Quasars in the Infrared

Habilitationsschrift

zur
Erlangung der Venia legendi
für das Fach Astronomie

der
Ruprecht – Karls – Universität
Heidelberg

vorgelegt von

Martin Haas

aus Mannheim

2001

Für Regina

Abstract

This thesis presents a combined view of results obtained for quasars and related objects with ISOPHOT, the photometer onboard the Infrared Space Observatory ISO. The infrared data are supplemented by sub-millimetre and millimetre photometry with the 30 m IRAM telescope, the 10 m Swedish ESO Submm Telescope and the 14 m James Clerk Maxwell Telescope. Three data sets of unprecedented sensitivity are investigated:

1) 17 optically bright and mostly radio-quiet quasars, randomly selected from the Palomar-Green catalogue: The former detection rate of about 30% by IRAS is now increased to about 70% (12/17). The spectral energy distributions (SEDs) provide evidence for luminous to hyper-luminous dust emission and do not support the existence of dust-poor quasars. The variety of SED shapes suggests the influence of different heating mechanisms like active galactic nuclei (AGN), powering the mid-infrared, and starbursts, mainly responsible for the far-infrared. The mid- and far-infrared luminosities are correlated, providing evidence for a close AGN–starburst connection. Because of the low extinction towards the centres, the dust might be organised in a disk or torus geometry seen face-on or at intermediate inclination. If such a system is seen edge-on, the extinction will be so high, that it will never be identified as a quasar via common criteria.

2) 10 pairs of luminous radio galaxies and radio-loud quasars from the revised third Cambridge catalogue, which match in both redshift and FR 2 lobe power: The former detection rate of less than 25% by IRAS is now increased to more than 60% (13/20). In 12 sources the quality of the SEDs clearly allows the thermal dust bump rising above the smooth synchrotron spectrum to be discerned, while the upper limits in the other sources are still compatible with a luminous dust component. The quasars and galaxies in our sample cannot be distinguished by their dust properties, providing the first successful evidence in the infrared in favour of the unification of radio galaxies as edge-on quasars.

3) 15 nearby bright ultraluminous infrared galaxies and 20 normal comparison galaxies: In order to search for radio-quiet hidden quasars, a new method is presented to probe high mid-infrared extinction. It uses the ratio between the PAH 7.7μm feature, which is sensitive to extinction, and the 850μm dust emission, which is optically thin and serves as normalizer. It is shown that the intrinsic PAH 7.7μm/850μm flux ratio lies in a well confined range with low dispersion. Exceptions are the two ultraluminous infrared galaxies UGC5101 and Arp220, with a very low ratio caused by high extinction. For Arp220 the central mid-infrared continuum is dereddened under the assumption that the dust follows a tilted disk-like distribution similar to that seen for the molecular gas traced by CO. After dereddening, both the mid-infrared luminosity and the luminosity density exceed a value typical for starbursts, increasing the evidence for a hidden quasar in Arp220.

The results from these samples represent new cornerstones which trigger further investigations from the entire ISO archive and from the upcoming satellites.

Contents

1 General Introduction **1**

1.1 Quasars and radio galaxies – an overview 1

1.2 The infrared view 4

1.3 The projects with ISO – the basis for this thesis 5

2 Optically bright quasars from the Palomar–Green catalogue **7**

2.1 Introduction 7

2.2 The data 8

2.3 Spectral energy distributions (SEDs) 8

2.4 PG quasars are dusty 12

2.5 Dust heating: AGN versus starbursts 13

2.5.1 Existing models 14

2.5.2 The variety of the SED shapes:
evidence favouring both AGN and starbursts 15

2.5.3 The luminosity correlations:
evidence for a close AGN – starburst connection 17

2.5.4 The remaining puzzle 21

2.6 Consequences for edge-on quasars 22

3 Radio galaxies and quasars from the 3CR catalogue **25**

3.1 Introduction 25

3.1.1 Unified schemes – the principles for unification 26

3.1.2 About to prove or disprove the unification 27

3.1.3 Status in the optical: pro unification 29

3.1.4 Status in the infrared: contra unification? 30

3.2 The data 31

3.3 Spectral energy distributions (SEDs) 31

3.4 Evidence favouring unification 33

3.4.1 Balanced detection statistics 33

3.4.2 Balanced dust luminosities 35

3.4.3 Synchrotron contribution in the infrared:
higher in quasars than in galaxies . . . 35
3.4.4 Consistency with other ISOPHOT observations . . . 35
3.5 The dust-to-lobe luminosity ratio . . . 36
3.5.1 Balanced distributions: further evidence for unification . . . 36
3.5.2 Environment and evolution:
New prospects for exploring their influence . . . 37
3.5.3 On selection effects . . . 37
3.5.4 Deviations from balanced distributions: the remaining puzzle . . . 40
3.6 The revised picture in the infrared:
substantial role of unification . . . 41

4 Search for hidden quasars among Ultra-Luminous InfraRed Galaxies 43
4.1 Introduction . . . 43
4.2 A new method to probe high mid-infrared extinction . . . 44
4.2.1 The data . . . 45
4.2.2 PAH 7.7μm/850μm extinction measurements . . . 46
4.3 Signatures for a hidden quasar in Arp220 . . . 48
4.3.1 The amount of the PAH 7.7μm extinction . . . 49
4.3.2 The extinction of the MIR continuum . . . 52
4.3.3 Dereddening of the MIR continuum . . . 56
4.3.4 The luminosity density: favouring a quasar . . . 58

5 Conclusions 61

6 Appendix: Advanced ISOPHOT Data Analysis 65
6.1 Optimised source detection . . . 66
6.1.1 Fourier analysis of chopped data . . . 66
6.1.2 Time series analysis of raster maps . . . 67
6.2 Influences on the detection statistics . . . 69
6.2.1 Galactic cirrus . . . 69
6.2.2 Mixture of observing modes with different sensitivities . . . 70
6.2.3 Cosmic particle glitch rates . . . 70

References 73

Acknowledgements 85

Chapter 1

General Introduction

1.1 Quasars and radio galaxies – an overview

Quasars were discovered about half a century ago: At the beginning, the new radio telescopes detected various enigmatic sources on the sky. Follow-up optical identifications and spectroscopy revealed the completely new class of radio galaxies, with Cyg A (= 3C 405) as the most prominent example (Baade & Minkowski 1954). Among these extragalactic radio sources some have a bright quasi-stellar like optical appearance and relatively high redshift. Thus they are extremely powerful, surpassing even the most luminous galaxies known. Famous examples of these so-called quasars are 3C 273 (Schmidt 1963) and 3C 48 (Greenstein & Matthews 1963).

Today at least a dozen classes of different quasars and radio galaxies are known. Prominent catalogs are the *revised third Cambridge catalog of radio galaxies and quasars* (3CR catalog, Laing, Riley & Longair 1983) and the *Palomar-Green catalog of optically selected quasars* (PG catalog, Schmidt & Green 1983). Quasars generally show special *optical* characteristics: compact extent, high luminosity and broad emission lines arising in the turbulent central region. Despite their initial discovery at radio wavelengths, most of the quasars discovered so far are not prominent radio emitters, hence "radio-quiet". Rather, the power of quasars is dominated by the optical, ultraviolet (UV) and X-ray regimes, where it originates from accretion processes onto a black hole in the centre of the so-called host galaxy (and not from nuclear fusion as in stars). Thus in the contemporary picture, quasars are the extremely luminous *active galactic nuclei* (AGN), which outshine their host galaxies.

The radio emission of a quasar comes from the one- or two-sided collimated jet-like outflows with relativistic speeds and from the very extended lobes, which comprise the working surface against the ambient circumgalactic medium. Fig. 1.1 shows a radio map of Cyg A. The radio emission is due to synchrotron radiation, i.e. fast electrons spiralling in magnetic fields. Variability is also observed, particularly in those sources with a flat

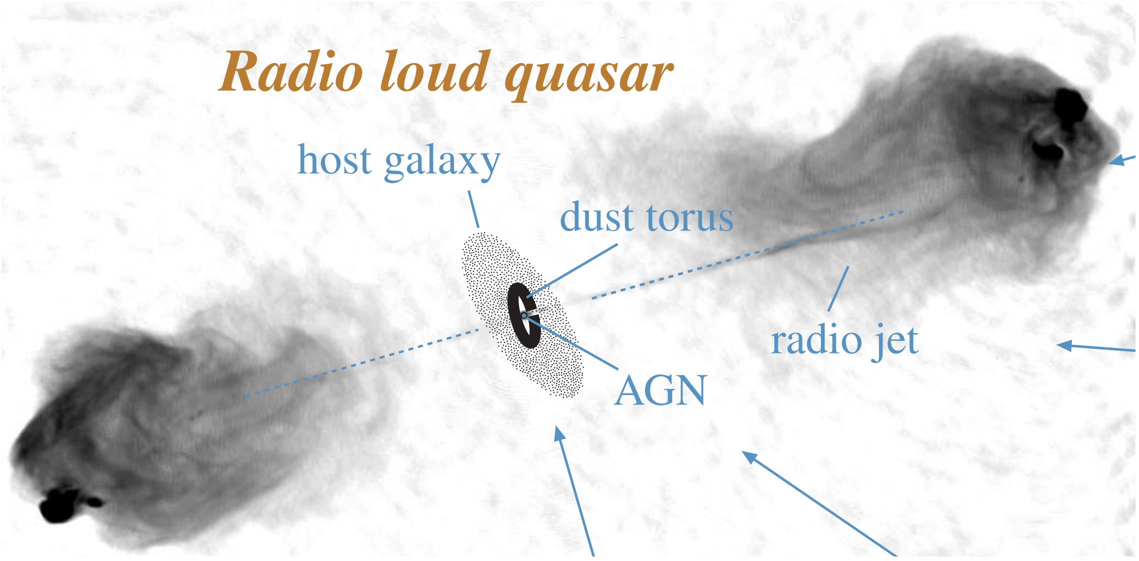

Figure 1.1: Schematic example of the components of a radio-loud quasar, superimposed on a radio map of the radio galaxy Cyg A with its jets and lobes (at 6 cm from Perley et al. 1984). The presence of the AGN is inferred in most cases from broad lines in optical spectra. The host galaxy can be seen in some cases on optical images. The presence of the dust torus is mainly inferred from indirect signatures. The extents of the components are about a few pc for the dust torus, about 10 kpc for the host galaxy and about several 100 kpc for the lobes (i.e. like the distance of the Andromeda Galaxy from the Milky Way). The arrows indicate the pole-on (along the jet axis), intermediate and edge-on aspect-angles. We see Cyg A roughly edge-on.

radio spectrum. At high frequencies it is accompanied by inverse Compton processes, as inferred from hard X-ray and γ-ray observations. The radio phenomenena seem to be a short flare-like phase in the lifetime of a quasar. During this phase, the black hole is effectively fed and also the magnetic field is well ordered, allowing for the formation of the jets (with a spectrum peaking predominantly at GHz frequencies) and the lobes (with a spectrum peaking predominantly at MHz frequencies).

Radio galaxies which do not yet show the optical signatures of a quasar do, of course, also house an AGN, since otherwise the formation of the jet and the powerful radio lobes cannot be explained. The AGN of radio galaxies, however, may be less powerful than that of radio-loud quasars – a case pointing towards environmental differences or just to an evolutionary connection between radio galaxies and quasars. Alternatively, the AGN may just be hidden from our view, for example by a dust torus seen edge-on – a case for a geometric unification of radio galaxies and quasars. To explore the relation between radio galaxies and quasars is still one of the great challenges. News on this topic is presented in

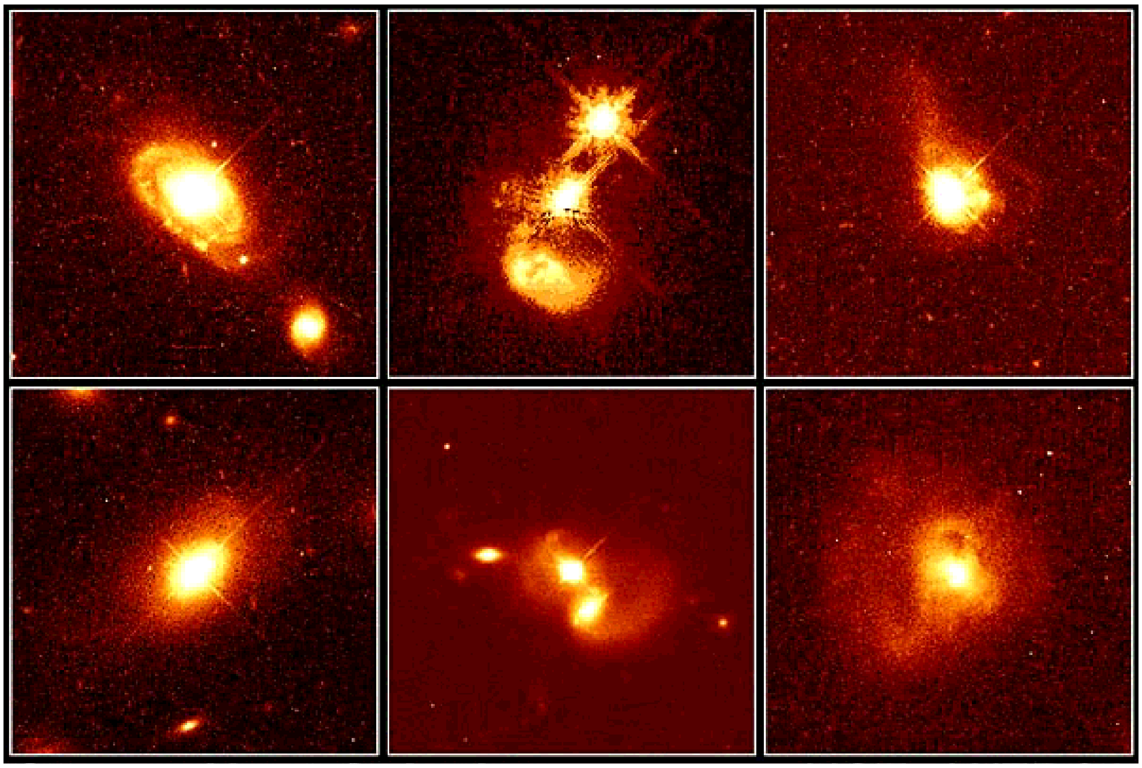

Figure 1.2: Optical images of quasars obtained with the Hubble Space Telescope (credit J. Bahcall & M. Disney, NASA). *Top left:* PG 0052+251, host galaxy with spiral arms. *Bottom left:* PHL 909, with elliptical host galaxy. *Top center:* Galaxy collision, the debris of which may fuel the quasar. *Bottom center:* PG 1012+008, interaction between the quasar and the passing bright galaxy (the object just below the quasar). *Top right:* Quasar 0316-346 with tidal tails, suggesting interaction with a passing galaxy which is located outside the image. *Bottom right:* Two merging galaxies IRAS 13218+0552, orbiting each other several times before final merging.

chapter 3.

The formation of quasars is far from being understood. The advent of sensitive high resolution (sub-arcsec) optical imaging has allowed for an investigation of the morphology of the host galaxies. Some of them show disturbances and signatures of galaxy interactions (Fig. 1.2). They point towards galaxy collisions and mergers as triggers for quasar formation (Hutchings et al. 1981, 1982a,b, 1983, Stockton 1982, Bothun et al. 1982, Gehren et al. 1984, Stockton 1986, Bahcall et al. 1996, 1997, Disney 1998)

A wealth of conference proceedings during recent decades reflects the enormous research activities on quasars which are still ongoing. A good overview can be obtained by the reviews by Bregman (1990) and Urry & Padovani (1995), and the books "Colliding Galaxies" by Barry Parker (1990) and "Active Galactic Nuclei" by Ian Robson (1996).

1.2 The infrared view

As "infrared" (IR) conveniently the wavelength range between 1 μm and 1 mm is called, which fills the gap between the optical and the radio regimes. This range is subdivided into the near-, mid-, far- infrared (NIR, MIR, FIR) and sub-millimetre (sub-mm) ranges, with borders at around 5 μm, 40 μm, 250 μm, which sometimes vary depending on the context.

With the advent of infrared detectors in astronomy in about 1970, a hand-full of AGN were immediately studied (Telesco et al. 1976, Hildebrand et al. 1977). Instead of radio-quiet quasars, for sensitivity reasons only some bright nearby Seyfert galaxies, which may be considered as low luminosity quasars, have been observed. While the mid- and far-infrared emission of the (variable) quasar 3C 273 represents the featureless continuation of the radio synchrotron spectrum towards shorter wavelengths, the Seyfert 2 galaxy NGC 1068 exhibits a thermal spectrum with a pronounced peak in the far-infrared and a low flux level at mm and longer radio wavelengths, similar to what is observed in starburst galaxies (i.e. galaxies with intense bursts of star formation).

Because the earth's atmosphere absorbs most of the infrared radiation coming from astronomical targets, sensitive infrared telescopes have been mounted on planes or spacecrafts. In 1983, the IRAS satellite provided the first statistically useful 10–100 μm infrared database for quasars and radio galaxies (Neugebauer et al. 1986, Golombek et al. 1988, Sanders et al. 1989, Heckman et al. 1992, 1994, Hes et al. 1995). But most quasars and radio galaxies were too faint to be measured properly at more than two of the four filters. Therefore the nature of the infrared emission remained controversial: It could be reprocessed emission from dust grains in a circumnuclear torus or the host galaxy – as indicated by low mm fluxes (e.g. Chini et al. 1989a) – as well as synchrotron radiation – as indicated by the variability in some sources (e.g. Neugebauer et al. 1986). As is typical for many astronomical debates, most likely the real case is a mixture of both contributions. To disentangle the contributions constitutes the main challenge for subsequent infrared observations of quasars and radio galaxies. Chapters 2 and 3 treat this topic.

Of special interest is whether there are quasars hidden by dust. These could be either young quasars – perhaps still located in a dusty merging environment as proposed by Sanders et al. (1988a) – or even evolved ones seen under special geometric circumstances like a dusty torus viewed edge-on. The IRAS satellite discovered the so-called ultra-luminous IR galaxies (ULIRGs), dusty galaxies which emit the bulk of their energy in the mid- and far-infrared and reach quasar-like luminosities ($L_{IR} > 10^{12}\ L_{\odot}$). Since the dust extinction in the ULIRGs often prevents any practical optical view of the central regions, infrared observations (penetrating even quite a large dust column) are best suited to shed further light on their geometric and/or evolutionary relation to quasars. News on this topic is presented in chapter 4.

Compared with optical and radio capabilities, the sensitivity and spatial resolution of infrared observations is still limited. Nevertheless, the infrared regime fills an important gap between optical and radio wavelengths and has now become an established field of quasar research, with growing future perspectives.

1.3 The projects with ISO – the basis for this thesis

The *Infrared Space Observatory ISO* (Kessler et al. 1996) successfully operated in orbit from November 1995 until April 1998, with the mid-to-far-infrared photometer ISOPHOT (Lemke et al. 1996) as one of its four instruments onboard. With 3-200 μm ISOPHOT covered a larger wavelength range and offered the possibility to reach higher sensitivity than was possible with IRAS, thus it provided ideal prerequisites for shedding new light on the nature of quasars and radio galaxies. ISOPHOT also allowed for 6-12 μm low resolution spectroscopy suited to studying the so-called PAH features of bright sources like nearby ULIRGs.

A number of open and guaranteed time observations were performed. Their evaluation is still ongoing and will probably take the next 5-10 years of the ISO archive phase. A couple of fundamental results have already been obtained.

In order to coordinate the guaranteed time observations the *ISO European Central Quasar Programme* led by R. Chini (MPIfR Bonn, now at Univ. Bochum) and K. Meisenheimer (MPIA, Heidelberg) and the *US ISO Quasar Key Project* led by B. Wilkes (Harvard CfA, Cambridge) were set up. The *ISO European Central Quasar Programme* contains several samples of quasars and radio galaxies, carefully selected for an optimized study of dedicated topics.

In parallel, guaranteed time observations of the nearby bright ULIRGs were coordinated by a photometry consortium led by U. Klaas (MPIA, Heidelberg) and a spectroscopy consortium led by R. Genzel (MPE, Garching).

The infrared data taken by ISO are supplemented at longer wavelengths by follow-up sub-mm and mm photometry for the quasars with the 30 m IRAM telescope on Pico Veleta, and for the ULIRGs with the 10 m Swedish ESO Submm Telescope SEST on La Silla and the 14 m James Clerk Maxwell Telescope JCMT on Mauna Kea.

This thesis presents a combined view of selected results obtained for the samples in the *ISO European Central Quasar Programme* and the ULIRGs. They are organized into three chapters, at the beginning of which more comprehensive introductions are given, a common conclusion and an Appendix on data reduction:

- Chapter 2 starts for practical reasons with the optically selected radio-quiet quasars, where the synchrotron contribution is lowest and the dust properties can best be recognised (Haas et al. 1998a, Chini & Haas et al. 1999, Haas et al. 2000).

- Chapter 3 reports on radio-loud quasars and their unification with radio galaxies, which represents the first successful evidence in the infrared (Haas et al. 1998a, 1999, Meisenheimer & Haas et al. 2001).

- Chapter 4 presents a new method to reveal hidden quasars among ULIRGs based on the sub-mm and mm follow-up observations and the spectroscopic ISOPHOT-S data (Haas et al. 2001).

- Chapter 5 comes to a common conclusion, with particular emphasis on what remains to be done next with the subsequent infrared telescopes.

- Chapter 6 (Appendix) contains some details on the sophisticated data reduction, which essentially helped to work out the astronomical results.

The main focus of this thesis is on the general detection of dust in quasars, the clues about the dust heating mechanisms, and – as a consequence of the high dust incidence – the geometrical aspects for the appearance of hidden quasars; the evolutionary relations are not considered further here, since the samples are too small. This topic will be treated in Ulrich Klaas' Habilitationsschrift (in preparation) in connection with the unique infrared-to-mm SEDs of a large sample of 41 ultraluminous infrared galaxies (Klaas & Haas et al. 2001).

Chapter 2

Optically bright quasars from the Palomar–Green catalogue

2.1 Introduction

The Palomar–Green catalogue (Schmidt & Green 1983) provides an optically selected sample of 114 bright quasars. Despite the first statistically useful mid– and far–infrared data by IRAS (Neugebauer et al. 1986, Sanders et al. 1989), the observational basis in the IR is still limited. Only 36 sources have been found by Barvainis (1990) and only 24 sources using stricter selection criteria by Rowan–Robinson (1995), which are detected in both the 25 μm and 60 μm bands representative for the MIR and FIR emission. In this chapter we focus on the following topics:

1) The primary challenge is to improve on the detection rate and to corroborate the thermal nature of the IR emission.

2) The current understanding of the ultraviolet to FIR continua of PG quasars is guided by a three component model (Barvainis 1990, Rowan-Robinson 1995) consisting of

   - a UV-optical component due to the black hole accretion disk,
   - a central 'AGN' dust component spatially associated with the narrow line region, showing up in the NIR-MIR at $3 - 25\,\mu$m with the UV–optical photons as primary heating source,
   - a 'starburst' dust component represented by the FIR $60 - 100\,\mu$m emission, probably radiating from extended regions in the host galaxy.

   The relation between AGN and starburst components is a main issue of the current debate: On the one hand a wide variety of shapes in the IR continua has been reported favouring independent components (Barvainis 1990); on the other hand a correlation between the luminosity of these two components has been found

(Rowan–Robinson 1995). Since only those sources detected at both 25 and 60 μm are considered, such a correlation could be forced by ignoring those possibly existing sources for which exactly one of either the mid- or far-infrared fluxes is low and falls below the detection threshold.

3) The suggested existence of edge-on quasars in analogy to the Seyfert 2 galaxies is also under discussion, and predictions about their observational appearance from properties of non-edge-on quasars (like those assumed in the PG sample) are desired.

These topics require high sensitivity observations as were anticipated for ISO.

2.2 The data

Broad band photometry has been obtained with ISOPHOT between 5 and 200 μm of a sample of 17 PG quasars out of the *ISO European Central Quasar Programme*.[1] These data are complemented for 11 sources by 1.3 mm observations with the 30 m IRAM telescope. Though not statistically complete, the data set represents a fair random sample (out of all PGs) with a well balanced coverage of redshift range from nearby ($z \approx 0$) to distant ($z = 2$) objects. A preliminary look in the ISO Data Archive indicates that the future inclusion of additional PG quasars covered by the *US ISO Quasar Key Project* (about 25 sources, Wilkes et al. 1999) might corroborate the results drawn from our small sample.

2.3 Spectral energy distributions (SEDs)

The IR and mm fluxes are listed in Table 2.1. The four brightest sources detected by IRAS were also well detected by ISO, and the fluxes all agree within 15%. Two sources marginally detected by IRAS are now clearly confirmed by ISO. In addition, eight new detections in the IR could be achieved. For the remaining three out of 17 sources, upper limits are provided at all wavelengths.[2] 11 sources were measured at 1.3 mm; four sources were detected and good upper limits were provided for the remaining seven sources.

[1] Originally all PG quasars were selected which have B<16 mag and lie in the sky area visible by the ISO satellite. About one third of the PG sample was contained in the *ISO European Central Quasar Programme*, the rest was covered by the *US ISO Quasar Key Project* (Wilkes et al. 1999; Hooper et al. 1999). During the actual execution of the first measurements it turned out that the occurrence of high energy particle glitches and the presence of cirrus structure required a more time consuming measurement mode. Therefore the samples had to be reduced due to (1) time constraints, (2) sources with low cirrus foreground for optimum detectability and (3) further sky visibility constraints. From the originally selected sample, 17 sources were observed. Three of our sources are also contained in the sample of 24 PG quasars by Rowan-Robinson (1995).

[2] Fig. 6.4 in section 6.2.1 (Appendix) illustrates that the cirrus ("background brightness") mainly determines whether detections or upper limits can be achieved, and that the upper limits are not biased at high redshift.

Table 2.1: Measured fluxes in mJy.
Bold numbers are detections above the 3–sigma level, the errors are 10–30% of the quoted fluxes depending mainly on the source/sky brightness contrast as seen by the apertures used. The source/sky contrast (last column) is averaged for the wavelength range between 60 and 100 μm. The thin numbers represent 3–sigma upper limits. The * indicates those cases also detected with IRAS. 'co-add' was successfully applied to the 60 and 100 μm maps of PG 0044 resulting in a broad 80 μm band detection. Some sources were observed twice, with the second observation preformed in the more sensitive mapping mode (see Chapter 6).

PG name	4.8 μm	7.3 μm	11.5 μm	12.8 μm	20 μm	25 μm	60 μm	100 μm	150 μm	170 μm	200 μm	1300 μm	src/ sky
0003	<18	<27	<48	<186	<99	<111	<204	<231		<516			1
							<147	<99		<135			
0026	**17**	**15**		**22**	<138	<213	<228	<129		<315			1
							<162	<132		<144			
0043	<12	< 9	<21	<39	<123	<111	<300	<159		<126			1
							<222	<117		<90			
0044	**15**	**18**	**17**	<105	<96	<393	<303	<138					<1
coadd							**92**			**94**			
0050	**110**	**269**		**554***	**936**	*	**1752***	**2339***		**1529**		< 3.6	>10
0052	<63	**36**	**34**	<198	<114	<87	<141	**163**		<198			1
							<147*	**109**		**125**			
1206	<3			**23**	**64**		**257**	**353**		**189**		**1.8**	3.5
1241	**7**	<27		<87	<99		**378**	**217**		<96		**3.3**	2.5
1247	<9	**10**		**30**	<183		**236**	**174**		<150		< 2.1	2
1254	**22**	**27**		<90	<114		**307**	**242**		<345		< 1.8	1.5
1259	<15			<45	<108		<141	<87		<48		< 2.1	1.5
1302	**13**	**19**		**32**	<180		**343**	**343**		<189		**635**	2
												168	
												185	
1307	<84	**14**		<54	<144		**212**	**155**		<174		< 1.5	1.5
1411	<78	**59**		**102***	**182**	*	**147***	**140**		<129		< 1.8	2
1613			**74**	*		**194***	**591***	**1002***	**858**	**730**	**539**	**1.6**	>10
1634			**48**	*		**120***	**267***	**349***	**230**	**206**	**158**	< 1.5	3.5
2112	<54	**33**		**41***	**45**		<135*	<216		<231			1

The spectral energy distributions (as measured, not corrected for redshift) are shown in Fig. 2.1 supplemented by data from literature (a complete reference list is given in Haas et al. 2000). Note that the temperature values of the blackbodies shown in Fig. 2.1 are corrected for redshift. The most remarkable feature of the SEDs is the steady flux increase from the NIR over the MIR peaking in the FIR regime at about 60 μm (PG 1411+442 peaks already at 25 μm), followed by the beginning of the Rayleigh–Jeans tail which steeply falls off towards the 1.3 mm data points (except for the radio loud object PG 1302-102, which still shows a thermal bump above the synchrotron spectrum). This steep fall-off is most obvious for PG 1613+658 (and PG 1634+706) with a spectral index $\alpha_{200-1300\mu m} \approx 3.1$ (> 2.6). It again demonstrates that the radiation is not due to synchrotron emission but rather originates from thermal dust emission as was previously shown for some quasars by Chini et al. (1989a) and Hughes et al. (1993).

Even for the radio loud quasars PG 0044+030 and PG 1241+176 (with steep spectrum)

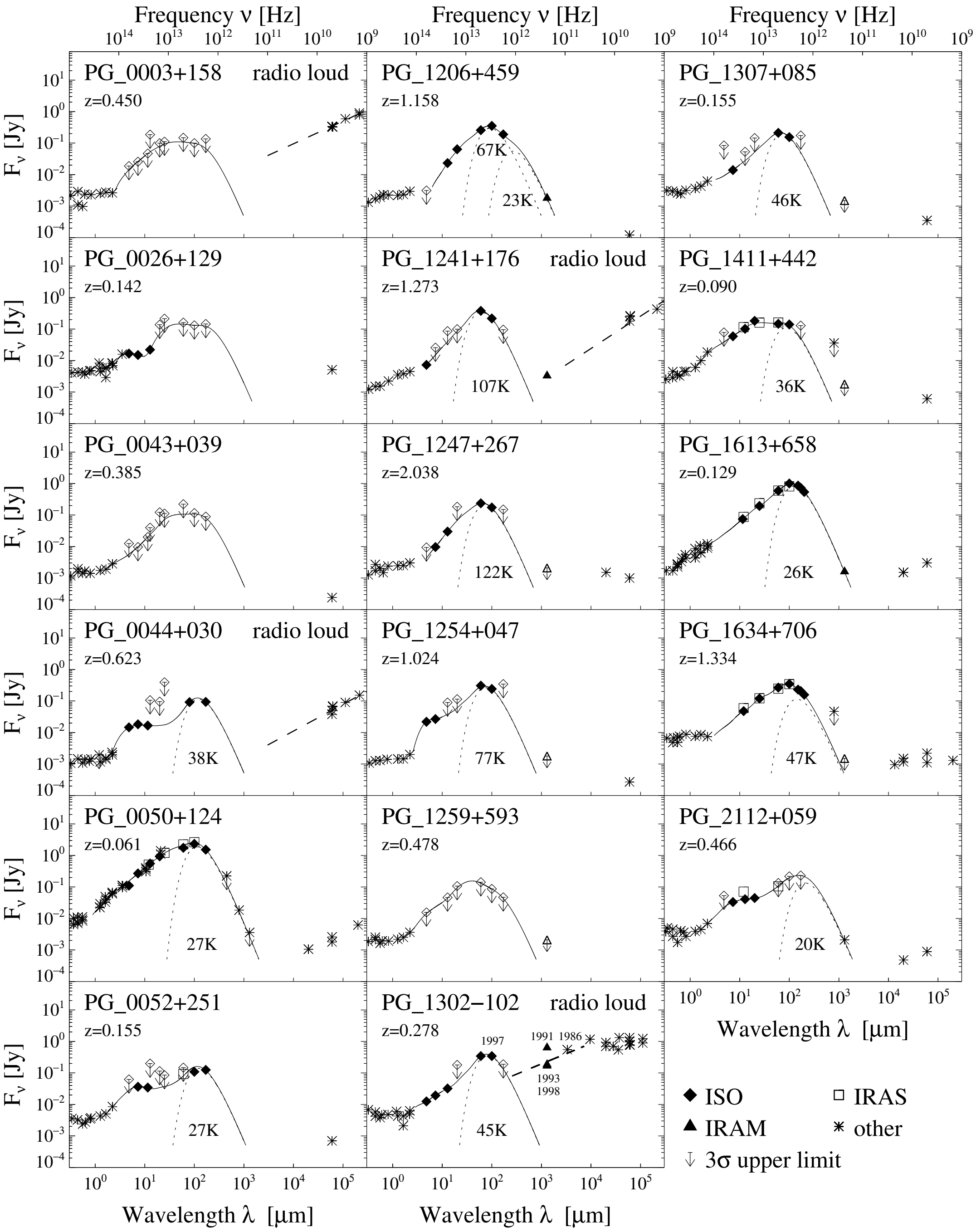

Figure 2.1: Spectral energy distributions of the PG quasars.

The wavelength and frequency ranges are as observed and not shifted to the rest frame of the objects. Several modified blackbodies with emissivity proportional to λ^{-2} are eyeball fitted to the data (solid lines) and only the coolest components are plotted individually (dotted lines). The photometric errors are less than 30%. Where only 3-σ upper limits are achieved (e.g. for PG 0003+158), the solid lines indicate the range from which the luminosity limits in Table 2.2 are derived. The temperatures listed are corrected for redshift. The long–dashed lines indicate extrapolated synchrotron spectra. For the variable radio source PG 1302–102 different epochs of the data groups are indicated by the year.

and PG 1302–102 (with flat spectrum) the thermal bump rises sharply above the synchrotron emission. PG 1302–102 was monitored at 1.3 mm over the last seven years, showing that the synchrotron activity was actually low at the time of the ISO observations in 1997. This means that the chance of detecting a thermal bump was quite high. The confidence in the $60 - 100\,\mu$m bump is strengthened by the upper limit at $170\,\mu$m. A similar case of a thermal bump above a relatively bright and flat (hence beamed) synchrotron spectrum was also found by ISO observations of the quasar 3C279 (Haas et al. 1998a).

The IR SED of each quasar can be modelled by a superposition of several modified blackbodies (dust emissivity proportional to λ^{-2}), indicating the presence of a wide variety of temperatures from hot (1000 K) to cool (30 K) dust in these objects. The temperature of the coolest dust component lies in the range between 30 and 120 K.

Interestingly, the SEDs of some sources (e.g. PG 0050+124 and PG 1613+658) fall off extremely steeply beyond their maximum flux at about $100\,\mu$m. It is not yet clear how the fall-off is for the other sources (Fig. 2.1), and whether a difference in the fall-off behaviour can be established. The steep spectral fall-off means that on the "cool side" there is no steady layering of several colder dust components which are still luminous and possibly distributed more on the outside and diffusely within the host galaxy. Any luminosity contribution from such a layering is negligible. This suggests that among the luminous ones a well defined coolest dust component exists, which probably also has a well defined spatial extent. The coolest dust component could also be the consequence of a high, but homogenous diffuse "interstellar" radiation field distributed throughout the host galaxy.

Although our high redshift sample is small (5 sources at $1 < z < 2$), it seems remarkable that for all our sources the SED peaks close to $60\,\mu$m. As a consequence, the temperature of the coldest luminous dust component appears hotter the higher the redshift is (from 30 - 40 K at $z = 0$ to 90 - 120 K at $z = 2$). In one case (PG 1634+706) the IRAM 1.3 mm limit provides the constraint that the peak does not shift significantly towards the sub–mm range with redshift. For the other sources like PG 1206+459 or PG 1254+047 the 1.3 mm fluxes or upper limits still allow for an additional, relatively faint, cool dust component. For the radio loud source PG 1241+176, the 1.3 mm emission probably originates from synchrotron radiation. Admittedly our sample is small, thus any dust temperature dependence on redshift is uncertain and the remarks are intended to point towards a possible trend. Further observations at sub–millimetre wavelengths should enable us to clarify whether the coolest dust component really has a higher temperature in quasars of an earlier epoch or larger luminosity, or whether the temperature trend appears just as an observational effect due to incomplete wavelength coverage of the current sparse data.

Table 2.2 lists derived parameters like luminosities, dust temperatures and masses, supplemented by additional quantities used in the following discussion. It should be stressed that the SEDs presented here resemble an excellent data set for PG quasars which enables interesting *qualitative* insights (e.g. on the SED shapes, section 2.5.2), and to some

Table 2.2: Luminosities, dust temperatures and masses.
The luminosity distance is determined as $D_L = c / H_0 * (z + z^2 / 2)$, i.e. $q_0 = 0$, with $H_0 = 75$ km/sec/Mpc. The soft X-ray 0.1-2.4 keV luminosity L_X is derived from the ROSAT archive. Note that in the restframe of the quasar the X-ray window shifts according to z. The absolute blue luminosity L_B in the restframe of the quasar is derived from Véron-Cetty & Véron (1998). The infrared luminosities L_{IR} (3-1000 μm), L_{MIR} (3-40 μm) and L_{FIR} (40-1000 μm) are computed from the blackbody curves shown in Fig. 2.1. T_{dust} refers to the coldest dust component derived from the decomposition of the SED. The dust mass M_{dust} is estimated according to Hildebrand (1983). The SED shapes are binned into power law increase (1), MIR dominated (2), FIR dominated (3); for details see section 2.5.2.

PG	**z**	**D_L** Mpc	**L_X** $10^9 L_\odot$	**L_B** $10^9 L_\odot$	**L_{IR}** $10^9 L_\odot$	**L_{MIR}** $10^9 L_\odot$	**L_{FIR}** $10^9 L_\odot$	**T_d** K	**M_{dust}** $10^5 M_\odot$	**L_{IR}/ L_B**	**L_{FIR}/ L_{MIR}**	SED type
0003	0.450	2203	812	765	< 4319	< 3790	< 529	29	< 982	<5.6	0.139	–
0026	0.142	608	108	160	< 329	249	< 80	17	<1992	<2.1	0.323	3
0043	0.385	1835	< 364	1009	< 1852	< 1426	< 426	27	< 1141	<1.8	0.299	–
0044	0.623	3266	282	1753	4247	3177	1070	38	1077	2.4	0.337	3
0050	0.061	251	35	92	803	575	228	27	983	8.7	0.396	1
0052	0.155	668	149	253	365	289	76	27	465	1.4	0.264	3
1206	1.158	7309	<3703	14582	45665	35996	9669	23	23901	3.1	0.269	2
1241	1.273	8327	<4563	14582	76877	71582	5295	107	88	5.3	0.074	2
1247	2.038	6448	5978	58052	197437	191048	6389	122	75	3.4	0.033	2
1254	1.024	6189	<2831	6979	36271	31579	4692	77	213	5.2	0.149	3
1259	0.478	2367	< 567	1599	< 5232	< 4681	< 551	33	< 367	<3.3	0.118	–
1302	0.278	1266	318	1106	1743	1094	649	45	281	1.6	0.593	1
1307	0.155	668	169	278	347	238	109	46	38	1.2	0.460	1
1411	0.090	376	3	121	269	239	30	36	27	2.2	0.125	2
1613	0.129	549	164	101	803	455	348	26	2113	8.0	0.765	1
1634	1.334	8889	1411	52944	88396	75895	12501	47	2004	1.7	0.165	1
2112	0.466	2297	15	1213	< 4539	3363	< 1176	20	< 18157	<3.7	0.350	2

degree also a *quantitative* investigation was possible (e.g. on the luminosity correlations, section 2.5.3). Some further attempts of a quantitative evaluation have been successfully tried (like the possible redshift or luminosity dependence of the temperature of the coolest dust component mentioned above or the estimate of the opacity from the mass of the cold dust component, section 2.6). Nevertheless, bearing in mind the measurement errors and the smallness of the sample, other more detailed quantitative studies among the 17 PG quasar SEDs (e.g. of the mass of the warm AGN-heated dust or the L/M_{dust} ratio as measure for the evolutionary status) are severely limited, hence do not make much sense. Such *quantitative* studies have to be left to future projects with larger and possibly more accurate data bases. Also the search for evolutionary trends among our small sample is not considered further here.

2.4 PG quasars are dusty

The spectra shown in Fig. 2.1 provide an impressive confirmation of the fact that the SED of an optically selected quasar contains a strong mid- and far-infrared bump due to thermal emission by dust. The thermal infrared luminosities span from luminous $10^{11}\,L_\odot$ to ultraluminous 10^{12}-$10^{13}\,L_\odot$, to hyperluminous $10^{14}\,L_\odot$ objects (Table 2.2). For four out of five quasars for which we could establish only upper limits the resulting FIR dust emission exceeds $10^{11}\,L_\odot$.

The random sample achieves a remarkably high mid- and far-infrared detection rate of 12/17 and 14/17, respectively. This rate of about 70% drastically increases the former detection rate of about 30% achieved by IRAS. Thus we infer a low probability p that dust–free naked quasars exist ($p \leq 3/17$). The amount of dust lies in the order of $10^{7\pm1}\,M_\odot$ (Table 2.2) which is typical for dust rich spirals (cf. Haas et al. 1998b) as well as luminous and ultraluminous infrared galaxies (cf. Klaas & Haas et al. 1997, 2001).

The 114 PG quasars are selected from the Palomar-Green survey of *stellar-like* objects with UV excess, thus the PG quasar sample may be biased against extended bright host galaxies. If the FIR emission comes primarily from dust in the extended host, then the PG quasars are also biased against dust emission, and for extended quasars even more dust emission may be expected. For example, the Hamburg quasar survey (e.g. Wisotzki et al. 2000) is based on objective prism plates (without restriction to stellar-like objects) and contains also "extended" quasars. Further sensitive IR observations will clarify whether these extended quasars are more dusty than PG quasars.

2.5 Dust heating: AGN versus starbursts

Since the dust must have been produced by stars, this supports the hypothesis that the quasars are accompanied or proceeded by a starburst. Further arguments in favour of the presence of starbursts come from morphological observations (partly with the HST), where interactions with companions have been revealed; also for some of our sources like PG 0052+251 (Fig. 1.2), which is a spiral with a ring of HII regions (Dunlop et al. 1993, Bahcall et al. 1996, 1997), PG 1302-102 (Hutchings & Neff 1992, Disney et al. 1995), PG 1411+442 (Hutchings & McClure 1990), and PG 1613+658 (Disney 1998). Nevertheless, the luminosity contribution from these starbursts is an open question.

What actually powers the enormous dust emission reaching up to about $10^{14}\,L_\odot$? As will be shown below, the AGN alone could provide sufficient heating energy. Nevertheless, the problem is to find a scenario in which the central luminosity can efficiently be transported to reradiate from cooler outer regions. Since the currently investigated models of pure AGN heating scenarios fail in a considerable number of cases, starbursts have been suggested as a second heating mechanism responsible for the FIR output (Rowan-Robinson 1995, 2000). Since only a limited number of AGN models has been thoroughly investigated, this conclusion is not compelling in the sense that a proper model for AGN heating might yet have escaped the theorist's imagination. Thus the AGN could still be the sole dominant heating source. Now we will first consider the existing models, and then see, how far our data can provide new insights.

2.5.1 Existing models

The broad range of dust temperatures challenges the models which try to describe the IR emission around AGNs. The PG quasars have blue colours and low E_{B-V} absorptions in the spectra of the broad line regions, but contain considerable amounts of dust (at least half of our sample has $M_{dust} \gtrsim 10^7\,M_\odot$). Therefore a non-spherical geometry like a disk or torus might be required, with a face-on or at least intermediate viewing angle, so that our line of sight to the blue centre is not affected by the dust torus.

A very thick and compact dust torus (Pier & Krolik 1992, 1993) cannot provide the broad temperature range required. Also for a thick and extended torus/flared disk with an r^{-1} density profile (Granato & Danese 1994, hereafter GD; Granato et al. 1997, herafter GDF), as well as a tapered disk (Efstathiou & Rowan-Robinson 1995), the predicted IR spectra are too narrow: they only fit the MIR range and fall far below the observed high FIR luminosity. In order to achieve broad MIR and FIR spectra, GD and GDF had to reduce the central dust density and to shift dust into the outer regions. In their model they assumed a disk with a dust density profile which is *constant* with radius. But such a profile has no physical basis and is found nowhere else, thus we reject this artificial type of profile. Instead, more interesting is a clumpy torus as proposed (for Seyfert galaxies) by Krolik & Begelman (1988) with the advantage that the dust, when organised in clouds, can more easily survive the extremely strong radiation field of the AGN. As mentioned by Efstathiou & Rowan-Robinson (1995) the clumpiness will tend to increase the dust temperature in the outer part of the torus, as the dust sees the inner and hotter part of the torus through the gaps between inner clumps. Detailed results for a clumpy torus model, however, are not yet available. Though very promising, it has to be clarified how far the required broad range of dust temperatures can be achieved with the AGN as the sole power source. In view of these (present) difficulties, enormous starbursts are required as the main heating power for the FIR emission.

Alternatively, a geometrically thin, warped disk in the host galaxy was proposed (Phinney 1989, Sanders et al. 1989), where due to the warp the concave "frontside" of the outer regions is directly illuminated by the central heating source. Though an elegant picture at first glance, a 3-dimensional radiative transfer calculation is still missing, and the warped disk as an explanation for the full MIR and FIR continua could not yet be confirmed by other observations and several objections have been mentioned:

(1) Pier & Krolik (1992) argued that with a warped disk viewed face-on (as would be the case for the quasars) one should see the 9.7 μm silicate feature in emission, because the surface of the warped disk will always be hotter than the main body, but the

expected silicate 9.7 μm feature has not been detected yet.

(2) Also, Rowan-Robinson (1995) argued that in at least some cases the FIR/UV-optical luminosity ratio is much too high to be explained with reprocessing by a dusty warped disk.

Note that Rowan-Robinson applied a conservative "violation criterion" requiring $L_{FIR} / L_{UV-opt} < \Omega$, with L_{UV-opt} being dereddened and $\Omega = 1$ being the violation threshold. Actually the violation threshold might be much lower: a warp with an inclination angle $\alpha°$ against the disk plane covers a fraction $\Omega = \alpha/180$ of the sphere, for example $\alpha = 18°$ results in $\Omega = 0.1$, and $\alpha = 36°$ results in $\Omega = 0.2$. The inclination angle might be at maximum 36°, otherwise the warp might become dynamically unstable and will be disrupted, leading rather to a distribution of clumpy clouds (which would no longer be described as warped disk model). Though a rough estimate, it shows that the violation threshold most likely lies at about $0.1 < \Omega < 0.2$, thus strengthening the objection against warped disks as an explanation for the FIR luminosity (e.g. PG 0050+124 and PG 1613+658 in section 2.5.4).

Warps may exist in the disks of quasar host galaxies, but they might not be suited to explain the near- to far-infrared spectra of quasars.

2.5.2 The variety of the SED shapes: evidence favouring both AGN and starbursts

We now investigate our quasar data. The SEDs show a variety of shapes. In order to provide clues for the discussion of the heating mechanisms, we searched for distinct features in the SED shapes. As a result, we choose to bin the SEDs into three groups (Fig. 2.2) with the following features:

1) a power law rise from the NIR to the FIR, most prominent for the low redshift quasars PG 0050+124 and PG 1613+658, similar for the high redshift quasar PG 1634+706 (but with a flat intrinsic optical component).

2) a strong dominance of the MIR: the most prominent case is PG 1411+442; probably PG 2112+059, with NIR/MIR detection, but only upper limit in the FIR, also belongs to this group. Furthermore, the high redshift sources like PG 1247+267 ($z>1$) very likely belong to this group: The observed FIR peaks intrinsically originate in the MIR and they could have an additional faint cool dust component (which should then be detectable in the sub-mm range). The SEDs of group 2 typically seem also to have a power law-like flux increase, but it lasts only from the NIR to the MIR ($\approx 30\,\mu$m) and is therefore not as striking as for that of group 1.

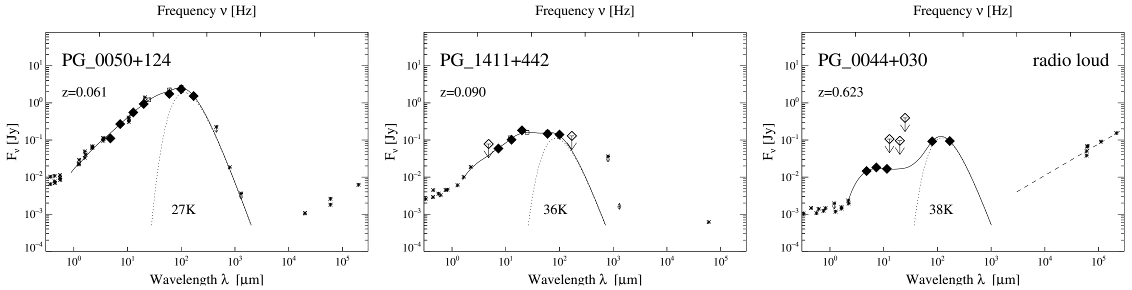

Figure 2.2: Examples illustrating the SED shapes: a power-law rise from the NIR to the FIR *(left)*, a strong dominance of the MIR *(middle)*, two maxima: one in the NIR/MIR and a dominant one in the FIR *(right)*.

3) two maxima: one in the NIR/MIR and a dominant one in the FIR, with a jump between 25 and 60 μm. PG 0044+030 and PG 0052+251 belong to this group.

Table 2.2 lists the classification of all 14 sources detected. Our current sample is obviously too small to decide whether the proposed groups are clearly distinct or only represent an arbitrary binning of a continuous distribution of SED shapes. Nevertheless, the grouping of the SED shapes according to the three features as presented above seems to be a fruitful way of disentangling the heating mechanisms. The power law rise of the SEDs of group 1 indicates a well ordered dependence between the dust components of different temperatures. It suggests, in fact, heating by a central source with a temperature gradient from inside to outside. In the cooler regions starbursts could perhaps become significant. The SEDs of group 2 (having also some power law flux increase, but a high MIR contribution with respect to that in the FIR) can be understood in terms of a central heating without need for an additional starburst outside. On the other hand, the SEDs of group 3 (having a low MIR plateau with respect to that in the FIR) are more reminiscent of interacting starburst galaxies and indicate either that a starburst is necessary, or that extinction plays a significant role, even in the MIR. However, there is no evidence for strong obscuration, since the L_{MIR}/L_B and L_{FIR}/L_B ratios are not exceptionally high, as shown below. (Alternatively, as mentioned in section 2.5.1 an irregular clumpy distribution of dust clouds at different distances from the AGN and heated solely by the AGN to different temperatures may also produce some variety in the SED shapes, but such a picture is not considered further here, since model results are not available.)

In conclusion, the variety of SED shapes – in particular the occurrence of MIR and FIR peaking SEDs – provides evidence for different heating mechanisms, favouring starbursts in addition to AGN. The relative contribution of the starbursts seems to vary from object to object, and in the next section we will consider how large the dispersion is.

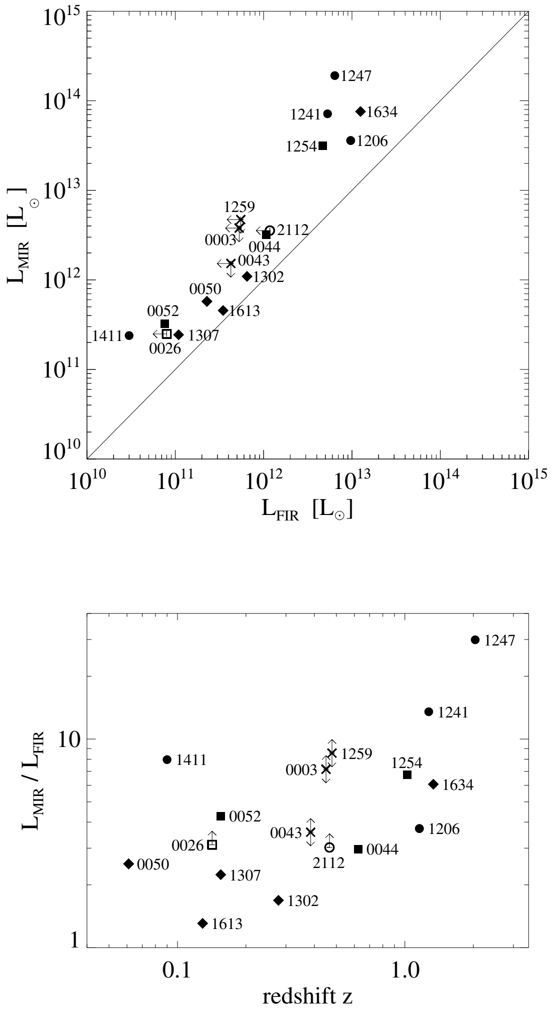

Figure 2.3: Restframe mid- versus far-infrared luminosity of the PG quasars. Different symbols for SED groups: (1) diamonds, (2) circles, (3) squares, (not classified) crosses. The solid line indicates equity. The bottom row shows the ratio against redshift.

2.5.3 The luminosity correlations: evidence for a close AGN – starburst connection

We now consider the restframe MIR and FIR luminosities. They are correlated over the whole luminosity range, as shown in Fig. 2.3 (top) using the values from Table 2.2. This extragalactic MIR luminosity – FIR luminosity correlation, however, could be dominated by the large distance range involved, i.e. it could correlate mainly the distance with itself. Therefore Fig. 2.3 (bottom) shows the MIR/FIR luminosity ratio against redshift. This plot clearly demonstrates that the correlation is basically real, but it is accompanied by a

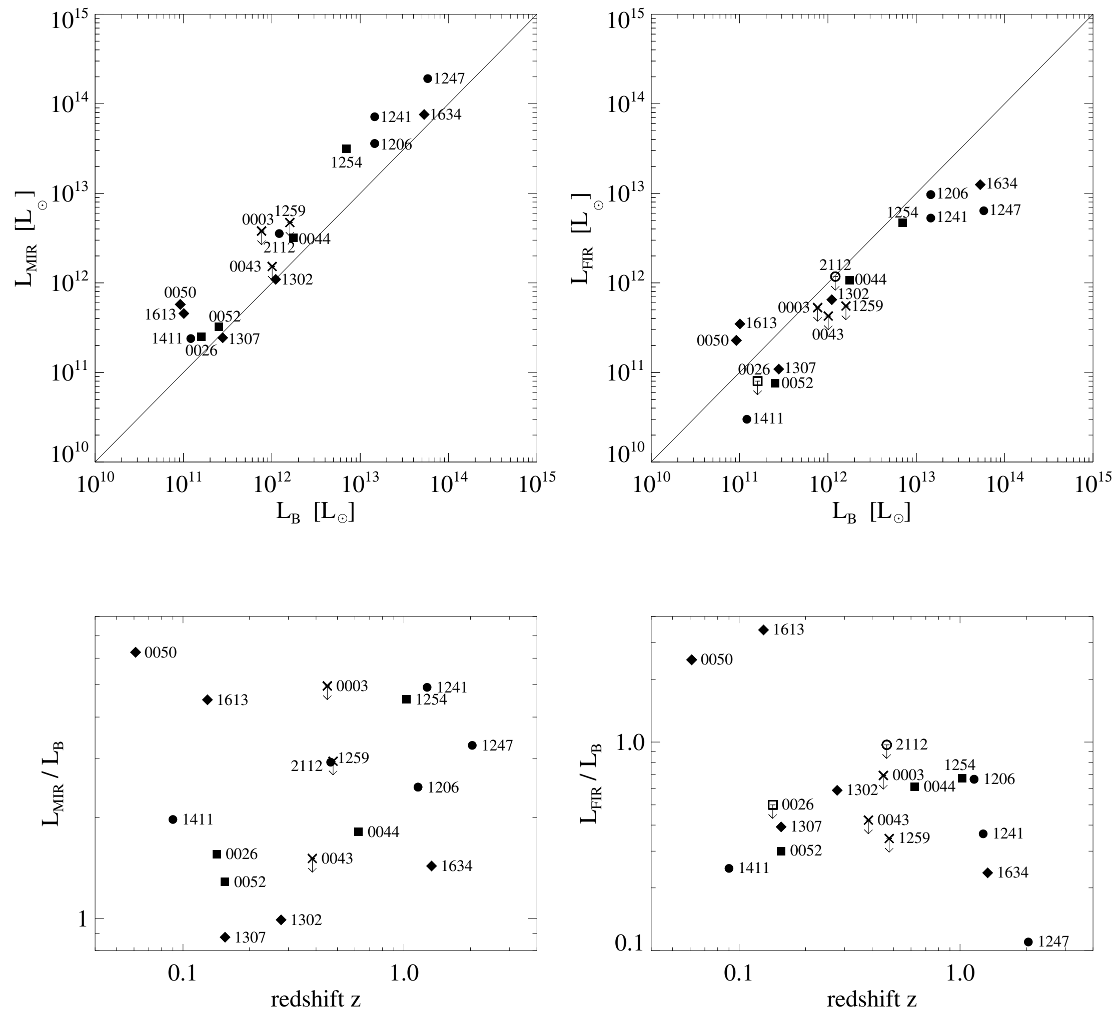

Figure 2.4: Restframe mid-infrared versus blue luminosity *(left)* and far-infrared versus blue luminosity *(right)* of the PG quasars. Symbols as in Fig. 2.3.

considerable dispersion of about one order of magnitude. It shows also a marginal *trend with SED shape*, in that the MIR peakers have the highest MIR/FIR luminosity ratio – as expected. But our sample is too small to allow for establishing a clear *separation* between the members of the SED groups. Irrespective of the SED shape the MIR luminosity is at least as high as that in the FIR.

Both the mid– and far–infrared luminosities are well correlated to the blue luminosity L_B (Fig. 2.4). There are no trends with SED shape. Remarkably both the L_{MIR}/L_B and L_{FIR}/L_B correlations are of similar quality. (The two L_{FIR}/L_B extremes PG 0050+124 and PG 1613+658 are discussed separately in section 2.5.4 below.) The blue luminosity must originate from the central region, since it is extremely well correlated with the broad

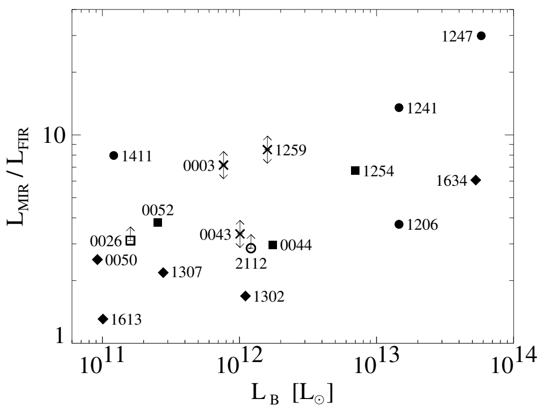

Figure 2.5: Restframe mid- to far-infrared luminosity ratio versus blue luminosity. Symbols as in Fig. 2.3.

line Lyman$_\alpha$ luminosity (cf. Netzer 1990). Furthermore, a starburst in the dense central region is expected to show more reddening than observed, hence L_B does not come from a starburst. Since $L_{UV-opt} \approx 9 * L_B$, we get $L_{UV-opt} > L_{IR}$ for all our quasars, hence the broad line region, in principle, can provide sufficient energy to account for the entire dust emission.

The correlations between the blue, the mid- and the far-infrared luminosity indicate a common heating source for the MIR and FIR dust components or a coupling between the different heating sources. In the case of two heating sources – AGN *and* starburst – the correlations can be interpreted qualitatively as proposed by Rowan-Robinson (1995): the more massive and powerful the starburst, the more likely it is for the matter to have an unstable angular momentum and to drop into the black hole. The AGN then strongly heats the central dust component. There are of course individual irregularities, reflected by the different SED shapes and the scatter shown in Fig. 2.3 bottom, which could be caused by different extinction, aspect angles or evolutionary states. If a turbulent gas supply (as indicated by the starbursts) appears to be a prerequisite for effectively feeding the AGN, one may ask (for future investigations), whether the collision and merger of two galaxies poor in gas and dust can effectively create a quasar.

A further trend may be recognised along redshift and/or blue luminosity: the more redshifted and/or luminous sources tend to have a higher MIR/FIR luminosity ratio (Figs. 2.3 (bottom) and 2.5). This colour trend is not an observational artefact due to missing or unknown sub-mm flux, since the maximum possible FIR luminosity can be well estimated by our IRAM 1.3 mm flux limits (see Fig. 2.1). In PG 1247+267 for example, an additional cool dust component hidden underneath the 1.3 mm flux limit would increase the FIR luminosity only by a maximum factor of two, hence the MIR/FIR trend with lumi-

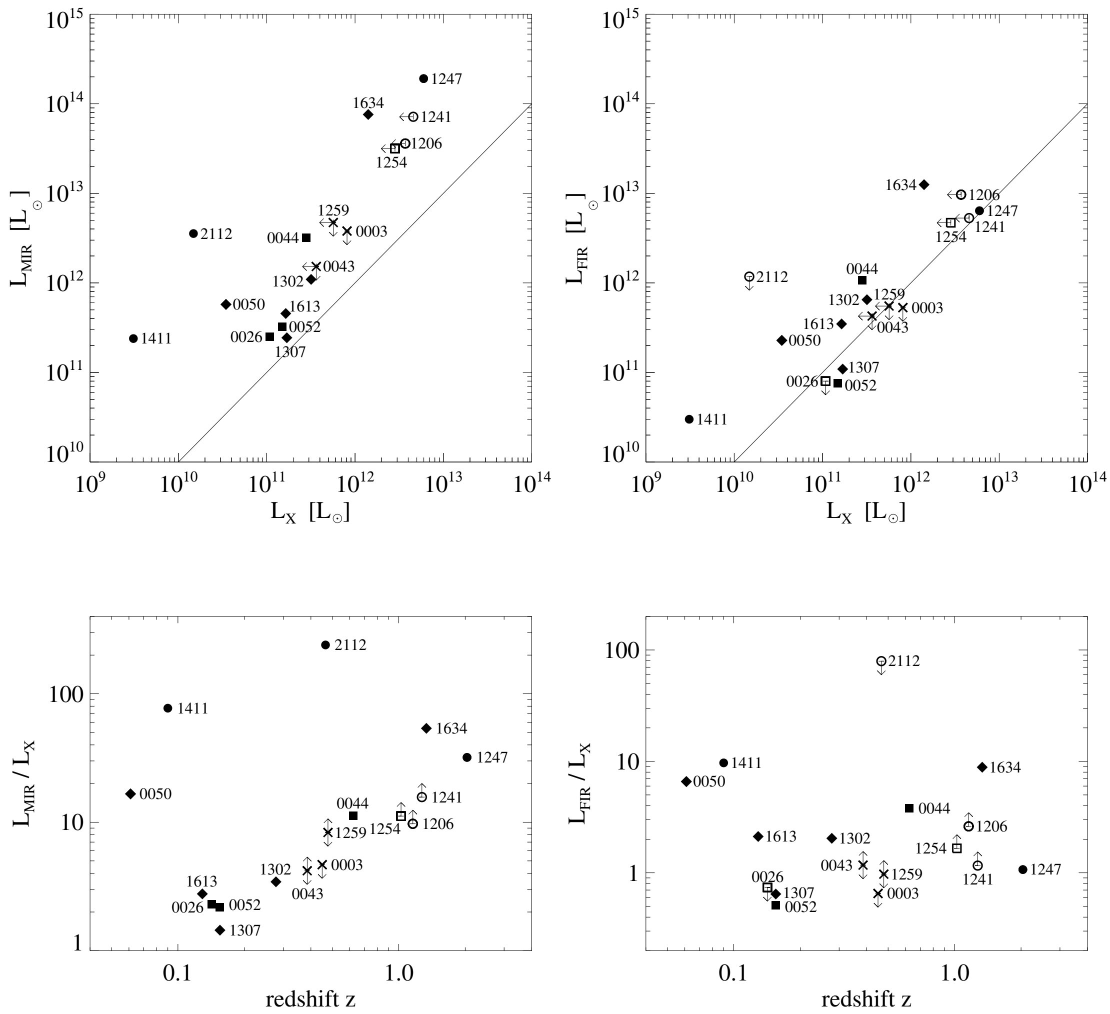

Figure 2.6: Restframe mid-infrared versus soft X-ray luminosity *(left)* and far-infrared versus soft X-ray luminosity *(right)* of the PG quasars. Symbols as in Fig. 2.3.

nosity still remains. (As for the temperature of the coolest dust component mentioned in section 2.4, further observations should allow us to clarify whether this trend is actually due to luminosity or redshift.)

If the FIR emission is mainly caused by starburst, then supernova remnants (SNRs) will play a significant role. Since SNRs are also powerful X-ray emitters, we looked for a correlation between the MIR and FIR luminosities and the soft X-ray luminosities we derived from the ROSAT archive. Such correlations are present, but weak (Fig. 2.6). The soft X-rays (0.1-2.4 keV) are believed to originate from the AGN (the accretion disk or the corona or a jet) as well as from SNRs. If they come primarily from SNRs, then the L_{FIR}/L_X correlation should be better than the L_{MIR}/L_X one (again assuming the MIR

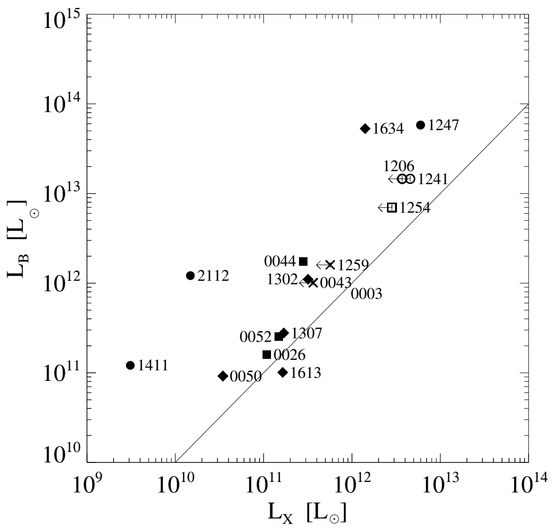

Figure 2.7: Restframe blue versus soft X-ray luminosity of the PG quasars. Symbols as in Fig. 2.3.

to arise mainly from the AGN and the FIR to be dominated by starbursts). But within the scatter of the distributions this is not observed (and in addition some sources show X-ray variability already favouring an AGN origin of the X-rays), thus the soft X-rays cannot be used to support the starburst hypothesis. Furthermore, the L_{FIR}/L_X ratios of our quasars lie between 0.5 and 10, and hence are considerably lower than typical values of about 10-100 found for SNRs in the Milky Way (G. Hasinger, private communication; see also Dwek et al. 1987). Therefore the soft X-rays might originate mainly from the AGN, i.e. its accretion disk or its corona. (We do not consider the jet possibility since most of our sources are radio quiet.) Note the trend that the MIR dominated SED group 2 shows the highest L_{MIR}/L_X and L_B/L_X ratios. Interestingly, the scatter in the L_X to L_B correlation (Fig. 2.7) indicates a variety in soft X-ray generation and absorption of the central region. One interpretation could be that if the black hole is fuelled at about the maximum rate (Eddington limit), then a lot of matter is centrally located which could also act as an X-ray absorber.

2.5.4 The remaining puzzle

So far we have arrived at a consistent picture in which the quasars with a strong MIR bump (SED group 2) can be well understood in terms of a pure AGN heated dust torus with no evidence for starbursts. And those quasars with a strong FIR bump (SED group 3) look as though they definitely require a starburst. Nevertheless the question remains as to why the (possibly more extended) starburst luminosity in these sources is of similar order to the (more central) AGN luminosity. Interestingly, other correlations between nucleus and extended regions have been found, too: (1) In the near infrared, the luminosity of the central unresolved point source increases with that of the host galaxy (McLeod & Rieke 1994a, 1994b), and (2) the mass of the black hole as derived from H_β lines shows a clear trend with the optical luminosity of the bulge of the host galaxy (Laor 1998).

Puzzling objects in the picture of two heating sources are those with the long lasting power law flux increase from the NIR to the FIR (SED group 1). The two sources PG 0050+124 and PG 1613+658 lie clearly above the main population in the L_{FIR}/L_B diagram, while in the L_{MIR}/L_B diagram (Fig. 2.4) they lie closer to the mean, indicating for these two sources either that in case of pure AGN heating a special scenario is required or that a strong starburst contributes significantly to the FIR luminosity. In the latter case the SED of group 1 could be understood as a suited combination of SED group 2 and 3. Then two relatively independent heating mechanisms have to produce a remarkably smooth flux increase from the NIR to the FIR. If one discards this possibility as unlikely, then the SED group 1 has to be fully explained with the AGN as the dominant power source and the proper geometry or scenario has to be searched for and thoroughly investigated. Then the most promising scenario seems to be the clumpy torus model. (The warped disk model might be discarded for PG 0050+124 and PG 1613+658 which have $L_{FIR} / L_{UV-opt} \approx 0.3 > \Omega \approx 0.2$,see section 2.5.1).

2.6 Consequences for edge-on quasars

As pointed out in section 2.5.1, the presence of dust in PG quasars and the low absorption in the spectra of the broad line region argue in favour of a disk or torus geometry which is seen face-on or at an intermediate viewing angle. Thus the question arises of how the edge-on counterparts of PG quasars will appear to us.

Firstly, we consider the extinction predicted for the edge-on case: From our data the dust mass and the *opacity* can be estimated as relatively free from any screen bias, since the FIR radiation might be optically thin. Distributing a dust mass of $10^8\,M_\odot$ (e.g. for PG 0050+124, Table 2.2) homogeneously within a slab of 100 pc height and 1000 pc radius yields a dust column density of about 30 $M_\odot\,pc^{-2}$ face–on and 300 $M_\odot\,pc^{-2}$ edge–on (Fig. 2.8). Adopting a common conversion of 0.1 $M_\odot\,pc^{-2}$ to $\tau_V \approx 0.5$ yields an opacity $\tau_V \approx 150$ for face–on and $\tau_V \approx 1500$ for edge–on view. Using $A_{25\mu m}$ / $A_V \approx 0.063$ (MRN extinction curve, Mathis et al. 1983) yields an edge–on optical depth of $\tau_{25\mu m} \approx 90 >> 1$.

Though only a rough estimate, it also reveals for larger slab heights and smaller radii as well as an r^{-1} dust density profile, that the edge–on viewed disk or torus is opaque to its own central MIR radiation. And this might also hold for a *clumpy* disk or torus. Since the extinction and reddening in the optical, UV and even the soft X-ray range is extremely high for an edge-on quasar, such a source will never be identified as a quasar via common

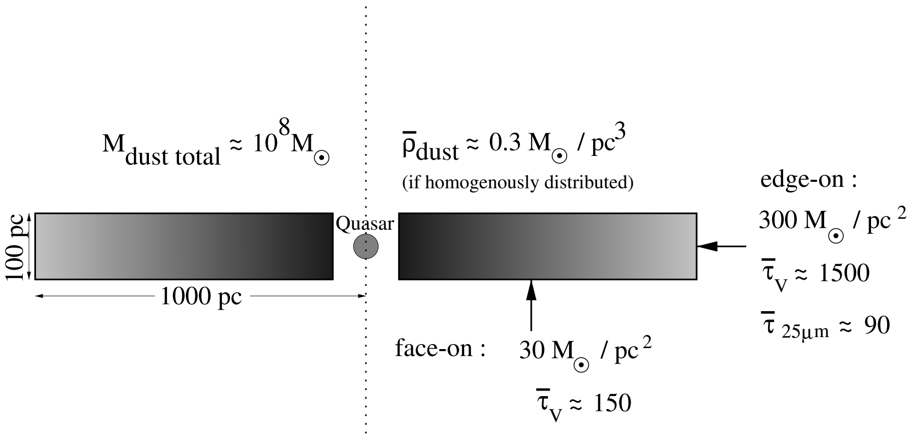

Figure 2.8: Schematic of a dusty slab illustrating the opacity when seen face- and edge-on.

selection criteria. In particular, the blue luminosity will be drastically underestimated (also in the case of a luminous extended host galaxy), and probably the (soft) X-ray power, too. At most, a Seyfert 2 type spectrum may remain recognisable and possibly polarised broad lines.

In conclusion, an edge–on PG quasar will appear to us like a luminous or ultra-luminous infrared galaxy, with an SED modulated by extinction even in the MIR; then the $F_{25\mu m}/F_{60\mu m}$ ratio will be lower than that observed for our sample (by factors which can easily reach values as high as 10).

Next we consider among which ULIRGs one should search for edge-on quasars. All of our detected PG quasars have high infrared luminosities and so-called *warm* MIR/FIR colours, $F_{25\mu m}/F_{60\mu m} > 0.2$, ranging from 0.3 to 1.25 with a median of about 0.5, whereby we corrected for the redshift effects. (For our objects a flux ratio of $F_{25\mu m}/F_{60\mu m} \approx 0.3$ typically corresponds to $L_{MIR} / L_{FIR} \approx 1$, whereby the details of such a conversion depend on the shape of the SED and on how steep the flux rises from the NIR to the FIR.) Therefore our result provides the sought after evidence for the reverse direction of the link between warm ULIRGs and quasars found by Sanders et al.(1988b): out of their bright ULIRG sample with warm MIR/FIR colours all 12 out of 12 sources showed optical signatures of quasars. Formally expressed – using the mathematical "⇒" and "⇐" symbols – we have now:

(a) warm U–LIRG $\Rightarrow$ optical quasar (Sanders et al.)

(b) warm (U)LIRG $\Leftarrow$ optical quasar (this work).

Since all ULIRGs with warm MIR/FIR colours show optical signatures of a quasar, the central region as well as the inner part of the torus in these ULIRGs cannot be heavily obscured in the MIR, and thus the optical extinction towards the centre might also be moderate ($A_V < 10$). This may even be the case for the famous extremely red and polarized quasar IRAS 13349+2438, the SED of which peaks in the MIR (Beichman et al. 1986, Wills et al. 1992, Wilkes et al. 1999). Thus, the warm infrared galaxies are probably quasars (AGN) preferentially seen face–on or at intermediate viewing angles, but not edge–on.

Thus, we arrive at the remarkable conclusion that edge–on quasars may appear to us not only as warm, but even as *cool* luminous or ultraluminous infrared galaxies with $F_{25\mu m}/F_{60\mu m} < 0.2$. However, not every ULIRG needs to house a hidden dust-enshrouded or edge-on quasar (or to evolve into a quasar).

Before searching for hidden radio-quiet quasars (Chapter 4), we will consider radio-loud quasars and their suggested edge-on counterparts, the radio galaxies (Chapter 3).

Chapter 3

Radio galaxies and quasars from the 3CR catalogue

3.1 Introduction

About 30% of AGN are radio-loud, having ratios of radio 5 GHz to optical B-band flux $F_{5GHz}/F_B > 10$. For our purpose here the following distinctive features of radio-loud AGN are relevant:

- Apart from the exotic BL Lac type objects, the radio-loud AGN are morphologically divided into core-dominated Fanaroff-Riley type FR 1 and lobe-dominated type FR 2. This morphological distinction is accompanied by a spectroscopic one: Typically the radio spectra of FR 1s are flat and those of FR 2s are steep. In both cases the radio emission is synchrotron radiation, but the flatness of the FR 1 spectra is due to relativistic beaming.

- The radio-loud AGN are divided by optical emission line properties into broad-line and narrow-line radio-galaxies, in analogy to the radio-quiet Seyfert 1 (or quasar) and Seyfert 2 types. A *broad-line radio-galaxy* is also called *radio-loud quasar*, while *radio galaxy* refers to one with narrow lines only.

The revised third Cambridge 3CR catalogue of about 170 sources (Bennett 1962a,1962b; Laing, Riley & Longair 1983) is selected at 178 MHz, a frequency at which most sources – radio galaxies as well as radio-loud quasars – are dominated by the very extended FR 2 radio lobes.

From a purely observational point of view, at least a dozen classes of AGN are discernible. On the conceptional side, however, there is widespread agreement that most, if not all, of these different objects contain a massive black hole ($M_{bh} \geq 10^6\,\mathrm{M}_\odot$) the accretion onto which is providing the main source of energy. It seems natural, to explain their differences with observational selection effects and thereby to reduce the number of intrinsically different object classes. Such selection effects could be differences in (1) the *circumgalactic environment*, (2) the *evolutionary phase*, or (3) the *aspect angle*. The aspect angle should be important, if AGN are not spherically symmetic objects. To disentangle the influence of these effects on the relation between various AGN (and to determine which effect dominates) is one of the major challenges of the current research.

In this chapter we will investigate the *unification of radio galaxies and quasars via aspect angle*, and, after the presentation of the infrared results we will have a quick look at the influence of *environment* and *evolution*. Note that here by the term *unification* we always mean the *purely geometric aspect angle unification*, and we do not unify via *environment* or *evolution* effects – as some people do.

3.1.1 Unified schemes – the principles for unification

Unified schemes try to unify various observational classes of quasars and radio galaxies as intrinsically similar sources, where the observed differences are due to *aspect-angle effects*. Thereby two mechanisms are important – the *beamed emission* and the *hiding dust torus*. This is illustrated in Fig. 3.1 using already new ISO results (Haas et al. 1998a, 1999):

- *Beamed emission*: A radio loud quasar with *flat* radio spectrum (e.g. FR 0234+28, 3C 279) is observed nearly *pole-on* so that a *beamed jet* with superluminal motion causes the bright radio and FIR appearance; a quasar with *steep* spectrum (e.g. 3C 48) is seen at an *intermediate angle* between pole-on and edge-on. In this picture, the reason for the aspect-dependent observational differences (in their radio and infrared spectra as well as their radio morphological appearance) is the *beamed emission*. This is the flat-and-steep spectrum quasar unification proposed by Orr & Browne (1982).

- *Hiding dust torus*: Seyfert 1 and Seyfert 2 galaxies represent the classical unification via a dust torus seen pole-on (=face-on) and edge-on, whereby the view towards the broad line region in the centre of the torus is hidden in the edge-on case. (Antonucci & Miller 1985). Radio quiet quasars (e.g. PG 0050+124) share the thermal properties of the radio loud ones, but the lack of magnetic fields near the central engine prohibits the development of a powerful jet which seems to be the origin of the strong synchroton emission. Radio quiet quasars and some ULIRGs (upper left corner in Fig. 3.1) may be unified as face- and edge-on members of the same population.

- The most radical unification is proposed by *combining* the phenomena *beamed emission* and *hiding dust torus*: A radio galaxy (e.g. 3C 405) is viewed nearly edge-on, whereby the nucleus contains an "optical quasar with broad emission lines" which is obscured behind a dust torus (Barthel 1989).

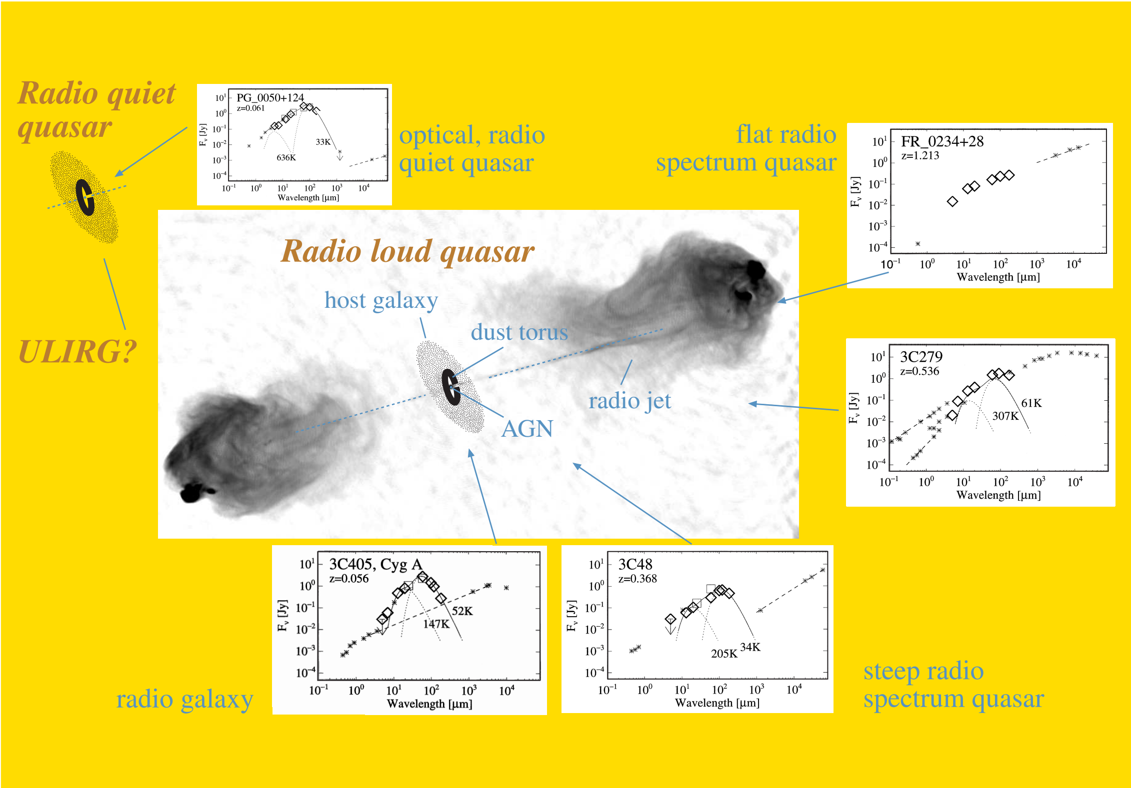

Figure 3.1: Illustration of the pure aspect-angle unification between ULIRGs and radio-quiet (PG) quasars, and the unification between flat and steep spectrum radio-loud quasars and radio galaxies. The image in the centre is a radio 6 cm map of Cyg A (as in Fig. 1.1). The arrows indicate the pole-on, intermediate and edge-on aspect-angles from which the observer looks at the system. The SEDs show the luminous mid- and far-infrared dust bumps rising above the smooth synchrotron spectra, which extend from the cm range into the infrared and are most prominent in the pole-on case, where they might outshine any thermal emission.

The unified schemes for radio-loud AGN are excellently reviewed by Urry and Padovani (1995). While both the unification of flat and steep spectrum radio-loud quasars and of Seyfert 1 and Seyfert 2 galaxies seem to be widely accepted, the unification of narrow-line radio galaxies (henceforth called *radio galaxies* or simply *galaxies*) and steep spectrum quasars (henceforth called *radio-loud quasars* or simply *quasars*) is still a matter of a controversial debate.

3.1.2 About to prove or disprove the unification

A disprove of the unification requires to demonstrate a difference in an extended or non-orientation-dependent quantity. For various samples the radio luminosity functions and the distributions of radio power versus linear size of the lobes show redshift-dependent differences between radio galaxies and quasars; they are mentioned as argument against the validity – or at least a dominating influence – of the unification (e.g. Singal 1993a, 1993b, 1996). These differences, however, can be affected by the evolution of the individual sources and their environments or by a change of the conditions during the cosmic evolution, therefore they constitute no real disprove of the unification. Furthermore, the selection criteria for creating *flux limited samples* may introduce a bias, when considering average properties. For example, beamed objects tend to be brighter, hence more numerous in a flux limited sample.

Proving the unification is even harder than disproving it, because demonstrations of similarity in arbitrary isotropic properties between the two classes of objects can only strengthen the case, but do not really constitute a proof. (In mathematical terms, they fulfill a necessary requirement, but not a sufficient condition.) In principle, suitable isotropic properties could be:

- the hard X-ray emission, with the proviso that it is still poorly known, how well it does penetrate the dust clouds,
- the mid-infrared emission from dust, with the proviso that part of the central emission could be absorbed by outer regions, hence the emission may not be ideally isotropic,
- the far-infrared emission from dust, with the proviso that FIR luminosity could also originate from starbursts, hence yields no direct implication on the strength of the AGN,
- the lobe luminosity at low radio frequencies (e.g. at 178 MHz), with the proviso that the lobe to AGN luminosity ratio could depend on the lobe environment, thus could vary from object to object,
- the emisson of narrow lines like [O II]λ3727 from a region which is compact but sufficiently extended to exceed the scale height of the obscuring torus, with the proviso that the [O II]λ3727 luminosity could also be provided mainly by stars, and not by the AGN.

There can be no doubt that a radio galaxy contains an AGN, since otherwise the jets powering the lobes cannot be explained. But the debate is on whether the AGN is of quasar-like stength. Thus – in order to prove the unification – the primary task is to reveal a hidden quasar in a (powerful) radio galaxy. The most direct evidence for a quasar hidden behind a dust torus can be obtained by spectropolarimetry, when broad high exitation lines show up as light scattered in the bipolar cones with polarisation angle perpendicular to the polar axis. Despite a growing number of positive detections (Hill et al. 1996), huge extinction could have prevented success in numerous attempts (Hill et al. 1996). Therefore, an alternative more indirect strategy is, to verify the existence of the dust, which hides the quasar in the supposed edge-on type. This can be done by two ways: in the optical by searching for the signatures of dust extinction, or in the infrared by detecting the dust emission.

3.1.3 Status in the optical: pro unification

There are at least three ways, which lead to anisotropic optical emission, namely (1) relativistic beaming, (2) seeing different amounts of a disk surface according to inclination, or (3) orientation-dependent obscuration (Jackson & Browne 1991). It is not yet clear, how far each of the anisotropic processes does affect the optical appearance observed. Nevertheless, important cornerstones have recently been achieved in the optical. Here we focus on the interplay between the [O II]λ3727 line, the [O III]λ5007 line and the continuum:

Hes et al. (1996) showed that the [O II]λ3727 line luminosity is on average similar for 3CR radio galaxies and quasars, consistent with the unification. As mentioned above, the concern is, whether the [O II] emission, in fact, has to be assigned to the narrow line region surrounding the AGN, then serving as indicator for the AGN strength. Nevertheless, the value of these results is emphasized by the following context.

Further optical findings support the unification, although also indirectly: In contrast to [O II]λ3727, the [O III]λ5007 line is slightly stronger in quasars than in radio galaxies. The [O III]λ5007 line requires a ten times higher excitation potential which is more indicative of an AGN. If it originates closer to the AGN, then it will be more obscured behind an inclined dust torus, as is observed in accordance with the unification (Hes et al. 1996, Baker 1997).

Remarkably, when considering exclusively quasars, but at a range of different inclination angles, the [O II]λ3727 / [O III]λ5007 line ratio declines with increasing angle between radio axis and line-of-sight. (This angle is inferred from the radio geometry and the core-to-lobe ratio.) The best explanation for this smooth aspect-angle dependence is *extinction by dust* (Baker 1997). And the crucial point with respect to the galaxy-quasar unification is, that the radio galaxies lie just at the smooth continuation of the [O II]λ3727 / [O III]λ5007 line ratio for inclined (i.e. nearly edge-on) quasars, again consistent with the unified model.

The same aspect-angle dependence holds also for the [O II]λ3727 and [O III]λ5007 *equivalent widths*, suggesting that actually the strong continuum typical for an AGN is reduced (in the intermediately inclined quasars compared with the face-on ones) – again in accordance with the unification.

Despite some reservations, the optical studies provide growing evidence for aspect dependend dust extinction of the nuclear region. They could not find substantial arguments against the unification. Furthermore, if the extinction explanation is correct, then the reemission of dust should really be seen in the infrared.

3.1.4 Status in the infrared: contra unification?

An attractive check of the unification is offered via the mid- and far-infrared: If the mid- and far-infrared emission of the dust torus is optically thin and isotropic, then it should show up in the SEDs of all members of a unified class, irrespective of aspect-angle. Previous mid- and far-infrared observations, however, did not yet reach sufficient sensitivity to allow for a meaningful conclusion:

Heckman et al. (1992) could detect only 6 out of 117 radio galaxies and quasars in the $12-100\,\mu$m IRAS data of their sample of 3CR sources with $z > 0.3$. Therefore, they superimposed all IRAS maps of the radio galaxies and quasars, respectively, constructing averaged "super-maps" of the IR emission from the two samples. 3CR *quasars* on average are four times more luminous at 6 to $50\,\mu$m (in the AGN rest frame) than a comparable sample of *radio galaxies*. At a first glance, this is in pronounced contrast to the expectation from the unified schemes which are positively indicated by the optical studies. Also, at low redshift $0.05 < z < 0.3$ the *quasars* (i.e. to be precise: the broad line radio galaxies out of which only a few exhibit the optical power of a quasar) are about 4 times more luminous at 12 and 25 μm than the *galaxies*, but the difference between galaxies and quasars becomes smaller at 60 and 100 μm (Heckman et al. 1994). Also, Hes, Barthel & Hoekstra (1995) found that only 6% of the 3CR radio galaxies at $0.3 < z < 0.8$ but 37% of the quasars are detected on the recalibrated IRAS scans. In order to stay in line with the unification, as an explanation for the IR difference between quasars and radio galaxies Hoekstra, Barthel & Hes (1997) proposed that the FIR and possibly also the MIR emission is considerably caused by a beamed synchrotron component, resulting in a higher IR luminosity for quasars than for galaxies.

But why did these investigations not see the emission from the hiding dust? The wavelength coverage and sensitivity of the IRAS data were not sufficient to discriminate between dust and synchrotron emission, hence to correct for the contribution by a beamed synchrotron component to the mid- and far-infrared spectra of the quasars. The importance of a sufficiently large wavelength coverage e.g. from $1-1000\,\mu$m is clearly illustrated in Fig. 3.1. Also, the "super-maps" could severely be biased by fine-structure in the galactic cirrus such that one single object located in a low cirrus region could dominate the whole sample. Hence, the status in the infrared is indefinite, neither confirming nor discarding the unification. Therefore more sensitive observations (and a larger wavelength coverage) are needed as expected from ISO.

Table 3.1: Measured fluxes in mJy.
The sources are ordered along the pairs as shown in Fig. 3.2. The ISOPHOT observing modes (column 2) are: c = chopping with P1–C200, m = mapping with all detectors P1–C200, b = both: chopping with P1–C100 and mapping with C200 detetctors. Bold numbers are detections above the 3–sigma level, the thin numbers represent non-detections which are shown as 3σ upper limits in Fig. 3.2. The * indicate sources also detected with IRAS.

Name	obs	4.8 μm	7.3 μm	12.8 μm	20 μm	60 μm	100 μm	120 μm	170 μm	180 μm	1300 μm
3C 405*	b	1± 4	**40± 1**	**250±36**	**590± 59**	***3034±56**	**2155± 57**	**994±216**	337± 200	**419±100**	
3C 48*	b	6± 7		**104±34**	-23± 82	***460±85**	**829±113**	**739±239**	**554±142**	**550±165**	
3C 20	b	-17± 4	-2±12	-74± 35	-73± 28	**97±26**	140± 92		**167± 17**		
3C 273*	c			*		***1124±86**	***1348± 68**	**1546± 94**	**1292± 21**	**1056± 75**	
3C 295	c	**16± 4**	-1± 9	42± 64	-218±122	**157±26**	**155± 19**		106± 37		**19.1±0.9**
3C 47*	b	0± 3		27± 13	-22± 15	***103±30**	***169± 53**		**164± 25**		
3C 427.1	c	1±16	0± 5	-25± 38	36± 25	37± 45	72± 68		-1867± 60		0.7± 0.7
380	m	-1± 3	2± 1	-8± 7	-39± 36	**54±16**	**56± 16**		**83± 20**		**514.9±2.4**
3C 325.0	c	17±13	3± 6	-29± 25	-84± 27	**160±52**	**140± 19**		27± 42		0.4± 0.6
3C 138	m			8± 9	56± 69	13± 42	25± 37		27± 39		
280	c	-3± 1	-1± 4	26± 22	-10± 68	66± 31	58± 63		34± 77		**14.7±1.0**
3C 286	c	6± 3		41± 31	-1± 39	**142±34**	**126± 39**		35± 62		**233.4±3.5**
3C 368	c	**6± 2**	**8± 2**	22± 40	-52± 54	**94±24**	72± 48		80± 56		0.14± 0.6
3C 309.1	c	**22± 5**	13±13	18± 62	-85±162	**100±10**	-14± 48		272± 91		**266.6±1.7**
324	c	3± 2	0± 1	0± 11	37±194	-29± 34	53± 77		236± 79		0.5± 0.6
3C 287	c	-5± 6		20± 23	34± 42	-33± 52	-89± 26				**81.2±1.4**
3C 65	c	**10± 2**		7± 41	-10± 20	**129±18**	-19± 43		38± 33		
3C 298*	c	1± 4		**23± 4**	**29± 9**	***184±24**	**213± 39**		**243± 59**		**14.1±0.8**
3C 437	c	1± 7	-2± 4	45± 34	-23± 46	-31± 42	5± 82		-6± 63		
3C 9	c	7± 3		27± 14	9± 75	-16± 48	-68± 82		-148± 109		

3.2 The data

The *ISO European Central Quasar Programme* contained 10 galaxy/quasar pairs selected from the 3CR catalogue such that both the isotropic 178 MHz luminosity and the redshift match as close as possible between the radio galaxy and the quasar in order to minimize effects of cosmic evolution. (Due to visibility constraints during the execution of the observations the originally intended pairs had to be replaced, and the actually obtained pairs do not match ideally, therefore it makes sense to soften the matching conditions and to compare now groups with similar redshift only.)

The photometry with ISOPHOT between 5 and 180 μm was complemented for 11 sources by 1.3 mm observations with the 30 m IRAM telescope in order to constrain the synchrotron contribution.

3.3 Spectral energy distributions (SEDs)

The IR and mm fluxes are listed in Table 3.1. The spectral energy distributions (as measured, not corrected for redshift) are shown in Fig. 3.2 supplemented by data from the literature (a complete reference list is given in Meisenheimer & Haas et al. 2001). They

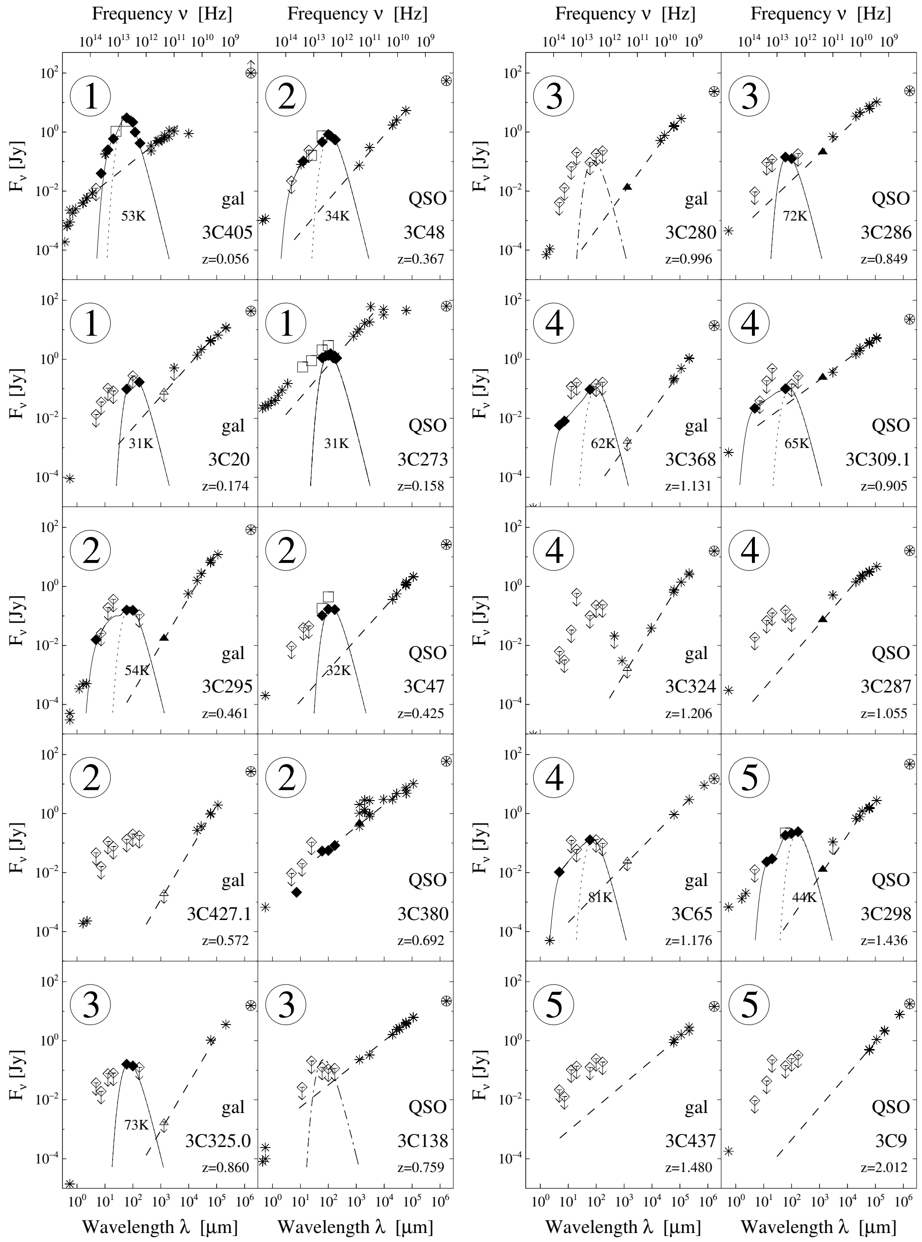

Figure 3.2: Observed spectral energy distributions of the pairs of 3CR radio galaxies and quasars ordered according to the redshift of the galaxy. The photometric errors are less than 30%. The large encircled number in the upper left corner denotes the group for an alternative matching. Symbols as in Fig. 2.1. Filled diamonds refer to the ISOPHOT detections, filled triangles to IRAM measurements, while open diamonds indicate 3σ upper limits. IRAS detections are shown by open squares. Stars give flux measurements at optical and radio wavelengths which refer to the central source. The exeption are the *encircled stars* which represent the total flux at 178 MHz from the 3CR catalogue. The long–dashed lines indicate the synchrotron contribution as extrapolated from radio and mm data. Several λ^{-2} modified blackbodies are fitted to the data (solid lines) and only the coldest components are plotted individually (dotted lines). Their temperature values refer to the restframe of the object. In cases of non–detection of one member of a pair (3C138, 3C280), the dashed–dotted line illustrates, how the blackbody of the "partner" would show up at corresponding redshift and that it would not exceed the upper limits.

may look quite noisy to a non-expert, but they constitute really a novum in infrared astronomy. In particular, they allow impressively to separate synchrotron and dust emission:

In six out of six radio galaxies and at least four out of seven quasars detected the mid-to-far-infrared SEDs exhibit a “thermal bump” well in excess above the synchrotron emission. In all seven cases for which we derive only upper limits, these limits still allow for the presence of a stong thermal bump well above the synchrotron component.

In one case (3C 380) only synchrotron emission is identified even in the mid-to-far-infrared showing up as smooth continuation from the longer wavelength range. 3C 380 has the flattest spectrum among our sample, with a far-infrared luminosity of about $L_{40-150\mu m} > 10^{12}L_{\odot}$. Within the measurements errors a thermal component of 10% of this luminosity would not be discernible, therefore even a luminous ($10^{11}L_{\odot}$) dust component could easily be hidden underneath.

Modified blackbodies with emissivity proportional to λ^{-2} are fitted to the data. In the cases with good signal to noise ratio the dust emission has to be fitted by more than one single blackbody in the temperature range from hot dust at about 500 K down to cold dust at about 30 K. The mass of the dust lies in the range 10^6 – $5{\times}10^8$ $M_{\odot}$. Both temperature and mass range are similar as for the dust seen in the PG quasars.

Table 3.2 lists derived dust parameters like luminosities, temperatures and masses.

3.4 Evidence favouring unification

The striking result from our SEDs is the high detection rate of a thermal dust bump in both the radio galaxies and the radio-loud quasars. This is certainly a cornerstone in infrared astronomy, compared with the meager findings by the former infrared missions. The ISO data strongly favour the role of unification for describing the relation between radio galaxies and quasars. The arguments are:

3.4.1 Balanced detection statistics

The overall detection statistics for the radio galaxies and quasars in our sample are indistinguishable: Among the 10 pairs we found 5 for which both the quasar and the radio galaxy is detected, one with only the quasar, and one with only the radio galaxy being detected. In the remaining 3 pairs we could neither detect the quasar nor the galaxy. Note, that all detected sources show a significant signal at least in one of the 60 and 100 μm bands. (It should be stressed that the observing conditions are similar and well balanced for the radio galaxies and quasars of our sample, as illustrated in Figures 6.5, 6.6 and 6.7 of section 6.2.)

Also, the presence of a dust bump is statistically balanced for the radio galaxy – quasar pairs. Most of these pairs are well matched both in extended radio luminosity and redshift. Some pairs in Fig. 3.2 do not match, e.g. 3C 405 – 3C 48 and 3C 437 – 3C 9, because for

Table 3.2: Luminosities, dust temperatures and masses.
The sources are ordered along the pairs as shown in Fig. 3.2. The luminosity distance is determined as $D_L = c / H_0 * (z + z^2 / 2)$, i.e. $q_0 = 0$, with $H_0 = 75$ km/sec/Mpc. $P_{178MHz} = 4\pi D_L^2 F_{\nu=178\,MHz}$. The infrared luminosities L_{IR} (3-1000 μm), L_{MIR} (3-40 μm) and L_{FIR} (40-1000 μm) are computed from the blackbody curves shown in Fig. 3.2. L^{syn} denotes the synchrotron luminosity in the FIR range (60-100μm) and the mm range (100-10000μm) as shown by the long–dashed lines in Fig. 3.2. The wavelength ranges refer to the restframe of the objects. T_d refers to the coldest dust component derived from the decomposition of the SED. The dust mass M_{dust} is estimated according to Hildebrand (1983).

Name 3C	**z**	$\mathbf{D_L}$ Mpc	$\mathbf{P_{178MHz}}$ 10^{26} W / Hz	$\mathbf{L_{IR}}$ $10^9\,L_\odot$	$\mathbf{L_{MIR}}$ $10^9\,L_\odot$	$\mathbf{L_{FIR}}$ $10^9\,L_\odot$	$\mathbf{L^{syn}_{FIR}}$ $10^9\,L_\odot$	$\mathbf{L^{syn}_{mm}}$ $10^9\,L_\odot$	$\mathbf{T_d}$ K	$\mathbf{M_{dust}}$ $10^6\,M_\odot$
405	0.056	230	552	399	215	184	2.8	12	53	4
48	0.367	1736	197	7623	5011	2612	7.1	78	34	400
20	0.174	756	31	142	5	137	1.2	12	31	48
273	0.158	681	35	289	8	281	140.9	1497	31	106
295	0.461	2267	513	1261	444	817	0.6	36	54	16
47	0.425	2060	135	673	25	648	2.7	28	32	199
427.1	0.572	2940	274	—	—	—	0.1	7	—	—
380	0.692	3723	984	—	—	—	367.9	1827	—	—
325.0	0.860	4916	452	5871	3670	2201	0.3	17	73	13
138	0.759	4185	467	—	—	—	239.3	1142	—	—
280	0.996	5964	1007	—	—	—	8.7	168	—	—
286	0.849	4834	699	5023	3140	1883	220.5	1634	72	11
368	1.131	7077	826	17797	14824	2973	1.1	24	62	28
309.1	0.905	5254	479	19977	18372	1605	442.2	1982	65	13
324	1.206	7728	1127	—	—	—	1.0	50	—	—
287	1.055	6442	811	—	—	—	87.6	970	—	—
65	1.176	7465	1015	33079	30333	2746	47.1	379	81	10
298	1.436	9861	5528	54941	40793	14148	16.1	475	44	565
437	1.480	10294	1853	—	—	—	233.5	1279	—	—
9	2.012	16133	5543	—	—	—	56.3	665	—	—

practical reasons they were formed out of loose ends of the actually observed sample. For these the discrepancies are reduced, when the strict pairwise matching is softened allowing for groups which match primarily in redshift; this results also in reasonably comparable luminosities. The group matching is indicated by the encircled numbers in Fig. 3.2. Then for example group 2 allows for a better matching of 3C 48 with 3C 295 and 3C 47 (instead of matching 3C 48 with 3C 405).

3.4.2 Balanced dust luminosities

The dust luminosities of the 3CR radio galaxies and quasars are statistically very similar, ranging from 10^{11} to $3 \cdot 10^{13}\,\mathrm{L}_\odot$ for the radio galaxies and $6 \cdot 10^{11}$ to $5 \cdot 10^{13}\,\mathrm{L}_\odot$ for the quasars. Bearing in mind that for the PG quasars the dust luminosity shows also large dispersion over three orders of magnitude from 10^{11} to $10^{14}\,\mathrm{L}_\odot$, the 3CR sample is in good statistical agreement with the expectation of the unified schemes.

3.4.3 Synchrotron contribution in the infrared: higher in quasars than in galaxies

The beamed synchrotron spectra may continue well into the mid- to far-infrared wavelength region (3C 273, 3C 380, 3C 309.1, and propably 3C 138 and 3C 286). Remarkably, the synchrotron extrapolation of the quasars in our sample is – on average – more than ten times brighter in the FIR than that for the radio galaxies (see Table 3.2). This is consistent with the unified schemes, which predict that the jet axis of quasars is oriented more towards us, resulting in observing a stronger beamed component. This could also explain, why on the IRAS scans the quasars showed a higher detection rate than the radio galaxies.

3.4.4 Consistency with other ISOPHOT observations

If we expand our sample by including the four radio galaxy – quasar pairs which have been observed with ISOPHOT by van Bemmel et al. (2000, 2001), and have been selected and evaluated along identical lines as ours, we end up with 7 pairs in which both the radio galaxy and the quasar is detected, 3 pairs with only the quasar, and 1 pair with only the radio galaxy being detected. Thus, also the expanded sample is in good agreement with the unified schemes.

The detection statistics for the extended 3CR *radio galaxies* is about 8/14. This is consistent with the value of about 20/37 found by Fanti et al. (2000) for their ISOPHOT observations of other radio galaxy samples[1]. This demonstrates also that radio galaxies do well contain dust which is a prerequisite for hiding a quasar.

Some of our 3CR sources are detected only in the FIR, but not in the MIR, e.g. 3C 20 or 3C 47. But this does not provide any evidence against unification. Note, for a high optical depth as may be the case in "edge-on" radio galaxies the observable MIR emission will be reduced due to extinction. As for the PG quasars, the FIR luminosity in the 3CR sources could be powered mainly by starbursts. The PG quasars exhibit a good correlation between the mid- and far-infrared luminosities. If this is also the case for the 3CR samples,

[1] Fanti et al. investigated two samples of steep spectrum radio galaxies with similar redshifts and radio powers, one of compact and one of extended sources in order to find evidence for the youth of the compact ones, by successfully excluding the competing "frustration" scenario.

then from a FIR detection one may infer also significant intrinsic MIR luminosity caused by a powerful AGN.

In conclusion for the whole section 3.4, the mid- and far-infrared emission of quasars and galaxies seen by ISO is in full agreement with the expectations from the unified schemes.

3.5 The dust-to-lobe luminosity ratio

If the relation between radio galaxies and quasars is perfectly described by the unified schemes, then not only the detection statistics (and other properties as in section 3.4), but also the emitted dust power should be the same for objects of identical lobe luminosity. Thus the ratios of the dust to radio emission: $\mathrm{R_{dr}} = \nu\ \mathrm{F}_\nu$ (FIR) / $\nu\ \mathrm{F}_\nu$ (radio) and – in case of moderate opacity in the MIR – also $\mathrm{R_{dr}} = \nu\ \mathrm{F}_\nu$ (MIR) / $\nu\ \mathrm{F}_\nu$ (radio) should be identical for galaxies and quasars. In this section we investigate this ratio.

3.5.1 Balanced distributions: further evidence for unification

Fig. 3.3 displays this ratio for two rest frame wavelengths, for which the fluxes are carefully inter- and extra-polated from the SEDs. The wavelength and frequency ranges refer to the restframe of the objects. The restframe MIR fluxes at e.g. 24 and 40 μm can quite accurately be determined from the observed fluxes, and also the restframe FIR fluxes at e.g. 60 and 100 μm. For the high redshift sources the restframe 178 MHz flux, however, has to be extrapolated from the observed SEDs (see Fig. 3.2), with some uncertainty. Therefore, we show in Fig. 3.3 (left) also a slightly shorter radio wavelength (higher frequency) for which the flux can be interpolated with higher accuracy. We chose 433 MHz which arises from shifting the observed 178 MHz to the restframe of 3C 437 at z = 1.480. In both cases of Fig. 3.3 we cannot find any remarkable difference between the distribution of quasars and galaxies – again in agreement with the unified schemes. (Actually some small differences exist and are discussed in section 3.5.4 below.)

The lobe power and the dust luminosity agrees within factors of a few, independant of the classification as quasar or galaxy. This small dispersion is particularly remarkable, since the dust luminosity spans about three orders of magnitude.

A strong exception in Fig. 3.3 is 3C 405 (Cygnus A) with $R_{dr} < 10$, but this source has exceptionally bright radio lobes (Barthel & Arnaud, 1996). This confirms the conclusion by Barthel & Arnaud, that radio luminosity is not generally a good measure of AGN power. Also 3C 380 and 3C 295 deviate from the bulk of the sources, and we discuss now the reasons for this.

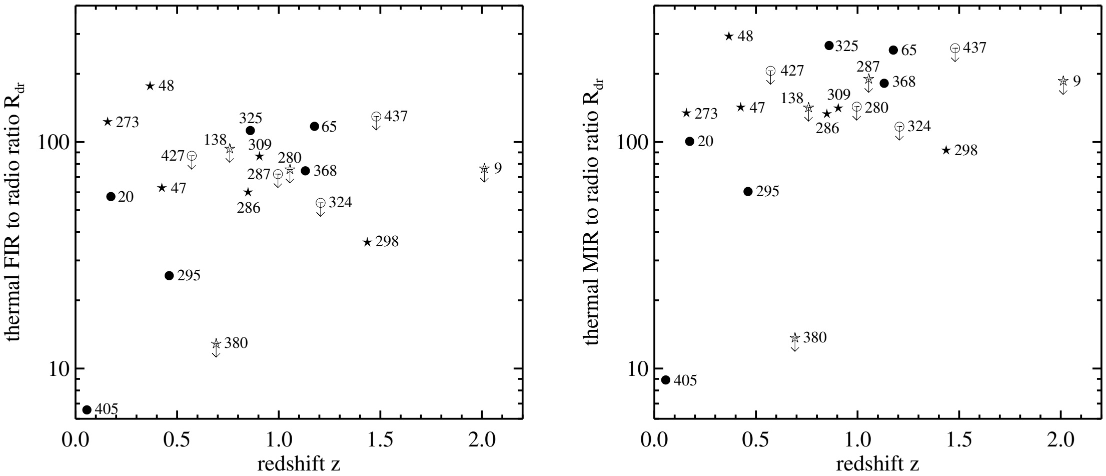

Figure 3.3: Ratio R_{dr} of thermal dust power νF_ν to radio power, both interpolated/averaged in the rest frame of the sources at the following wavelengths: IR 60 and 100 μm, radio 178 MHz *(left panel)*; IR 24 and 40 μm, radio 433 MHz *(right panel)*.

3.5.2 Environment and evolution: New prospects for exploring their influence

The ISO data suggest, that the mid- and far-infrared luminosities actually yield good estimates for the strength of the AGN. With this in mind and accepting that the unified schemes are basically valid, sensitive infrared measurements offer a unique opportunity: deviations in the dust-to-lobe luminosity ratio allow now to explore the influence of environment and evolution onto the extended radio lobes. (By evolution we mean not the cosmic evolution, but only the evolution of the lobes of an individual galaxy.)

Then in Fig. 3.3 not only 3C 405 but also the galaxy 3C 295 and the quasar 3C 380 lie at the low end of the R_{dr} distribution, indicating high efficiency in creating the radio lobe luminosity. Note that 3C 295 is located in a dense X-ray bright cluster like 3C 405, confirming the influence of the environment in enhancing the lobe power. Also 3C 380 is peculiar in that it shows both a relatively flat radio spectrum probably seen pole-on and bright FR 2 lobes. A possible way out of this dilemma is that there is an intrinsic bend in the jet (cf. Wilkinson et al. 1991). In this case a strong interaction with the circumgalactic medium may provide an extraordinarily high radio luminosity, too.

3.5.3 On selection effects

So far, the IR observations and the strategy was successful in showing the intrinsic similarity of radio galaxies and quasars. Our strategy was, to match pairs taken from the whole

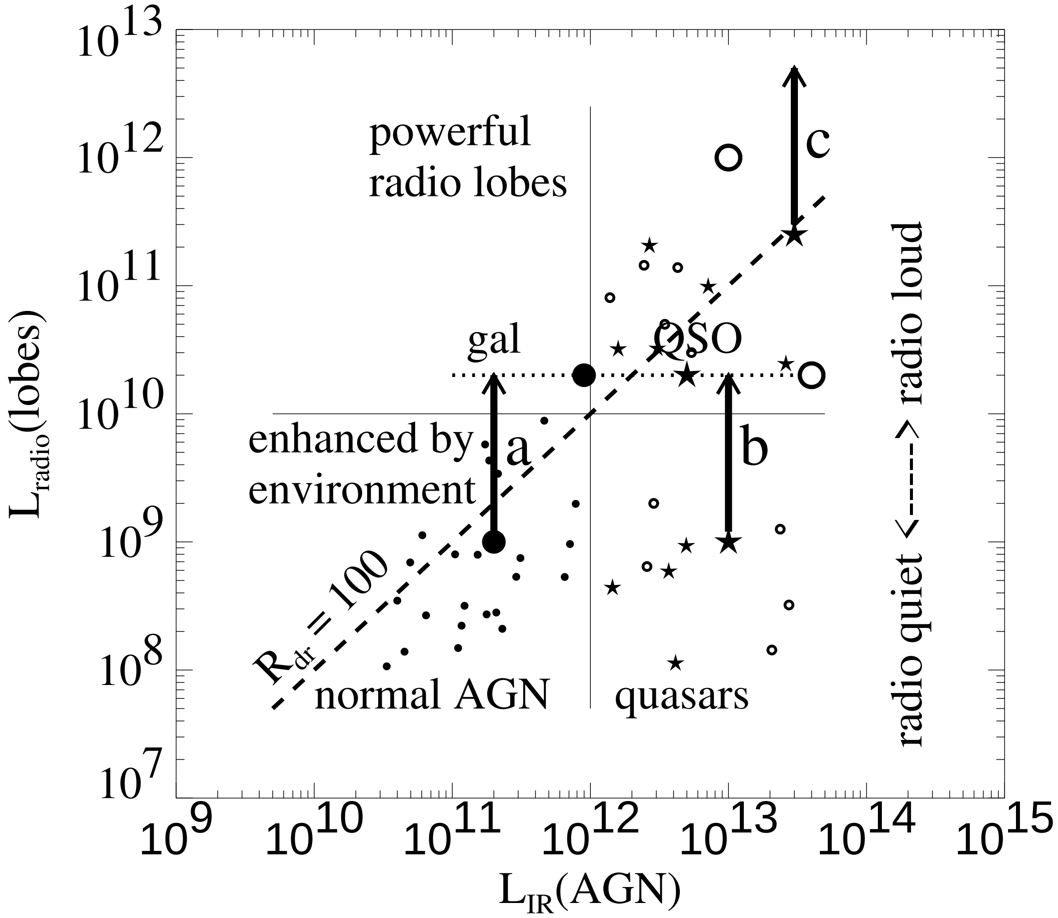

Figure 3.4: Schematic diagram of radio luminosity against dust luminosity, in order to illustrate possible selection effects, when unifying radio galaxies and quasars. The position of the objects represented by the small symbols was generated randomly. The symbols are: $\star$ = quasar, $\circ$ = edge-on quasars (radio galaxy with powerful quasar-like AGN), $\bullet$ = radio galaxy with less powerful 'normal' AGN (irrespective of aspect angle).

3CR radio galaxy and quasar catalog according to some properties which are believed to be isotropic. But, one objection against this strategy has to be mentioned: The matching condition does not care about the properties of the entire sample. Therefore a balanced subset can be selected, which needs not to be representative for the whole sample, hence the selection can introcude a bias.[2]

[2]Sometimes it is instructive to consider examples from different fields, therefore here look at one from biology: Imagine two samples, men and women. Do men and women intrinsically have the same body heights, which depending on aspect angle could appear different to an observer? Select two subsamples from the whole samples, such that each man – woman pair matches in let's say the diameter of the fist

There can be no doubt, that the evolution of the lobes and the circumgalactic environment influence the radio luminosity. Then we have certainly to deal with selection effects, when trying to unify radio galaxies and quasars. In order to get a feeling for possible selection effects we consider the distribution of AGN IR luminosity and lobe radio luminosity among radio galaxies and quasars. This is schematically shown in Fig. 3.4.

First we consider in Fig. 3.4 only the effects of evolution and environment: An individual radio-loud object evolves out of a radio-quiet one. During this evolution it migrates in the diagram from bottom to top. (Actually on cosmic time scales the evolution is fast like a flash, and for sake of simplicity we may assume here also that it proceeds monotonically.) For average circumgalactic environments this evolution may last until the object reaches the long-dashed diagonal line with a $R_{dr} = 100$ (which we may call the maximal R_{dr}, when we ignore here for the moment that the lobe power can decline during the expansion). This migration is in principle the same for powerful AGN (quasars) and for less powerful 'normal' AGN (distinguished by a thin vertical line at $10^{12}\,L_\odot$ in Fig. 3.4)

In special circumgalactic environments the lobe power may be enhanced extraordinarily. This is indicated by the thick vertical arrow for example objects labelled *a,b,c* in Fig. 3.4. Then a 'normal' AGN can produce powerful radio lobes lying above the average R_{dr} line (case *a* in Fig. 3.4). We do not consider here the open question, how strong the enhancement by environment can be. In order to understand the selection effects, only the phenomenon of the vertical arrows is important.

Targets with powerful radio lobes lie above the thin horizontal line at $10^{10}\,L_\odot$ in Fig. 3.4. When selecting such targets for testing the unification, they are put into two categories: (1) 'QSO', if the broad emission lines are seen and the AGN luminosity exceeds $10^{12}\ L_\odot$, (2) 'gal'= 'non-QSO', otherwise.

Two reasons may lead to a classificaton as 'gal':
(1) the broad line region is hidden (unification, *open* circles in Fig. 3.4), or
(2) the AGN is relatively weak (environmentally enhanced lobes, *filled* circles in Fig. 3.4).

An environmental enhancement of the lobe luminosity can of course also occur for a QSO. Remember that our strategy for testing the unification was, to create a gal – QSO pair matching in lobe luminosity (indicated by the dotted horizontal line in Fig. 3.4). But, in order to be matched via lobe luminosity with a galaxy, such a QSO – if it were not environmentally boosted – would intrinsically be in a rather radio-quiet ('unevolved') phase (case *b* in Fig. 3.4). In any case a radio source, which is by other criteria known to be a quasar, will show on average a higher IR luminosity than a source not known to be a quasar.

If a QSO with *powerful* radio lobes is environmentally boosted, then both its AGN

which is more or less round and isotropic. Measuring now among the pairs the body heights, they will appear statistically indistinguishable. Although this test looks at a first glance promising, it actually fails in providing a correct proof. The men are on average taller than the women.

IR and radio lobe luminosities are extremely high (case *c* in Fig. 3.4). If such a QSO is matched via lobe luminosity with a galaxy, then also the AGN IR luminosity of the galaxy might be of quasar-like strength.

Of course, this schematic investigation is a simplification. But it emphasizes the influences of evolution and environment on the lobe luminosity and the dust-to-lobe ratio. With respect to our gal – QSO pairs the most important conclusion is: the galaxies may be expected to show on average a lower dust-to-lobe luminosity ratio than the quasars. This is due to evolution of quasars from radio-quiet to radio-loud objects and it depends also on the strength of environmental lobe boosting. Depending on the relative contribution of the environmental enhancement, the difference in R_{dr} between galaxies and QSOs may become stronger at low luminosities. Note, however, that these effects cannot disprove the unification, i.e. that galaxies are in principle edge-on quasars.

3.5.4 Deviations from balanced distributions: the remaining puzzle

The dust-to-lobe ratio (Fig. 3.3) exhibits two deviations from perfectly balanced distributions for galaxies and quasars. However, since our sample is too small, they are not statistically significant and they may be caused by selection effects, too.

Firstly, in Fig. 3.3 both diagrams are underpopulated in their lower right corner. And one could ask, why we do not see objects like 3C 405 at high redshift. Apart from the small number statistics, this can be explained as purely sensitivity based selection effect:

If the distribution originally fills also the lower right part of the diagrams, then our 3CR sample selected first only those sources which are bright in the radio regime, and in a second step among them only those sources, which are also bright in the IR, are detected, too. Among the nearby ones the sensitivity of ISOPHOT is sufficient so that the full infrared luminosity range is seen, but among the high redshifted ones only those at the luminous end are detected; the other less luminous ones will occur only as upper limits in the infrared, resulting in an empty lower right corner of the diagrammes.

It is not necessary, to invoke a cosmological explanation (which was discussed in Meisenheimer & Haas et al. 2001), even if it appears to fit currently the so-called *alignment effect* (Chambers et al. 1987, McCarthy et al. 1987). Its origin and redshift dependence are a matter of debate, too. Bearing in mind the diversity of influences on the alignment effect and the smallness of our sample, this subject is not considered further here.

Secondly, in both diagrams of Fig. 3.3 at low redshift ($z < 0.5$) only quasars reach the middle and high values of $R_{dr} \gtrsim 100$. Apart from the small number statistics, again this can be understood as selection effects (whereby e.g. the evolutionary status of the lobes could also come into play, see section 3.5.3):

(1) When selecting a powerful radio galaxy, then we know that it is "most efficient" in creating the radio power, but we do not know about its AGN strength. Bearing in

mind the dispersion of dust luminosity, it is likely to pick out a radio galaxy which has an infrared luminosity which is not as "optimized" as the lobe power, hence R_{dr} is biased to lower values (case *a* in Fig. 3.4).

(2) Similarly, an inverse trend may occur for the selection of the quasars: There are radio-quiet as well as radio-loud quasars, and the R_{dr} distribution fills a large and steady range. The radio-quiet quasars lie around or above the upper end of the R_{dr} distribution in Fig. 3.3. As a consequence, when selecting a radio-loud quasar, we know already that the central machine is "optimized", but the radio lobes may not yet work at highest efficiency (even for case *b* in Fig. 3.4, since the environmental enhancement is diminuished by the not yet finished evolutionary bottom-to-top migration). Therefore it is likely to choose one with an intermediate or high R_{dr}, and it is unlikely to choose one with low R_{dr}.

Thus selection effects can well explain that at low redshift the quasars populate a higher R_{dr} regime than the radio galaxies.

To conclude from the entire section, the dust-to-lobe luminosity ratio offers new prospects to study – in addition to the unification – the influence of environment and evolution onto the radio lobes. Future observations of larger samples may be able to obtain more definite quantitative results.

3.6 The revised picture in the infrared: substantial role of unification

The new SEDs provide crucial evidence that *unification plays a substantial role in relating radio galaxies and quasars*. Thus the ISO data led to a strong revision of the incomplete picture drawn from insufficient former infrared data.

At the same time, when looking at the radio maps, it becomes clear that the jet and lobe phenomena, which are full of beautiful details, are of course also strongly influenced by the circumgalactic environment and by evolution. Therefore it it is not appropriate, to consider the three "principles" *unification*, *environment* and *evolution* on an exclusive either–or basis in order to describe the relation between radio galaxies and quasars. Rather the interplay of all three principles helps to understand radio galaxies and quasars which belong certainly to the greatest phenomena in the universe.

Chapter 4

Search for hidden quasars among Ultra-Luminous InfraRed Galaxies

4.1 Introduction

In the last two Chapters we have seen that hidden (edge-on) quasars may well exist. Thereby 'hidden' means that the optical tracers 'high blue luminosity' and 'broad high excitation lines' characteristic for a quasar are not directly seen.

The argumentation and the strategy for providing evidence for hidden quasars differs for radio-quiet and radio-loud objects:

Among radio-loud objects, i.e. the radio galaxies, the powerful lobes leave not doubt for the presence of an AGN, and the high (central) infrared luminosity provides evidence that the AGN is actually of quasar-like strength, i.e. the radio galaxy houses a quasar.

Among radio-quiet objects, however, the situation is more challenging. Despite the prediction – and already some successful findings – of quasars hidden behind an edge-on dusty disk or torus, a general consensus about their existence is only slowly growing: evidence for a radio-quiet quasar requires in addition to a high infrared luminosity also the detection of direct tracers for a powerful AGN. But to provide these tracers seems to be surprisingly difficult. Therefore in this chapter we follow a different more indirect strategy, namely to prove the existence of hugh extinction in (some) ultra-luminous infrared galaxies (ULIRGs), so hugh that the dereddend central luminosity density can only be explained by a quasar. It should be stressed that the challenge in this chapter is to probe really high extinction in the order of $A_V \gtrsim 100$ and not just common low values of $A_V \lesssim 10$.

Firstly, we consider some previous attemps to find hidden quasars. Optical, NIR and even MIR observations are more or less hampered by dust extinction, therefore their capability to probe dust enshrouded AGNs is limited. Also, it is not yet established, how far the hard X-rays which are good AGN tracers may be absorbed. For the quite efficient AGN search in the 2MASS survey via NIR colours (J-K$\,>2$, Nelson et al. 1998), the absorbing dust might be organized in a disk allowing for the NIR radiation to escape along the less extinguished pole directions. This shows that in most cases, where an AGN has been identified, the extinction is sufficiently moderate (at least along the lines of sight towards suitable regions), so that the AGN signatures can be seen in the X-ray, optical and NIR regimes as well. At MIR wavelengths, unfortunately, the ISOSWS high resolution spectroscopy of ULIRGs was not sensitive enough, resulting mostly in upper limits for the high excitation lines like 14.3μm Ne[V] or 25.9μm O[IV] (Genzel et al. 1998), and no really hidden *new* AGN or quasar has been found.

AGN have been detected so far only in about a third of the nearby ULIRGs (Genzel et al. 1998), in the remaining two thirds they may have escaped detection due to enormous extinction (Sanders 1999). Most of the known AGN are pronounced MIR emitters, having *warm* mid-to-far-infrared colours ($F_{25\mu m}/F_{60\mu m} > 0.2$) which themselves serve as tracer for an AGN. Thus, the extinction required to hide an AGN must be very high, suppressing the total MIR continuum and providing *cool* mid-to-far-infrared colours. But so far no technique is known to probe the *entire* MIR extinction properly.

When the amount of extinction is determined *exclusively* from data, which are themselves affected by extinction – like the 9.7 and 18μm silicate absorption features or the [SIII] 18.7μm/33.5μm line ratio –, then *without any other optically thin tracer* the result can be biased toward too low values, representing only the properties of a shallow surface, but not the entire dust column. Yet, a robust technique is required which provides the order of extinction and clues to whether the absorbing dust is located in a foreground screen or whether it is mixed with the emitters.

Extinction estimates of ULIRGs have also been derived from longer wavelengths, for example the shape of the spectral energy distribution from the moderately affected FIR to the optically thin sub-mm regimes. These spectra can be fitted by a single modified blackbody with free emissivity β and opacity parameter τ and temperature T. This approach, however, ignores the multitude of dust temperatures suggested from the patchy optical morphology, and the formally derived extinction values up to $A_V \approx 1000$ are questionable. Refinements using several modified blackbodies rely on the choice of the dust emissivity β and the decomposition into the various temperature components (Klaas & Haas et al. 1997, Lisenfeld et al. 2000, Klaas & Haas et al. 2001), hence the opacities cannot unambigously be determined.

4.2 A new method to probe high mid-infrared extinction

In order to determine the total amount of extinction, we here propose a different method, using the flux ratio between the 7.7μm PAH feature and the 850μm continuum emission. While the sub-mm radiation is optically thin and represents the emission from essentially all dust grains, the PAH strength (measured by the peak height of the Polycyclic Aromatic

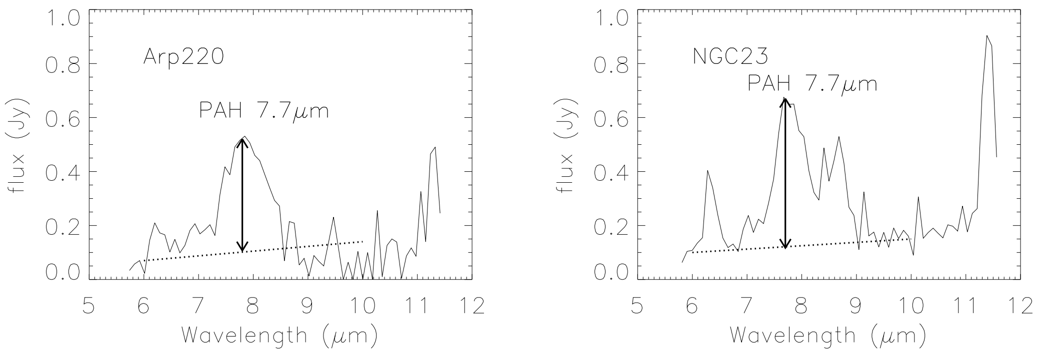

Figure 4.1: Examples of ISOPHOT-S 5-12 μm spectra. *left:* the ULIRG Arp220, *right* the comparison galaxy NGC 23. The dotted line indicates the continuum subtracted for the estimate of the PAH 7.7 μm strength. As can be seen on spectra extending toward longer wavelengths Arp220 has a famous strong silicate 9.7 μm absorption feature (e.g. Dudley 1999), which here is accounted for in the continuum estimate. Note that adopting a lower continuum can increase the determined PAH 7.7 μm strength to at most 20%.

Hydocarbonates at 7.7μm) is sensitive to dust extinction in the MIR.

4.2.1 The data

We apply this tool to 850 and 1300μm observations of a sample of nearby bright ULIRGs (Klaas & Haas et al. 2001) most of which we recently obtained at the JCMT with SCUBA and at the SEST. These data, supplemented by literature data (Rigopoulou et al. 1996, Lisenfeld et al. 2000) and with the 1300μm fluxes interpolated to 850μm, are compared with published PAH spectra of ULIRGs, obtained with ISO (Rigopoulou et al. 1999) and with the UKIRT (Smith et al. 1989, Dudley 1999). This results in a sample of 15 ULIRGs with $L_{FIR} \approx 10^{12} L_{\odot}$ and both the sub-mm and PAH fluxes available.

A comparison sample of 20 "normal galaxies" was constructed as a subset of the SCUBA 850μm local universe galaxy survey (Dunne et al. 2000) containing dusty galaxies with $L_{FIR} < 10^{10} L_{\odot}$. We selected those for which PAH spectra are available in the ISO data archive and for which the ISOPHOT-S aperture (24") contains the entire 850μm flux, as is the case for the ULIRGs.

The synchrotron contribution (clearly below 10%, extrapolated from the cm to mm continua) has been subtracted from the 850μm fluxes.

Fig. 4.1 shows two examples for the PAH spectra. Table 4.1 lists the derived fluxes.

Table 4.1: Measured fluxes in Jy. The MIR continuum around the PAH line was subtracted, also the synchrotron continuum extrapolated from the longer wavelengths was subtracted from the 850 μm flux. The errors are less than 30 %.

ULIRG	PAH 7.7 μm	100 μm	850 μm		Comparison Galaxy	PAH 7.7 μm	100 μm	850 μm
05189-2524	0.220	11.73	0.048		Arp148	0.250	10.99	0.092
UGC 5101	0.186	21.24	0.143		MGC+02-04-025	0.380	9.60	0.039
12112+0305	0.080	9.73	0.030		Mrk331	0.650	20.86	0.132
Mrk231	0.289	30.33	0.045		NGC 23	0.560	14.96	0.144
Mrk273	0.193	24.58	0.077		NGC 695	0.700	13.80	0.136
14348-1447	0.068	7.60	0.016		NGC 1122	0.600	15.15	0.084
15250+3609	0.128	5.80	0.027		NGC 1667	0.400	16.54	0.163
Arp220	0.414	126.7	0.744		NGC 5256	0.350	10.35	0.082
NGC 6240	0.420	28.13	0.137		NGC 5653	0.700	21.86	0.205
17208-0014	0.274	35.66	0.119		NGC 5713	1.000	36.27	0.359
19254-7245	0.084	5.38	0.029		NGC 5962	0.300	20.79	0.317
20100-4156	0.041	5.20	0.019		NGC 6052	0.270	10.18	0.095
22491-1808	0.043	5.06	0.012		NGC 7591	0.400	13.52	0.135
23365+3604	0.086	8.00	0.014		NGC 7592	0.450	10.50	0.108
23389-6139	0.028	4.33	0.009		NGC 7674	0.250	7.91	0.108
					NGC 7679	0.350	10.65	0.093
					UGC 2238	0.600	15.22	0.104
					UGC 2369	0.300	11.10	0.072
					UGC 2982	0.900	17.32	0.176
					UGC 8387	0.500	24.90	0.113

4.2.2 PAH 7.7μm/850μm extinction measurements

Fig. 4.2 (y-axis) shows the PAH 7.7μm/850μm distribution of the ULIRGs and the reference sample. Strikingly, all ULIRGs except Arp220 and UGC 5101 lie in a confined range, which is also the same as for the normal galaxies. This suggests that for both samples the PAH and the sub-mm emission are related, and that no extraordinary excitation conditions are needed. This is supported by the finding that the Galactic disk exhibits PAH emission with a low interstellar radiation field over a large range of different environmental parameters (Mattila et al. 1996). Also Léger & Puget (1989) predicted that PAH formation takes place in molecular clouds. These are typically bright at 850μm, but do not show any high excitation radiation.

UGC 5101 has a high mixed case extinction $A_V \approx 50$ derived from NIR-MIR spectroscopy (Genzel et al. 1998). Dereddening shifts it clearly into the range of the other ULIRGs (Fig. 4.2). Remarkably, UGC 5101 has an optical Seyfert 1.5 type spectrum, thus the high extinction cannot be along the line-of-sight towards the AGN, rather it might be towards extended regions lying off this line.

The PAH 7.7μm/100μm ratio is lower for the ULIRGs than for the reference sample by a factor of about three (x-axis in Fig. 4.2). ULIRGs have warmer dust (30K<T<50K) than normal galaxies (20K<T<30K), and therefore their 100μm flux relative to that at 850μm is higher. Again, along the PAH 7.7μm/100μm distribution Arp220 lies below the other obviously more "typical ULIRGs" which populate a confined range.

We consider three possibilities to explain the exceptional position of Arp220 in Fig. 4.2:

1) A low PAH 7.7μm flux due to a significant destruction of the PAH carriers by a hard UV radiation field is unlikely. Such a field should be present in the other ULIRGs with exposed AGN like Mrk 231 and IRAS 05189-2524, nevertheless they exhibit considerable PAH emission. So far there is no hint for such a field in Arp220. If

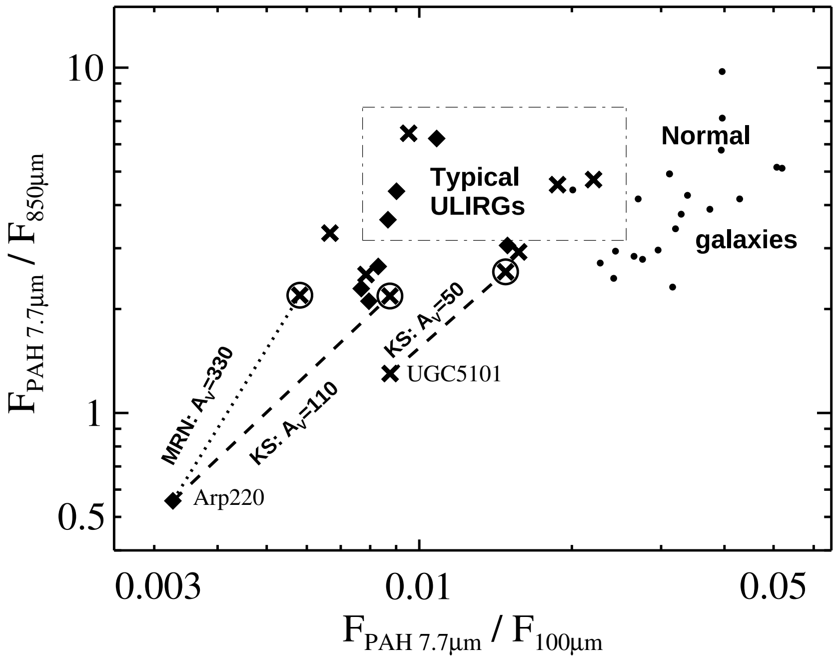

Figure 4.2: Two-colour diagram PAH 7.7μm to 850μm flux versus PAH 7.7μm to 100μm. The symbols are: $\times$ = Seyfert-ULIRGs, ♦ = LINER- and HII/SB-ULIRGs, • = normal galaxies. The errors are less than 30%. The positions of Arp220 and UGC 5101 after dereddening are marked with the encircled crosses. For Arp220 two mixed case extinction curves are considered: interstellar dust (MRN: dotted line), and protostellar dust (KS: dashed line). The dash-dotted box indicates the min-to-max range of the typical ULIRGs after dereddenening with the KS model and A_V values from Genzel et al. (1998). Note that dereddening reduces the PAH 7.7μm/850μm dispersion.

present, it would already point towards a strong but hidden AGN.

2) An excess of 850μm flux due to very cold dust which *also* has to be deficient in PAH emisssion: For example, the extremely quiet galaxy M31 has very cold dust at T$\leq$16K (Haas et al. 1998b) and it could be a low PAH emitter (Cesarsky et al. 1998). But in order to achieve the desired shift in Fig. 4.2, such very cold dust (even without any PAH emission) has to provide about half of the FIR emission and more than three quarters of the sub-mm emission of Arp220. In this case the dust mass would approach (or even exceed) the molecular gas mass derived from the CO luminosities (Downes & Solomon 1998), resulting in a gas-to-dust ratio of about 5, unrealistically low compared with the standard value of about 150. Also, bearing in mind the ultraluminosity of Arp220, a low excitation of the PAH carriers is unlikely.

3) Extinction: since the first two mechanisms do not provide a satisfactory explanation, we conclude that the low PAH 7.7μm/850μm flux ratio of Arp220 is mainly caused by extinction. Further evidence for a significant extinction comes from the deep silicate absorption feature (Dudley 1999). A comparison with UGC 5101 immediately suggests that the MIR extinction is very high.

To summarize, 13 out of 15 ULIRGs as well as 20 comparison galaxies populate the same confined range of the PAH 7.7μm/850μm flux ratio. Their MIR extinction may be moderate (A_V<3-10), so that NIR-MIR spectroscopy can yield proper results. Also, it is not likely that they contain a hidden powerful AGN which has not yet been identified as such by other tracers. Two ULIRGs, however, lie significantly below this range and their offsets are mainly due to high MIR extinction. Thus the new PAH 7.7μm/850μm diagnostics is a promising tool to reveal *high* MIR extinction in ULIRGs.

4.3 Signatures for a hidden quasar in Arp220

The best signatures for an AGN are broad emission lines. Actually in Arp220 a broad Br_α line has been discovered (Depoy et al. 1987). It is shown in Fig. 4.3. The strength of this NIR line, however, was found to be too faint to account for the ultrahigh bolometric (FIR) luminosity (Depoy et al. 1987). In order to do so the extinction towards the region emitting this line would be required to exceed the incredibly high amount of $A_V\approx130$, but at that time other extinction estimates were by far lower ($A_V\approx50$).

An extinction of $A_V \approx 110$ (see Fig. 4.2) is so high that even hard X-rays might be blocked (Compton thick case). Therefore the marginal detection of Arp 220 with ASCA (Iwasawa 1999) or BeppoSax (Risaliti et al. 2000) does not provide evidence against an AGN in this source. Recently CHANDRA observations find evidence for a (possibly luminous) source of hard X-rays elongated east-west which is in fact coincident with both

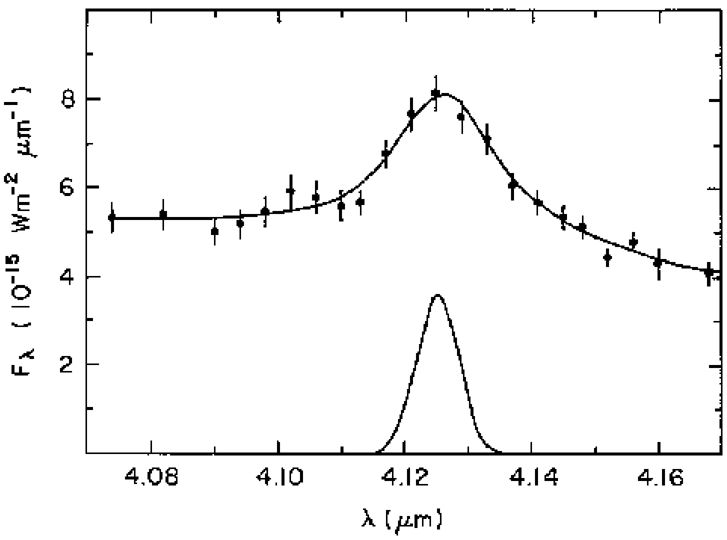

Figure 4.3: Broad Br_α line of Arp220 (FWHM 1300 km/s *top*) and the instrumental profile (*bottom*) (Credit Depoy et al. 1987).

nuclei (Clements et al. 2000). Due to the high extinction the X-rays may not be seen directly, rather via reflection depending on the geometry and a comprehensive picture has still to be worked out (David Clements, private communication).

The supernova remnants resolved using VLBI at 18 cm (Smith et al. 1998), provide evidence for powerful starbursts whose extent is larger than the 100 pc diameter for the MIR emission. Thus, they do not exclude the presence of a deeply hidden AGN.

Similarly, from the upper limits of MIR high excitation lines Sturm et al. (1996) concluded that an AGN – if present – may only be of minor importance for the luminosity budget. While consensus is growing that most of the FIR power comes from starbursts, it is intriguing to explore the consequences from the high MIR extinction assessed with the PAH/sub-mm diagnostics. In fact, a combination of our results with other observations yields increased evidence for a quasar-like powerful MIR emission.

4.3.1 The amount of the PAH 7.7μm extinction

Firstly, we argue in favour of the "mixed case" extinction, in contrast to the simpler case by a dust screen. These cases are illustrated in Fig. 4.4. The extinction factors are $\exp\{\tau_\lambda\}$ and $\tau_\lambda/(1\text{-}\exp\{\text{-}\tau_\lambda\})$ for the screen and the mixed case, respectively, with τ_λ=0.916$\cdot A_\lambda$ (Genzel et al. 1998). For the same observed extinction curves, the amount of extinguishing dust has to be much higher in the mixed case, since the emitters at the shallow surface (front side) are practically not extinguished and those deeply embedded (back side) have to be more heavily obscured. Thus, e.g. for the KS extinction curve explained further

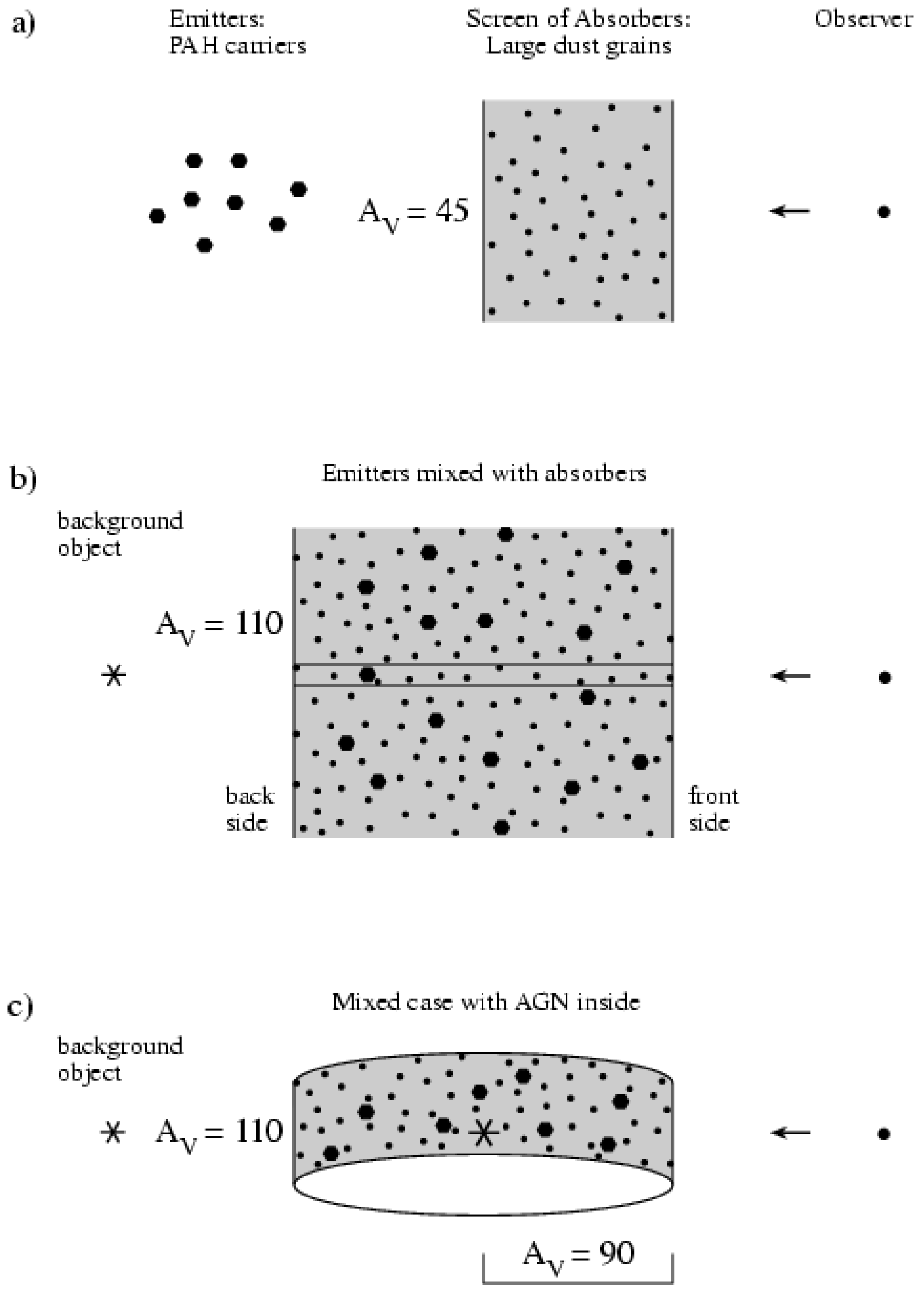

Figure 4.4: Illustration of the "screen" and "mixed" extinction cases. *a) screen case:* all emitters are behind the same "screen" of absorbers viewed from the observer. *b) mixed case:* emitters are "mixed" with the absorbers, and a much higher dust column is required, in order to observe the same reddening as for the screen case. *c) mixed case with AGN inside:* the AGN denoted by an asterisk suffers from screen extinction of half the dust column (resulting in $A_V = 90$, and not $A_V = 55$).

below A_V(KS-screen)≈45 corresponds to A_V(KS-mixed)≈110. Note that for both screen and mixed case extinction the length and orientation of the dereddening vectors in Fig. 4.2 are practically the same, just the nominal value A_V of extinction alters.

The difference in the PAH 7.7μm/100μm distributions between ULIRGs and the normal galaxies can be entirely explained by the higher 100μm/850μm colour temperature of the dust in ULIRGs. ULIRGs have typically a dust temperature T ≈ 30-50 K, while normal galaxies have T ≈ 15-30 K. Hence, the PAH emitters are independent of the warm – presumably starburst heated – dust in ULIRGs. Rather, the similar PAH 7.7μm/850μm distributions for the typical ULIRGs and the normal galaxies suggests that the PAH emitters and the sub-mm emitting dust grains are intimately coupled and actually mixed along the line of sight through the galaxies. Therefore, in the following we will use the mixed case, unless otherwise stated. It may be that the large 850 μm emitting dust grains are more concentrated on the cold cloud cores, while the PAH carriers are more related to the photo dissociation regions (PDRs), i.e. the cloud borders. Nevertheless, on a spatial scale larger than the typical cloud diameters (100 pc) the mixed rather than the screen case is the appropriate description for our purpose.

Now we consider the *minimum additional* mixed case extinction required to shift Arp220 towards the lower border of the PAH 7.7μm/850μm range for the other ULIRGs (Fig. 4.2). This depends on the extinction curves used. A_V≈330, when using the interstellar extinction curve for graphite and silicate grains in our Galaxy, with a grain size distribution cutoff at about 0.3μm (MRN-model: Mathis et al. 1983, Table C1).

In ULIRGs the dust may have properties more like those found in *protostellar* cold dense clouds. Their observed extinction curves have been successfully modelled using flaky grains with a large size cutoff at about 30μm (KS model: Krügel & Siebenmorgen 1994). Using even larger grains (>30μm) would result in a low emissivity exponent of β<1.2, contrary to the observed value of β≈1.6 (Lisenfeld et al. 2000, Klaas & Haas et al. 2001). Furthermore, in contrast to the MRN model, the KS extinction curve has no 5-25μm features in the MIR, consistent with the smooth curve observed toward the Galactic centre (Lutz et al. 1996). Therefore we give the KS model a slightly higher preference. If the *entire* dust in Arp220 has such properties[1], then the extinction required to provide the PAH 7.7μm/850μm offset to the other ULIRGs is at least A_V≈110, which we adopt as a conservative estimate. It is also consistent with the lower limit A_V(mixed)>110, which corresponds to A_V(screen)>45 derived from the [SIII] 18.7μm/33.5μm line ratio (Genzel et al. 1998). Note that from the silicate 9.7 μm absorption feature (see Fig. 4.9 below, Soifer et al. 1999) "only" a moderate A_V(mixed)≈75 is derived. It is pausible to assume that on our spatial scale the tracers *silicates*, *sulfur*, *PAHs*, and *large dust grains* are reasonably mixed along the lines of sight. Then obviously the silicate extinction tool does not probe the entire dust column of Arp220, but only a rather shallow surface. *Our value*

[1] We used: A_V:$A_{7.7\mu m}$:$A_{15\mu m}$:$A_{25\mu m}$:$A_{60\mu m}$:$A_{100\mu m}$:$A_{850\mu m}$ $= 1 : 0.039 : 0.039 : 0.036 : 0.015 : 0.0076 : 0.00035$

A_V(mixed)≈110 is still a lower limit, since it refers to the minimum extinction required to shift Arp220 to the range of the other ULIRGs. Actually a look at Fig. 4.2 shows that also A_V(mixed)≈150-200 is well consistent with the PAH 7.7 μm / 850 μm range (since the x- and y-axes are logarithmic and the A_V vectors simply add up).

4.3.2 The extinction of the MIR continuum

Actually, we are interested the true height of the (central) MIR continuum as possible tracer for an AGN. So far, we have derived the *average* extinction of Arp220 which, however, could vary between *different lines of sight* (towards the galaxy which has an extent in the infrared of less than about 10″, i.e. smaller than our PAH and sub-mm apertures). Thus – before applying some dereddening – one has to show that the average extinction (or even a higher one) applies also for one or both of the nuclei, and that their MIR continuum does not escape relatively unobscured via gaps of low extinction. This task requires high spatial resolution data, and in this section we develop several arguments favouring a highly obscured nuclear MIR continuum.

The central region of Arp220 exhibits a complex geometry on NICMOS images (Fig. 4.5, Scoville et al. 1999) with two nuclei, each intersected by dust lanes, which are coincident with the CO disks (Fig. 4.6, Scoville et al. 1997, Downes & Solomon 1998, and Sakamoto et al. 1999). The actual nuclear centres appear to be entirely hidden behind the dust lanes (Fig. 4.7). On KECK high resolution 3–24.5 μm images (Fig. 4.8) the PAH emission and the 12.5 μm continuum show similar morphologies and only a *moderate variation in the intensity ratios across the images* (Fig. 4.9). This applies also to the 17.9 μm band (which contains both mid-infrared continuum and a silicate absorption feature). If the suspected nuclear MIR continuum would be seen through gaps of low extinction and their extinction is not probed by the PAHs, then one would expect that for each nucleus the MIR continuum is more centrally peaked than the PAH emission. But this is not observed, suggesting in fact that the MIR continuum of both nuclei is highly obscured.

Most of the observed MIR emission in both the continuum and the PAH lines arises from an extremely compact area with a diameter of less than 100 pc centred on the *western* nucleus (Soifer et al. 1999). It contributes to the total flux by 66% at the 12.5 μm continuum and 55% at the 7.7 μm PAH line (see Fig. 4.9).

Further spatial information can be derived from the two bands at 9.7 and 10.3 μm covering the 9.7 μm silicate absorption feature: the *eastern* nucleus clearly belongs to the most obscured regions (Fig. 4.8). Its extinction $A_{9.7\mu m}$ is higher than that of the western nucleus by about a factor of two, resulting in A_V(screen)≈50 corresponding to A_V(mixed)≈125 which may be considered as the *maximum locally determined silicate extinction*. Nevertheless, as seen in the previous section, the average extinction value for Arp220 derived from the silicate feature is by a factor of about 1.5 too low, compared with

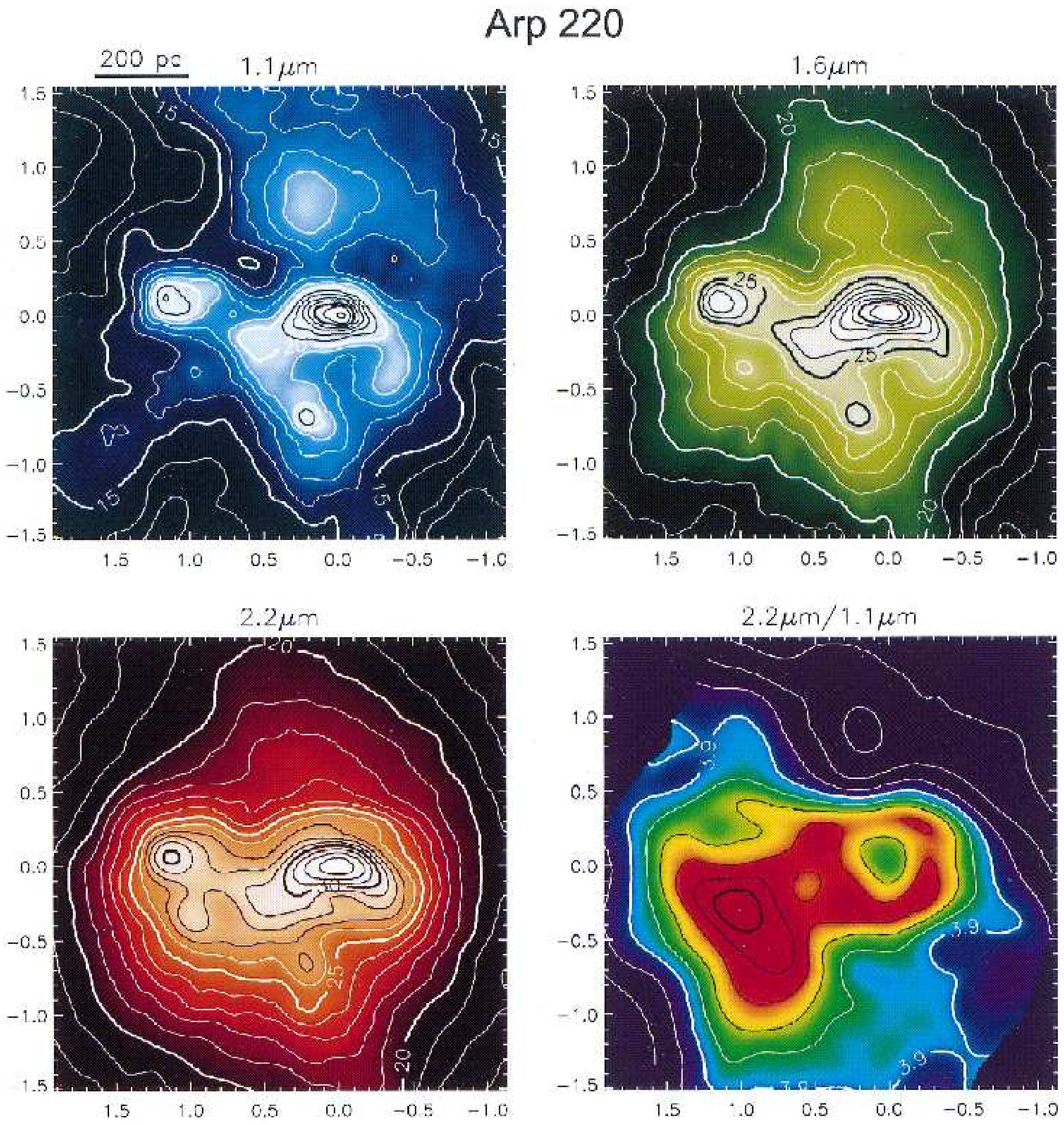

Figure 4.5: NICMOS images of Arp220 (Credit Scoville et al. 1999, the axes are labelled in the unit of arcsec). Note at $2.2\,\mu$m the bipolar eastern emission at (x,y) = (1.1,0.1) and (1.0,-0.4) possibly intersected by a dust lane at (x,y) = (1.0,-0.1) and the half-moon shaped western emission at (x,y) = (0,0). North is up and east towards left.

the PAH/submm diagnostics.

We may speculate that in the eastern nuclear region also the PAH $7.7\,\mu$m / $850\,\mu$m ratio is lowest, indicating highest extinction, too. But currently no sub-mm image of comparable spatial resolution is available, hence we cannot use the PAH/submm diagnostics to

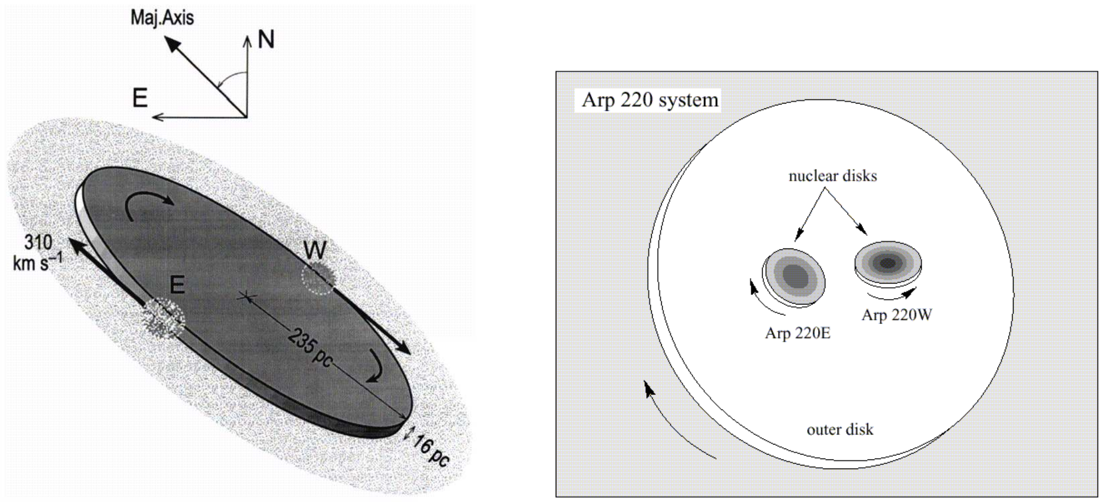

Figure 4.6: Schematic disk scenario derived from the CO observations of Arp220 (Credit Scoville et al. 1997 *left* and Sakamoto et al. 1999 *right*). An outer circumbinary disk contains two small counterrotating disks each associated with a nucleus. All three disks are inclined with respect to the line of sight towards the observer.

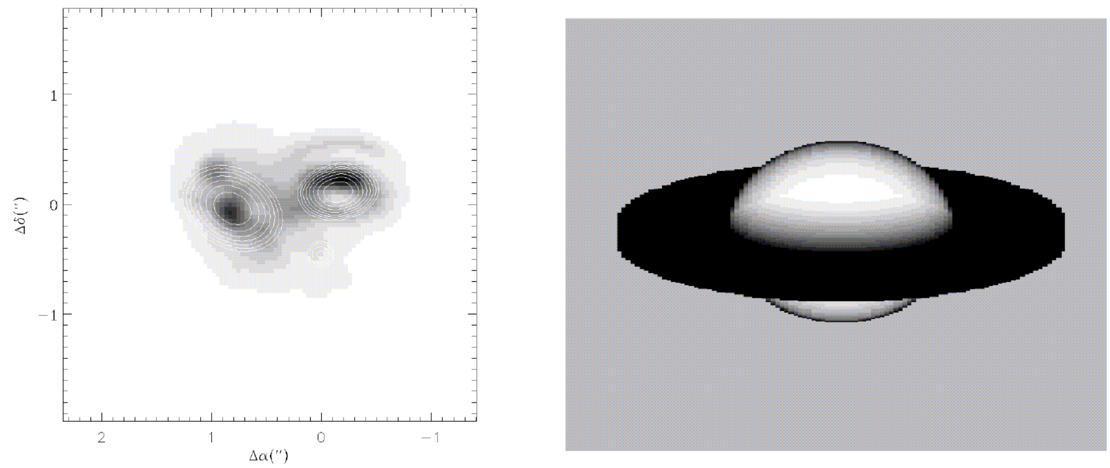

Figure 4.7: *Left:* Radio 6 cm contours overlaid on the NICMOS 2.2 μm image (Credit Scoville et al. 1998). The western NIR peak does not coincide with the radio peak which is the likely position of the actual western nucleus. *Right:* Schematic of the western nuclear region illustrating that the offset between radio and 2.2 μm position and the half moon shape of the 2.2 μm emission could come from the inclined disk (Credit Scoville et al. 1998).

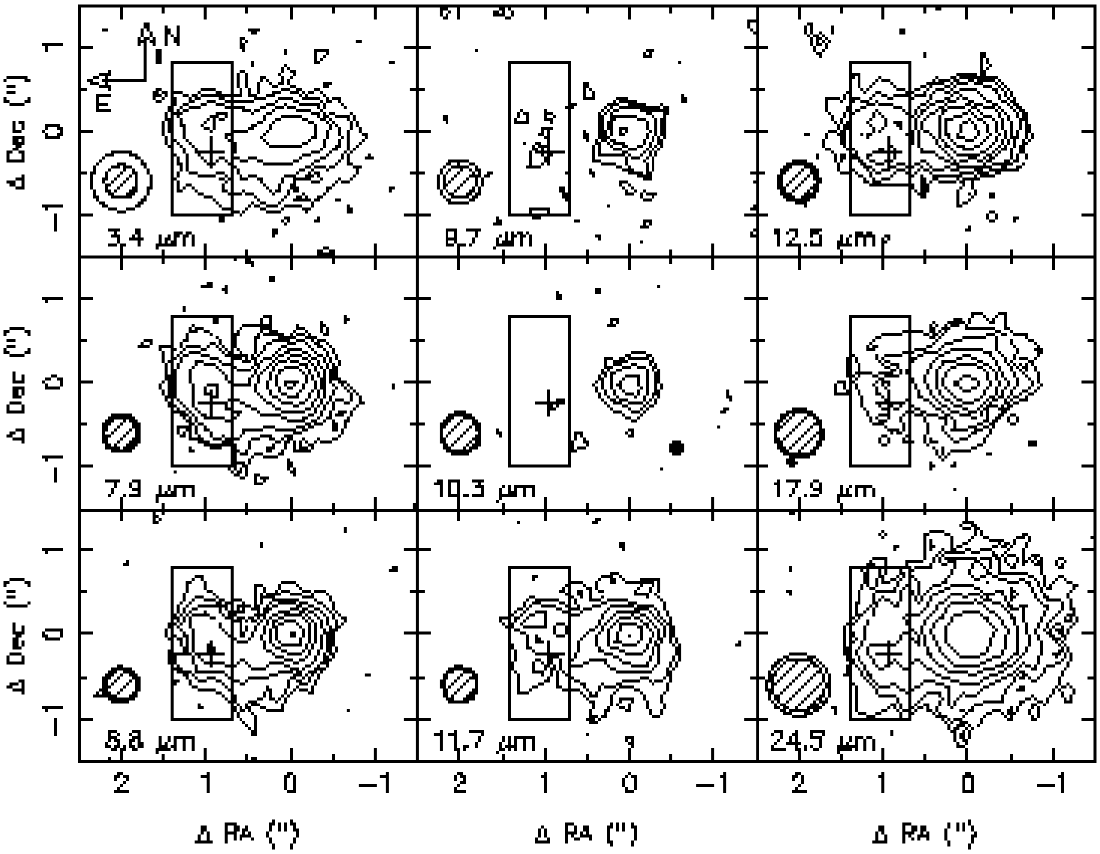

Figure 4.8: Keck contour maps of Arp220 (Credit Soifer et al. 1999). Contours increase by a factor of 1.5. The meaning of the bands are: Bands containing PAH lines are at 3.4, 7.9, 8.8, and 11.7 μm, bands tracing the MIR continuum are at 12.5 and 24.5 μm, and bands with silicate absorption are at 9.7, 10.3. The band at 17.9 μm contains also a silicate absorption feature, but it is not as deep as the one at 9.7 μm. (The plus sign indicates the position of the eastern nucleus as it appears as maximum on the 24.5 μm map, and the rectangle outlines the area used for photometry of the eastern nucleus by Soifer et al.)

determine the spatial variation of the extinction. Therefore we use the spatial information from the silicate band and scale the amount of the extinction so that it fits the average derived from the PAH/submm diagnostics. This results roughly in multiplying the silicate derived extinction A_V(mixed)$\approx$75 by a factor of 1.5.

Adopting $A_V\approx$110 derived from the PAH diagnostics, the extinction towards the nuclei lies at least around A_V(mixed)$\approx$95 (western) and 190 (eastern), respectively. These are conservative estimates and the PAH diagnostics allows also for values of A_V which are about a factor of 1.5–2 higher.

These arguments support the picture that in Arp220 both the regions emitting the PAH

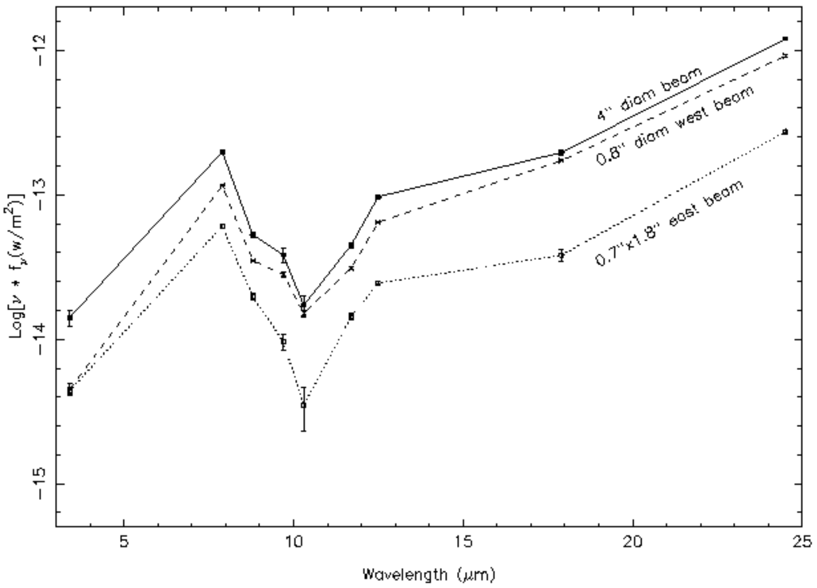

Figure 4.9: Mid-infrared spectra from the Keck contour maps of Arp220 (Credit Soifer et al. 1999).

7.7μm and those emitting the 12.5μm continuum are affected by a high MIR extinction of similar order of A_V(mixed)$\gtrsim$110 (which may further be adopted in order to keep the discussion straight forward). Thus the extinction is so high that it might be difficult to discover a hidden AGN with ordinary tracers.

4.3.3 Dereddening of the MIR continuum

The effects of reddening depend on the geometry of the absorbing/reemitting dust and we consider here the extreme cases "ideal sphere" and "axis-symmetric geometry".

If the dust were distributed in an *ideal sphere*, then the absorbed MIR continuum could only escape via reemission at longer wavelengths. In this case "dereddening" will not increase the total luminosity, but only the L_{MIR}/L_{FIR} ratio via a shift of L_{FIR} towards L_{MIR}. But this case can be rejected as follows:

On a large kpc scale, sensitive H_α, X-ray and HI maps (Heckman et al. 1987, Heckman et al. 1996, Hibbard et al. 2000) reveal a bipolar cavity –inclined with respect to our line of sight – created by strong supernova winds. On a small 50 pc scale, the presence of CO disks also indicates a *non-spherical axis-symmetric geometry* tilted about 45^o with respect to our line of sight (Scoville et al. 1997, Downes & Solomon 1998 and Sakamoto et al. 1999). Therefore, a significant portion of the MIR continuum might escape along the polar directions, but along the line of sight a reduced portion of the luminosity is seen. In

Table 4.2: Observed and dereddened luminosities of Arp220.

	deredd. factor	L_{MIR} $10^{11}L_{\odot}$	deredd. factor	L_{FIR} $10^{11}L_{\odot}$	L_{MIR}/ L_{FIR}
observed	1.0	2.1	1.0	9.0	0.23
MRN:A_V=330	10 (4...20)	≈ 21.0	3.2	28.8	0.72
KS: A_V=110	4.0	8.4	1.7 (1.3 ... 2.0)	15.3	0.54
KS: $A_V$screen=90*	20.0	42.0	"	"	2.75

* screen case on central MIR continuum, while the mixed case extinction probably still applies to the FIR emission

order to derive the true MIR luminosity, dereddening has to be applied. It will actually increase L_{MIR}, and to a less extent also L_{FIR}[2].

If (along the line of sight) the emitters of the MIR continuum are mixed with the absorbing dust, then the same A_V as derived from the PAH diagnostics can be used for dereddening. The results are listed in Tab. 4.2 (rows 2 and 3) and shown in Fig. 4.10. Dereddening with the MRN model shifts Arp220 from the cool ULIRGs to the warm ones, each of which houses a strong AGN. With the KS model such a shift is present, but less pronounced. Nevertheless, in both cases L_{MIR} reaches high quasar-like values ($\approx 10^{12}L_{\odot}$).

The compactness of the MIR emitting region and the presence of the dusty CO disks suggests, that the MIR continuum originates more in the centre, which is surrounded by the absorbing material. Such a situation is typically seen in Seyfert 2s (Clavel et al. 2000). Remember that the column density of the absorbing material is inferred via mixed case. As illustrated in Fig. 4.4 c, however, half of the dust column according to A_V(KS mixed)≈110 will then work effectively on the central MIR continuum as *screen* absorber with an amount of A_V(KS screen)≈90. This places Arp220 clearly in the L_{MIR}/L_{FIR} range of quasars (Tab. 4.2, row 4). With the MRN extinction curve A_V(MRN mixed)≈330 or a less conservative A_V(KS mixed)≈150 the screen dereddening of the centre becomes even more extreme. Note that these values are by far sufficient compared with A_V(screen)≈130 which was required by Depoy et al. (1987) in order to bring the observed low strength of the broad Br_{α} line into a range consistent with the bolometric (FIR) luminosity.

[2]Because the MRN extinction curve shows features between 5 and 25μm, we used luminosities. $L_{10-40\mu m}$ comprises some kind of stable average over these features; our results are basically the same as when using e.g. the 12.8 or 15μm fluxes. The luminosities of the sample are derived from ISOPHOT and sub-mm photometry (Klaas & Haas et al. 2001); we use H_o=75km/s/Mpc.

4.3.4 The luminosity density: favouring a quasar

So far, we arrived at a quasar-like MIR luminosity, and it remains to be shown that this cannot be provided by starbursts.

With conservative dereddening of L_{MIR} by a factor of 4 (Tab. 4.2, KS:$A_V \approx 110$), the MIR luminosity density of the *western nucleus* reaches $7.3 \cdot 10^7 L_\odot/pc^2$ ($L_{MIR} \approx 0.56 \cdot 10^{12} L_\odot$, $r \approx 50pc$), about a factor of 1000 higher than in the prototype nearby starburst galaxy M82 ($L_{MIR} \approx 9 \cdot 10^9 L_\odot$, $r \approx 200pc$). Since the dust (and the gas) is more dissipative than the stars, is tends to be distributed in a more compact area than the stars. Bearing this in mind, it is difficult to imagine, how starbursts alone can create such a high luminosity density, and *simultaneously* how the dust hides them entirely.

Therefore, a more natural explanation would be that – in addition to the prominent starbursts mainly responsible for the FIR luminosity – one (or both) of the nuclei of Arp220 contains a powerful AGN providing the quasar-like MIR luminosity which is hidden to us.

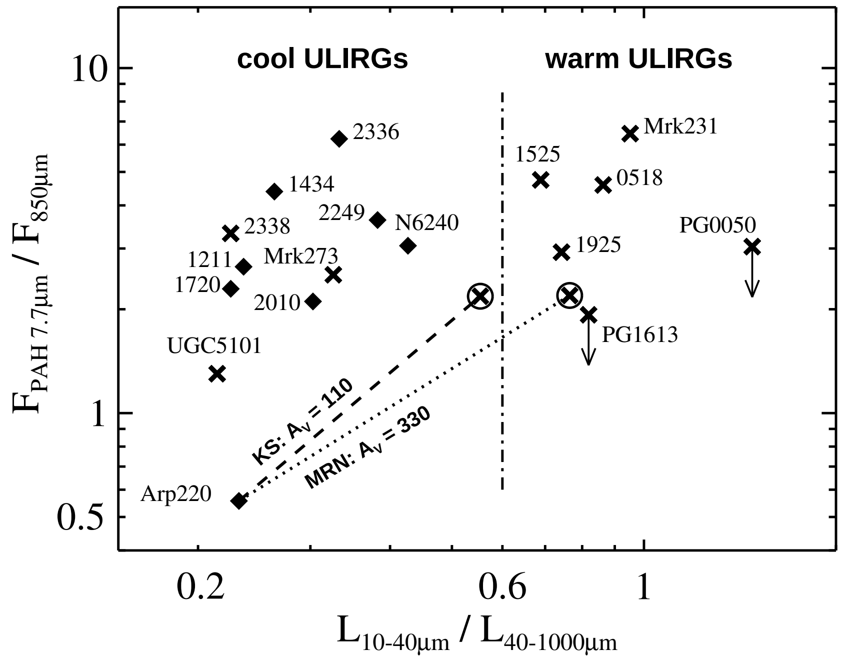

Figure 4.10: Two "colour" diagram PAH 7.7μm to 850μm flux versus L_{MIR}/L_{FIR} (= $L_{10-40\mu m}/L_{40-1000\mu m}$). Symbols as in Fig. 4.2. In addition, two PG quasars, where PAH spectra are available, are plotted. The dereddened positions of Arp220 correspond to the KS and MRN cases listed in Tab. 4.2. The vertical dash-dotted line marks the division between warm and cool ULIRGs according to $F_{25\mu m}/F_{60\mu m} \approx 0.2$.

To summarize, Arp220 shows an extraordinarily high – presumably mixed case – extinction, which also works on the MIR continuum of the nuclear regions. The presence of tilted non-spherical geometry justifies that after dereddening the true MIR luminosity reaches quasar-like values. The amount of extinction is consistent with reducing a quasar-like broad Br_α line to the low strength observed. Moreover, the MIR luminosity density of the western nucleus exceeds that of known circumnuclear starbursts, thus increasing the evidence for a hidden quasar in Arp220. The eastern nucleus is even more extinguished, so that the east-west elongated X-ray emission which coincides with both nuclei suggests that also the eastern nucleus contains a hidden quasar. Since both nuclei have not yet merged the quasar(s) might be very *young*. In conclusion, the new infrared and sub-mm investigations provide crucial clues to reveal even extremely hidden quasars.

Chapter 5

Conclusions

Sensitive infrared to mm observations have gained new insights on dust and synchrotron emission in quasars and on their aspect-dependent relation to radio galaxies and some ultraluminous infrared galaxies. The cornerstones are:

1) Most – if not all – (optically selected) quasars are surrounded by considerable amounts of dust, the heating of which requires *both* AGN and starbursts. The strength of AGN and starburst activities is closely correlated. The dust might be organised in a disk-torus configuration, since otherwise the nuclear regions would be extinguished. As a consequence, edge-on quasars may well exist, but they will never be identified as such via ordinary criteria.

2) Radio galaxies and steep spectrum radio-loud quasars exhibit similar dust properties, thus providing the first successful evidence in the infrared favouring their aspect-angle unification. Furthermore, it seems that the infrared emission is a better tracer for the AGN strength than the radio lobe luminosity. Hence, the dust-to-lobe luminosity ratio may be used to explore the influence of environment and evolution.

3) The PAH $7.7\,\mu$m / $850\,\mu$m ratio is introduced as a new extinction tool. This tool actually allows extremely high MIR extinction in some ULIRGs to be measured. In one example, Arp220, the comparison of the high extinction with other observables actually increases the evidence for a hidden quasar in this prototype cool ULIRG.

The results obtained with these first small samples stress the value of infrared observations of quasars. Corroboration of these results by larger more sensitive data bases is highly welcome.

The next steps would be to investigate the evolution of radio-quiet as well as radio-loud quasars. Crucial constraints from ISO and natural lines to follow are for example:

- The dust luminosity of quasars spans three orders of magnitude from 10^{11} to 10^{14} $L_\odot$. It has to be clarified how far this large dispersion is simply the consequence of large and small galaxies, or whether it is the signature of evolution from dust-rich young quasars towards more evolved ones with less dust.

- The mid-to-far-IR luminosity ratio and the temperature of the coldest dust component appears higher in quasars at high luminosity (or high redshift).

- The AGN-starburst connection: The starburst luminosity seems to be of similar order to the AGN luminosity. Nevertheless, one may suggest that the relative AGN luminosity continues to increase with quasar evolution (However, when the feeding of the AGN declines in a 'very old' quasar, then the contribution of the host galaxy again becomes more important).

- In a sequence like *ultraluminous merger of two dust rich galaxies – quasar – "naked" elliptical galaxy* the dust inevitably has to disappear at some stage between the quasar and the elliptical-galaxy period,. Therefore sensitive infrared SEDs of elliptical galaxies could provide further clues to evolution: the younger ellipticals (or those with a recent merger/quasar event) may also be those which have more dust remnants. So far, no infrared results on the various elliptical samples observed with ISO have been published.

  In addition to infrared and sub-mm data, independent criteria for the evolutionary stages have to be found, for example on high resolution optical images the degree of disturbance of the morphology of the host galaxy could serve as such an indicator, but suitable imaging surveys are still needed.

- As regards unification, the ISO observations provided the first steps in the infrared, favouring radio-galaxies as edge-on radio-loud quasars. Nevertheless, further refined SEDs are clearly desirable.

  The radio lobes are subject to a strong and – on cosmic time scales – fast evolution and depend on the circumgalactic environment. Therefore it would be interesting to compare the infrared properties with radio and other observables as well, for example the [OII] lines. (For our ISO sample no suitable overlap with published [OII] line samples has been found).

- The physical reason for the intimate connection between the PAH 7.7 μm and the 850 μm sub-mm emission in ULIRGs and normal galaxies still has to be explored. Further investigations on galactic regions as well as on other – spatially resolved – galaxy samples should be able to refine the new extinction diagnostics. Also, more sensitive mid-infrared spectroscopy should be able to clarify the presence of PAH emission in quasars.

These tasks required particularly sensitive observations. The next infrared spacecraft missions in preparation are:

- SIRTF (85 cm telescope, 3-170 μm, observatory, launch in 2002),
- ASTRO-F (70 cm telescope, 10-170 μm, all sky survey, launch in 2004) and
- FIRST/HERSCHEL (3.5 m telescope, *Far-Infra-Red and Submillimetre Telescope*, 60-600 μm, observatory, launch in 2007).
- NGST (8 m telescope, *Next Generation Space Telescope*, optical and mid-infrared instruments on board, launch in 2009)

Larger data bases from the ISO archive and from the upcoming infrared satellites SIRTF and ASTRO-F during the next few years will support the findings from the first samples with ISO. However, for most of the topics mentioned above – in particular those related to cosmic evolution – a clarification will have to wait until the next generation of large space telescopes like FIRST/HERSCHEL and the NGST.

Chapter 6

Appendix: Advanced ISOPHOT Data Analysis

This thesis is based on a new observing technology and new data products. Since the sources are faint near the detection limit, the results largely depend on an optimised and solid data analysis. In principle, the data reduction was carried out with the ISOPHOT Interactive Analysis software package (PIA[1]) enhanced by specially designed algorithms.

The results obtained with the standard algorithms implemented in PIA often showed relatively large errors due to random outliers. These prevented a formal 3-sigma detection, though the visual inspection of, for example, a chopped signal series left no doubt in the source detection. (Often the eye is still the best analyzer.) Statistically a sigma-clipping could help to remove the outliers, but a general "blind" application of sigma-clipping sometimes results in unrealistically small errors – recognisable in particular in case of a non-detection, e.g. when a 3–sigma upper limit at 60 μm lies far below a clear detection at 25 and 100 μm. Also, for the raster maps the creation of the maps from different detector pixels introduced noise due to drift and flatfield differences, which prevented optimal source detections.

Therefore – quasi as prototypes – we developed advanced reduction techniques. Since PIA will not be upgraded further (due to man power shortage), the two most important techniques for an optimised source detection are briefly described here.

It should be stressed that due to the high sensitivity promised for ISOPHOT on the basis of laboratory experiments, the observing times spent on each target were rather short (360 s down to only 16 s, depending on the expected source brightness and contrast above the galactic cirrus); the impact of cosmic particles, however, was much higher than expected and damaged large portions of the measurement time series. Thus not only must

[1]PIA is a joint development by the ESA Astrophysics Division and the ISOPHOT consortium led by the MPI für Astronomie, Heidelberg. Here we used the versions V7.x, V8.x and V9.x as available during the years 1997, 1998 and 1999.

the data reduction strategy definitely be good, but also of importance is a strategy to check the reliability of the results with respect to astronomical application. Therefore the second section of this chapter additionally contains a consideration of the main parameters which influence the detection rates and could introduce a bias. Moreover, a look at the figures gives a valuable impression of the data quality.

6.1 Optimised source detection

6.1.1 Fourier analysis of chopped data

For the chopped measurements we applied a Fourier analysis as illustrated in Fig. 6.1, for PG 1206+459 at 60 μm which is too faint to have been detected by IRAS: Before Fourier transformation, the measured sequence was mirrored (around the vertical dotted line). This is important in case of a long term drift as indicated by the dashed line. This yields a continuous periodic sequence by removing the jump, and thus reduces sidelobe noise in the Fourier power spectrum. In Fourier space the source signal shows up at the chopper frequency ($\nu = 15$ in Fig. 6.1), while the noise of the chopped sequence forms some kind of baseline distributed over all frequencies; the residual effect of the long term drift shows up at the low frequencies in the baseline ($\nu = 2$, 3, and 5 in Fig. 6.1). Since the chopper frequency is the highest frequency occuring in the (true) Fourier spectrum, in this plot the Fourier spectrum is also mirrored around the chopper frequency for the purpose of a better visual impression of the source signal sitting above the baseline and its scatter. The source signal (asterisk) is extracted after subtraction of a suitable baseline fitted by a

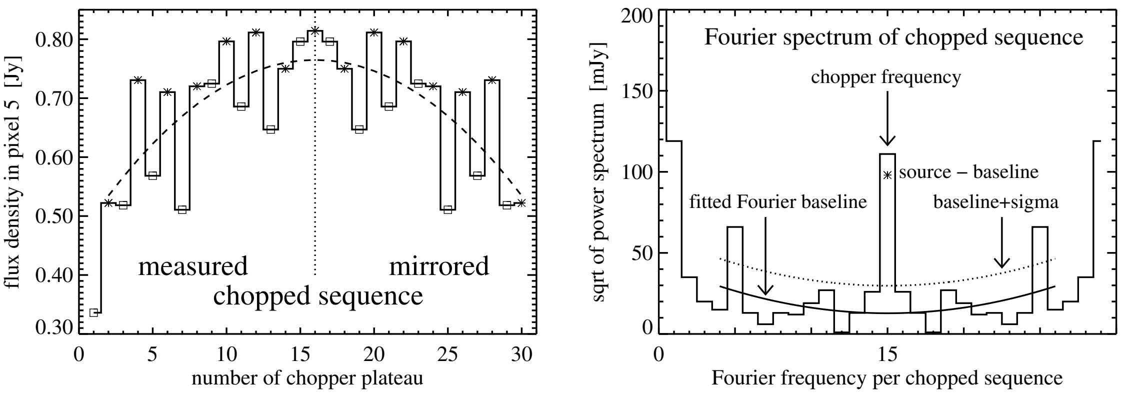

Figure 6.1: Example of a chopped sequence (□ = off-source, ∗ = on-source) and its Fourier spectrum. Only the central pixel (no. 5) of the 3×3 pixel detector array is used; the border pixels contain only about 5% of the source flux, therefore their inclusion effectively only increases the noise (due to cirrus) and worsens the detection rate.

parabola, and sigma is determined from the scatter of the baseline around this parabola. Note that sigma in the Fourier space ($\approx$ 15 mJy) is considerably smaller than in the chopped sequence ($\approx$ 50 mJy). (The final source flux is derived by applying corrections for point spread function and chopper frequency dependent signal loss due to detector transients – as in standard PIA.)

The Fourier analysis is quite robust against single outlier chopper plateau signals and the effect of long term detector drift. Its main advantage is a consistent noise estimate which also accounts for the number of chopper plateaux: Various measurement series (taken from the ISO archive) with the same total on-source integration time, but with one series having *many short* chopper plateaux and another having *few long* chopper plateaux, were compared. A standard PIA data reduction yielded different sigma values (those series with short chopper plateaux appeared noisier, since the number of chopper plateaux was not accounted for), but the Fourier analysis gave similar sigma values for all series. Empirically we found that sigma$_{\mathrm{Fourier}}$ is proportional to sigma$_{\mathrm{PIA}}$ $* \, n^{-0.1}$ with $n =$ number of chopper plateaux. Thus our sigma$_{\mathrm{Fourier}}$ still has the meaning of the *rms* and is not the *error of the mean* which would be proportional to $n^{-0.5}$, i.e. much smaller.

6.1.2 Time series analysis of raster maps

During the actual execution of the first – chopped – measurements it turned out that the occurrence of high energy particle glitches and the presence of cirrus structure severely lim-

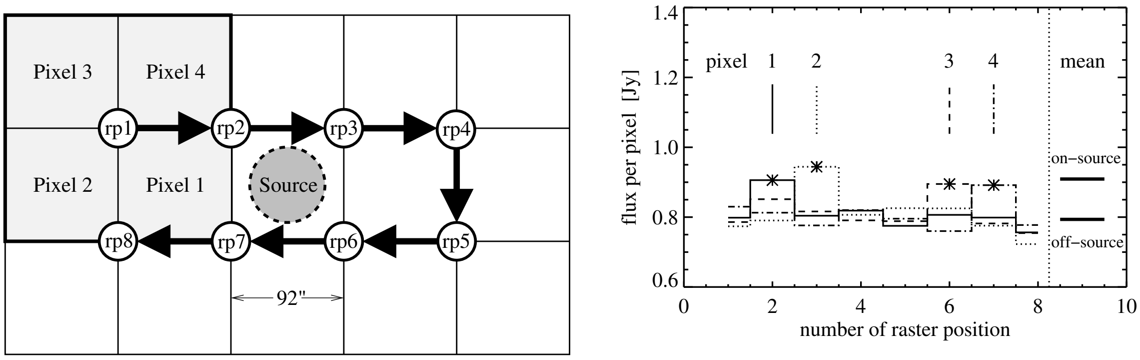

Figure 6.2: Scheme of a raster map with the C200 detector and its time series analysis.
left: Small 4×2 raster map with the 2×2 pixel C200 detector array (shadowed), resulting in a map with a size of 5×3 pixels. During the raster map each detector pixel is centered on the source exactly once.
right: Signal time series for each pixel shown by a different linestyle. The asterisks and vertical lines indicate those raster points on which the pixel j is expected to hit the source. The mean on– and off–source signals are also shown on the right hand side.

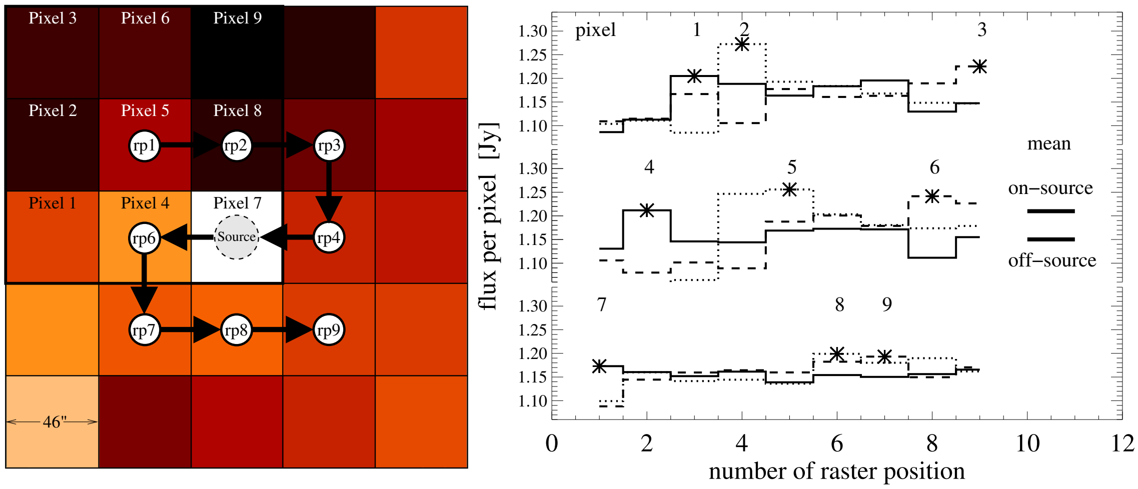

Figure 6.3: Raster map with the C100 detector and its analysis. The example shown is the faintest one of our quasar detections (PG 0044+030), where we co-added the 60 and 100 μm time series (resulting in a broad 80 μm measurement).
left: Grey level map with overlay of the raster scheme. The small 3×3 raster map with the 3×3 pixel C100 detector array (shadowed) results in a map with a size of 5×5 pixels. During the raster map each detector pixel is centered on the source exactly once. The grey levels from black to white give the different flux intensities with the highest flux at the source position.
right: The signal time series of a 3×3 raster map with the 3×3 pixels C100 array, each pixel in a column having a different linestyle. The asterisks indicate those raster points on which the pixel j is expected to hit the source. For all 9 detector pixels a positive source signal is derived above the signals from the neighbouring background raster points. Nevertheless the noise is quite high, mainly caused by the long term drift (e.g. pixel 7 hits the source at the first raster point and yields a too small source flux) and residuals from glitches (e.g. the on–source position of pixel 2 or the lefthand background position of pixel 5). The mean of all on– and off–source signals are also shown on the right hand side.

ited the sensitivity, and the observations were redesigned using the more time consuming redundant mapping mode.

For the small raster maps we did not extract the source flux from the final maps. Instead, we analysed the signal time series while each detector pixel crossed the source. This is illustrated for the relatively bright source PG 1206+459 at 170 μm observed with the C200 detector (Fig. 6.2) and for our faintest one PG 0044+030 with the C100 detector (Fig. 6.3). This technique allows immediate recognition of bad or outlying signals. Furthermore, a long term detector drift could increase the scatter in the background values of a map, while for the time series of each detector pixel the background can be estimated more accurately from the raster positions located immediately before and after the source was hit. (Since the Airy disk is larger than the size of one pixel, in principle some source flux is detected by the pixels on the adjacent raster positions, i.e. just those from which the background was estimated. But – as we ascertained from the beam profiles – this offset is clearly less than 5% of the source flux, hence negligible within the other errors.) The final source signal is then derived from the mean of the signals for the j detector pixels, whereby outliers are clipped. The final source flux is derived applying corrections for point spread function.

6.2 Influences on the detection statistics

6.2.1 Galactic cirrus

Fig. 6.4 illustrates for the PG quasar sample that the cirrus ("background brightness") mainly determines whether detections or upper limits can be achieved, and that the upper limits are not biased at high redshift.

We accepted as detections only those cases where the source was clearly visible above the cirrus noise. Fig. 6.3 shows the faintest of our detections. Furthermore, if our derived source fluxes were dominated by cirrus noise contributions, we would expect spectral energy distributions with a 17–20 K dust temperature similar to that of the galactic cirrus. But this is not the case – the dust temperatures of our quasars are much higher ($T \gtrsim 30$ K).

For the comparative study of the unification of the 3CR radio galaxies and quasars it is essential that both samples are observed with the same background limitations. Fig. 6.5 shows source flux versus background brightness. Galaxies and quasars are equally well distributed over the range of background brightness. At low background (less than 8.5 MJy/sr) all five sources are detected, two galaxies and three quasars (one being 3C380 with the lowest flux which is seen only on the raster map). At higher background non-detections are frequent. Remarkably, some chopped data (3C 20, 3C 47, 3C 368) yielded rather faint flux detections at a background brightness comparable to that below 3C 138, while for this source only upper limits could be achieved on the raster maps. Nevertheless, these detections seem reliable since their 60 to 100 μm flux ratio implies a dust temperature $T > 30$ K, well above typical cirrus values of $T \approx 15$ K.

The fact that a couple of upper limits are at quite high flux levels, could be caused by cosmic ray hits (Sect. 6.2.3).

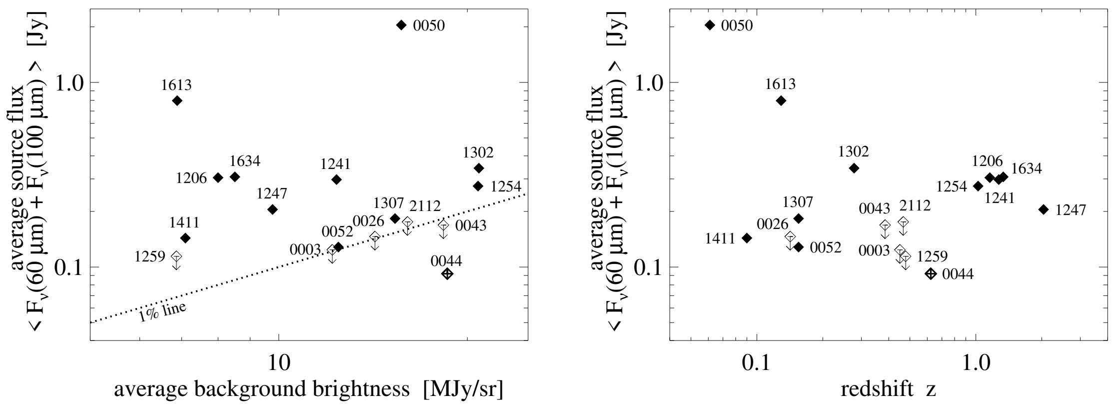

Figure 6.4: Source flux versus background brightness *(left)* and redshift *(right)*, respectively, for the PG sample. The source flux and background brightness were averaged from the 60 and 100 μm data, as for the last column in Table 2.1. The symbols are: ♦ = detections, ◇ with arrow = 3–sigma upper limits. The upper limits lie around the dotted line, above which the sources are brighter than 1% of the background. PG 1259+593 and PG 2112+059 were only observed with the less sensitive chopped mode. The diamond with plus represents the exceptional case of PG 0044+030, for which the 60 and 100 μm raster maps have been co-added (Fig. 6.3).

6.2.2 Mixture of observing modes with different sensitivities

During the ISO mission the first observations were performed in the less sensitive chopping mode and the later ones by raster maps with higher sensitivity. Again, for the comparative study of the unification of the 3CR radio galaxies and quasars it is essential that both samples are observed with the same instrumental sensitivity. Fig. 6.5 illustrates that the two cases of raster maps do not introduce a bias in favour of the unification: For example, at 60 and 100 μm the only two cases with maps are both on QSOs, but one of them (3C138) remains undetected, while one (3C380) which was not detected in the chopped mode, is now detected using the sensitive raster map. Although this biases the statistics slightly in favour of quasars, 3C380 is by chance a unique case, where the FIR emission is clearly dominated by non-thermal synchrotron radiation.

6.2.3 Cosmic particle glitch rates

Detections may be severely hampered by cosmic particles hitting the detectors.

Fig. 6.6 shows the chopped sequence of 3C 9 and 3C 298, both at the same background level in Fig. 6.5. While the sequence of 3C 298 immediately shows the on–off oscillation pattern typical for a clear source detection, that of 3C 9 is irregular and disturbed. Obviously, increased cosmic rates have limited the detections. (This is in fact the case, as

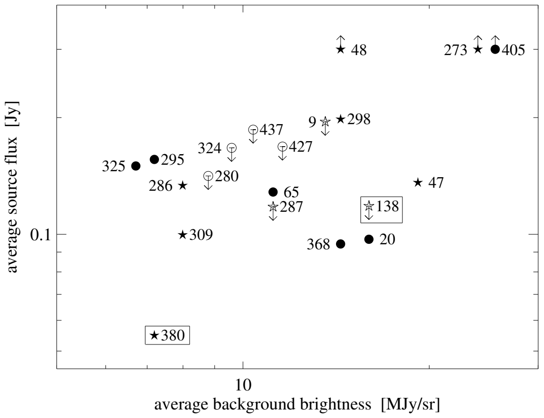

Figure 6.5: Illustration of the detection balance for the 3CR radio galaxy/quasar sample: The sensitivities of our observations are not biased with respect to either quasars or radio galaxies. Far-infrared source flux (averaged 60 and 100 μm values) versus background brightness. The symbols are: $\star$ = quasars, $\bullet$ = galaxies, filled = detections, open symbols with arrow = 3–sigma upper limits. All data are observed in chopped mode, except the two cases 3C380 and 3C138 marked with a surrounding box for which more sensitive raster maps were obtained. The three sources with fluxes well above 300 mJy are indicated by upwardly pointing arrows.

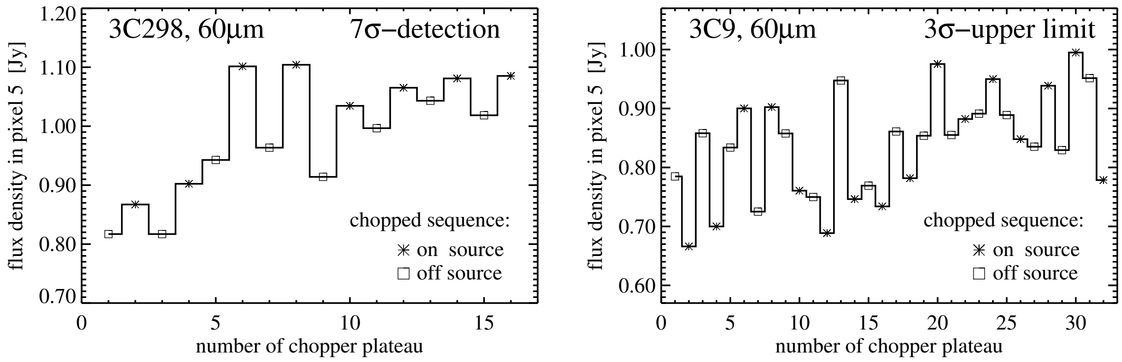

Figure 6.6: Influence of glitch rates on the source detection in chopped data sequences: Chopped sequence of 3C9 and 3C298, both at similar average background levels, and of the same duration of 128 s, and with a long term detector drift. While the sequence of 3C298 clearly shows the on–off–source oscillation pattern typical for a clear detection with some remaining glitches at the chopper plateaux 6 and 8, that of 3C9 is irregular and disturbed. Increased cosmic rates near the van Allen belt have limited the detections at 60/100 μm: we found in the raw data stream 134/158 glitches for 3C9, but only 32/17 for 3C298.

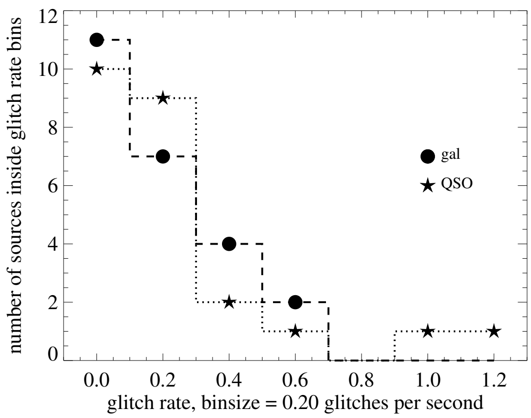

Figure 6.7: Histogram of the glitch rates among the 60 and 100 μm observations of the 3CR quasars ($\star$) and radio galaxies ($\bullet$). Due to some repeated measurements the total number for quasars and for galaxies sums up to 24 instead of 20.

we found when investigationg in detail the raw data level in which the glitches can be identified.) Near the van Allen belt the cosmic rates are higher, but overall we found no systematic trend in our data: some observations in the middle of the orbit (far from the van Allen belt) were severely disturbed by cosmics, while other observations close to the van Allen belt yielded good detections.

We checked that the orbit positions of our galaxy and quasar observations were randomly distributed, and the glitch rates show no significant bias with respect to either galaxies or quasars (Fig. 6.7). Again, among the 3CR sample we cannot find any difference with respect to either galaxies or quasars.

Bibliography

Antonucci R.R.J., Miller J.S., 1985, ApJ 297, 621
Spectropolarimetry and the nature of NGC 1068

Baade W., Minkowski R., 1954, ApJ 119, 206
Identification of the Radio Sources in Cassiopeia, Cygnus A, and Puppis A

Bahcall J.N., Kirhakos S., Schneider D.P., 1996, ApJ 457, 557
The Apparently Normal Galaxy Hosts for Two Luminous Quasars

Bahcall J.N.,Kirhakos S., Saxe D.H., Schneider D.P., 1997, ApJ 479, 642
Hubble Space Telescope Images of a Sample of 20 Nearby Luminous Quasars

Baker J.C., 1997, MNRAS 286, 23
Origin of the viewing-angle dependence of the optical continuum emission in quasars

Barthel P.D., 1989, ApJ 336, 606
Is every quasar beamed?

Barthel P.D., Arnaud K.A., 1996, MNRAS 283, L45
Anomalous radio-loudless of Cygnus A and other powerful radio galaxies

Barvainis R., 1990, ApJ 353, 419
On the optical-to-far-infrared spectral energy distributions of radio-quiet quasars

Beichman C.A., Soifer B.T., Helou G., Chester T.J., Neugebauer G., Gillett F.C., Low F.J., 1986, ApJ 308, L1
Discovery of an infrared-loud quasar

Bennett A.S., 1962a, MmRAS 68, 163
The revised 3C catalogue of radio sources

Bennett A.S., 1962b, MNRAS 125, 75
The preparation of the revised 3C catalogue of radio sources

Bothun G.D., Mould J., Heckman T., Balick B., Schommer R.A., Kristian J., 1982, AJ 87, 1621
0351+026 - A QSO spawned by interacting galaxies

Bregman J.N., 1990, A&A Rev. 2, 125
Continuum radiation from active galactic nuclei

Cesarsky D., Lequeux J., Pagani L., Ryter C., Loinard L., Sauvage M., 1998, A&A 337, L35
The strange mid-infrared spectrum of M31: ISOCAM observations

Chambers K.C., Miley G.K., van Breugel W. 1987, Nature 329, 604
Alignment of radio and optical orientations in high-redshift radio galaxies

Chini R., Kreysa E., Biermann P.L., 1989a, A&A 219, 87
The nature of radio-quiet quasars

Chini R., Biermann P.L., Kreysa E., Gemünd H.-P., 1989b, A&A 221, L3
870 and 1300 μm observations of radio quasars

Chini R., Haas M., Klaas U., Kreysa, E., Lemke D., Meisenheimer K., Müller S.A.H., Stickel M., 1999, in *ISO Surveys of a Dusty Universe* eds. Lemke D., Stickel M., Wilke K., Lecture Notes in Physics 548, Springer p. 169
The ISOPHOT View of Quasars and Radiogalaxies

Clements D., McDowell J, Shaked S., Baker A.C., Borne K, Colina L., Lamb S., Mundell C., 2000, AAS 197.12504 **Chandra observations of Arp220: The nuclear source**

Depoy D.L., Becklin E.E., Geballe T.R., 1987, ApJ 316, L63
Discovery of broad Brackett-alpha emission in ARP 220

Disney M.J., Boyce P.J., Blades J.C., Boksenberg A., Cane P., Deharveng J.M., Macchetto F., Mackay C.D., Sparks W.B., Phillipps S., 1995, Nature 376, L150
Interacting Elliptical Galaxies as Hosts of Intermediate Redshift Quasars

Disney M.J., 1998, Scientific American 278, 52
A new look at quasars

Downes D., Solomon P.M., 1998, ApJ 507, 615
Rotating Nuclear Rings and Extreme Starbursts in Ultraluminous Galaxies

Dudley C.C., 1999, MNRAS 307, 553
New 8-13 μm spectroscopy of luminous and ultraluminous infrared galaxies

Dunlop J.S., Taylor G.L., Hughes D.H., Robson E.I. 1993, MNRAS 264, 455
Infrared Imaging of the Host Galaxies of Radio-Loud and Radio-Quiet Quasars

Dunne L., Eales St., Edmunds M., Ivison R., Alexander P., Clements D.L., 2000, MNRAS 315, 115
The SCUBA Local Universe Galaxy Survey - I. First measurements of the submillimetre luminosity and dust mass functions

Dwek E., Petre R., Szymkowiak A., Rice W.L. 1987 ApJ 320, L27
IRAS observations of supernova remnants - A comparison between their infrared and X-ray cooling rates

Efstathiou A., Rowan-Robinson M., 1995, MNRAS 273, 649
Dusty discs in active galactic nuclei

Fanti C., Pozzi F., Fanti R., Baum S.A., O'Dea C.P., Bremer M., Dallacasa D., Falcke H., de Graauw T., Marecki, A., Miley G., Rottgering H., Schilizzi R.T., Snellen I., Spencer R.E., Stanghellini C., 2000, A&A 358, 499
ISO observations of a sample of Compact Steep Spectrum and GHz Peaked Spectrum radio galaxies

Genzel R., Lutz D., Sturm E., Egami E., Kunze D., Moorwood A.F.M., Rigopoulou D., Spoon H.W.W., Sternberg A., Tacconi-Garman, L.E., Tacconi L., Thatte N., 1998, ApJ 498, 579
What powers ultraluminous IRAS galaxies?

Genzel R., Cesarsky C., 2000, Ann. Rev. A&A 38, 761
Extragalactic Results from the Infrared Space Observatory

Gehren T., Fried J., Wehinger P.A., Wyckoff S., 1984, ApJ 278, 11
Host galaxies of quasars and their association with galaxy clusters

Golombek D., Miley G.K., Neugebauer G., 1988, AJ 95, 26
IRAS observations of radio galaxies

Granato G.L., Danese L., 1994, MNRAS 268, 235
Thick Tori around Active Galactic Nuclei - a Comparison of Model Predictions with Observations of the Infrared Continuum and Silicate Features

Granato G.L., Danese L., Franceschini A., 1997, ApJ 486, 147
Thick Tori around Active Galactic Nuclei: The Case for Extended Tori and Consequences for Their X-Ray and Infrared Emission

Greenstein J.L, Matthews T.A., 1963, ApJ 68, 280
Redshift of the Radio Source 3C 48

Haas M., Chini R., Meisenheimer K., Stickel M., Lemke D., Klaas U., Kreysa E., 1998a, ApJ 503, L109
On the Far-Infrared Emission of Quasars

Haas M., Lemke D., Stickel M., Hippelein H., Kunkel M., Herbstmeier U., Mattila K., 1998b, A&A 338, L33
Cold dust in the Andromeda Galaxy mapped by ISO

Haas M., Chini R., Meisenheimer K., Stickel M., Lemke D., Klaas U., Kreysa E., Müller S.A.H., 1999, ESA-SP 427, 887
On the Far-Infrared Emission of Quasars

Haas M., Müller S.A.H., Chini R., Meisenheimer K., Klaas U., Lemke D., Kreysa E., Camenzind M., 2000, A&A 354, 453
Dust in PG quasars as seen by ISO

Haas M., Klaas U., Müller S.A.H., Chini R., Coulson I., 2001, A&A 367, L9
The PAH 7.7μm/850μm ratio as new diagnostics for high extinction in ULIRGs – increasing evidence for a hidden quasar in Arp220

Heckman T.M., Armus L., Miley G.K., 1987, AJ 93, 276
Evidence for large-scale winds from starburst galaxies. II - an optical investigation of powerful far-infrared galaxies

Heckman T.M., Chambers K.C., Postman M., 1992, ApJ 391, 39
The Infrared Properties of Quasars and Radio Galaxies: Testing the Unification Schemes

Heckman T.M., O'Dea Ch.P., Baum S.A., Laurikainen E., 1994, ApJ 428, 65
Obscuration, orientation, and the infrared properties of radio-loud active galaxies

Heckman T.M., Dahlem M., Eales S.A., Fabbiano G., Weaver K., 1996, ApJ 457, 616
ROSAT Observations of the X-Ray Nebula around ARP 220

Hes R., Barthel P.D., Hoekstra H., 1995, A&A 303, 8
The Far Infrared Properties of 3CR Quasars and Radio Galaxies

Hes R., Barthel P.D., Fosbury R.A.E., 1996, A&A 313, 423
Emission line imaging of 3CR quasars and radio galaxies

Hibbard J.E., Vacca W.D., Yun M.S., 2000, AJ 119, 1130
The Neutral Hydrogen Distribution in Merging Galaxies: Differences between Stellar and Gaseous Tidal Morphologies

Hildebrand R.H., 1983, QJRAS 24, 267
The Determination of Cloud Masses and Dust Characteristics from Submillimetre Thermal Emission

Hildebrand R.H., Whitcomb S.E., Winston R., Stiening R.F., Harper D.A., Moseley S.H., 1977, ApJ 216, 698
Submillimeter photometry of extragalactic objects

Hoekstra H., Barthel P.D., Hes R., 1997, A&A 319, 757
Beamed radio and far infrared emission in quasars and radio galaxies

Hooper E.J., Wilkes B.J., Mc Leod K.K., Elvis M.S., Impey C.D., Lonsdale C.J., Malkan M.A., McDowell J.C., 1999, ESA-SP 427, 893
The US Key Project on AGN spectral energy distributions

Hill G.J., Goodrich R.W., Depoy D.L., 1996, ApJ 462, 163
Observations of Paschen alpha in a Complete Sample of Radio Galaxies

Hughes D.H., Robson E.I., Dunlop J.S., Gear W.K., 1993, MNRAS 263, 607
Thermal dust emission from quasars – I. Submillimetre spectral indices of radio-quiet quasars

Hutchings J.B., Campbell B., Pritchet C., Crampton D., 1981, ApJ 247, 743
Optical morphology of 13 QSOs

Hutchings J.B., Campbell B., Crampton D., 1982a, ApJ 261, 23
Color imaging QSO-galaxy interactions

Hutchings J.B., Campbell B., Gower A.C., Crampton D., Morris S.C., 1982b, ApJ 262, 48
Further morphological studies of QSOs

Hutchings J.B., Campbell B., 1983, Nature 303, 584
Are QSOs activated by interactions between galaxies?

Hutchings J.B., McClure R.D., 1990, PASP 102, 48
High-resolution optical imaging of three QSOs

Hutchings J.B., Neff S.G., 1992, AJ 104, 1
Optical imaging of QSOs with 0.5 arcsec resolution

Impey C.D., Neugebauer G., 1988, AJ 95, 307
Energy distribution of Blazars

Iwasawa K., 1999, MNRAS 302, 96
An X-ray investigation of powerful far-infrared galaxies

Jackson N., Browne I.W.A., 1992, MNRAS 250, 422
Optical properties of quasars: – II. Emission-line geometry and radio properties

Kessler M.F., Steinz J.A., Anderegg M.E., Clavel J., Drechsel G., Estaria P., Faelker J., Riedinger J.R., Robson A., Taylor B.G., Ximenez de Ferran S., 1996, A&A 315, L27
The Infrared Space Observatory (ISO) Mission

Klaas U., Haas M., Heinrichsen I., Schulz B., 1997, A&A 325, L21
Infrared spectral energy distributions of the interacting galaxies ARP 244, NGC 6240, and ARP 220

Klaas U., Haas M., Müller S.A.H., Chini R., Schulz B., Coulson I., Hippelein H., Wilke K., Albrecht M., Lemke D., 2001, A&A submitted
Infrared to millimetre photometry of ultra-luminous IR galaxies: new evidence favouring a 3–stage dust model

Krolik J.H., Begelman M.C., 1988, ApJ 329, 702
Molecular tori in Seyfert galaxies - Feeding the monster and hiding it

Krügel E., Siebenmorgen R., 1994, A&A 288, 929
Dust in protostellar cores and stellar disks

Laor A. 1998, ApJ 505, L83
On Quasar Masses and Quasar Host Galaxies

Laing, R. A., Riley J. M., Longair M. S., 1983, MNRAS 204, 151
Bright radio sources at 178 MHz - Flux densities, optical identifications and the cosmological evolution of powerful radio galaxies

Léger A., Puget J.-L., 1989, Ann. Rev. A&A 27, 161
A new component of the interstellar matter: small grains and large aromatic molecules

Lemke D., Klaas U., Abolins J., Abraham P., Acosta-Pulido J., Bogun S., Castaneda H., Cornwall L., Drury L.; Gabriel C., Garzon, F., Gemuend H.-P., Groezinger U., Gruen E., Haas M., Hajduk C., Hall G., Heinrichsen I., Herbstmeier U., Hirth G., Joseph R., Kinkel U., Kirches S., Koempe C., Kraetschmer W., Kreysa E., Krueger, H., Kunkel

M., Laureijs R., Luetzow-Wentzky, P., Mattila K., Mueller T., Pacher T., Pelz, G., Popow E., Rasmussen I., Rodriguez Espinosa J., Richards P., Russell S., Schnopper H., Schubert J., Schulz B., Telesco C., Tilgner C., Tuffs R., Voelk H., Walker H., Wells M., Wolf J., 1996, A&A 315, L64
ISOPHOT – capabilities and perfomance

Lisenfeld U., Isaak K.G., Hills R., 2000, MNRAS 312, 433
Dust and gas in luminous infrared galaxies - results from SCUBA observations

Lutz D., Feuchtgruber H., Genzel R., Kunze D., Rigopoulou D., Spoon H.W.W., Wright C.M., Egami E., Katterloher R., Sturm E., Wieprecht E., Sternberg A., Moorwood A.F.M., de Graauw T., 1996, A&A 315, L64
SWS observations of the Galactic center.

Mathis J.S., Mezger P.G., Panagia N., 1983, A&A 128, 212
Interstellar radiation field and dust temperatures in the diffuse interstellar matter and in giant molecular clouds

Mattila K., Lemke D., Haikala L.K., Laureijs R.J., Leger A., Lehtinen K., Leinert Ch., Mezger P.G., 1996, A&A 315, L353
Spectrophotometry of UIR bands in the diffuse emission of the galactic disk

McCarthy P.J, van Breugel W., Spinrad H., Djorgovski S. 1987, ApJ 321, L29
A correlation between the radio and optical morphologies of distant 3CR radio galaxies

McLeod K.K, Rieke G.H. 1994a, ApJ 420, 58
Near-infrared imaging of low-redshift quasar host galaxies

McLeod K.K, Rieke G.H. 1994b, ApJ 431, 137
Near-infrared imaging of low-redshift quasar host galaxies. 2: High-luminosity quasars

Meisenheimer K., Haas M., Müller S.A.H., Chini R., Klaas U., Lemke D., 2001, A&A in press
Dust emission from 3C radio galaxies and quasars: New ISO observations favour the unified scheme

Nelson B., Cutri R.M., Kirkpatrick J.D., et al., 1998, BAAS 193, 8104
A New Population of IR-Selected AGN Uncovered By 2MASS

Netzer H. 1990, in *Active Galactic Nuclei* eds. Blandford R.D., Netzer H., Woltjer L., Springer–Verlag Lecture Notes, p. 135

Neugebauer G., Miley G.K., Soifer B.T., Clegg P.E., 1986, ApJ 308, 815
Quasars measured by the Infrared Astronomical Satellite

Orr M.J.L., Browne I.W.A., 1982, MNRAS 200, 1067
Relativistic beaming and quasar statistics

Parker B., 1990, Plenum Press
Colliding Galaxies – the universe in turmoil

Perley R.A., Dreher J.W., Cowan J.J., 1984, ApJ 285, L35
The jet and filaments in Cygnus A

Pier E.A., Krolik J.H., 1992, ApJ 401, 99
Infrared Spectra of Obscuring Dust Tori around Active Galactic Nuclei. I - Calculational method and basic trends

Pier E.A., Krolik J.H., 1993, ApJ 418, 673
Infrared Spectra of Obscuring Dust Tori around Active Galactic Nuclei. II. Comparison with Observations

Phinney E.S. 1989, in "Theory of Accretion Disks" eds. Meyer F., Duschl W., Frank J. et al. Kluwer Academic Publishers, p.457
Dusty disks and the infrared emission from AGN

Rigopoulou D., Lawrence A., Rowan-Robinson M., 1996, MNRAS 278, 1049
Multiwavelength energy distributions of ultraluminous IRAS galaxies - I. Submillimetre and X-ray observations

Rigopoulou D., Spoon H.W.W., Genzel R., Lutz D., Moorwood A.F.M., Tran Q.D., 1999, AJ 118, 2625
A Large Mid-Infrared Spectroscopic and Near-Infrared Imaging Survey of Ultraluminous Infrared Galaxies: Their Nature and Evolution

Risaliti G, Gilli R., Maiolino R., Salvati M., 2000, A&A 357, 13
The hard X-ray emission of luminous infrared galaxies

Robson I., 1996, Wiley Praxis Publishing
Active Galactic Nuclei

Rowan-Robinson M., 1995, MNRAS 272, 737
A new model for the infrared emission of quasars

Rowan-Robinson M., 2000, MNRAS 316, 885
Hyperluminous infrared galaxies

Sakamoto K., Scoville N.Z., Yun M.S., Crosas M., Genzel R., Tacconi L.J., 1999, ApJ 514, 68
Counterrotating Nuclear Disks in ARP 220

Sanders D.B., Soifer B.T., Elias J.H., Madore B.F., Matthews K., Neugebauer G., Scoville N.Z., 1988a, ApJ 325, 74
Ultraluminous infrared galaxies and the origin of quasars

Sanders D.B., Soifer B.T., Elias J.H., Neugebauer G., Matthews K., 1988b, ApJ 328, L35
Warm ultraluminous galaxies in the IRAS survey - The transition from galaxy to quasar?

Sanders D.B., Phinney E.S., Neugebauer G., Soifer B.T., Matthews K., 1989, ApJ 347, 29
Continuum energy distribution of quasars: shapes and origins

Sanders D.B., Mirabel I.F., 1996, Ann. Rev. A&A 34, 749
Luminous Infrared Galaxies

Sanders D.B., 1999, Ap&SS 266, 331
The "Great Debate": The case for AGNs

Schmidt M., 1963, Nature 197, 1040
3C 273: A star-like object with large red-shift

Schmidt M., Green R.F., 1983, ApJ 269, 352
Quasar evolution derived from the Palomar bright quasar survey and other complete quasar surveys

Scoville N.Z., Yun M.S., Bryant P.M., 1997, ApJ 484, 702
Arcsecond Imaging of CO Emission in the Nucleus of ARP 220

Scoville N.Z., Evans A.S., Dinshaw N., Thompson R., Rieke M., Schneider G., Low F.J., Hines D., Stobie B., Becklin E., Epps H., 1998, ApJ 492, L107
NICMOS Imaging of the nuclei of Arp220

Singal A.K., 1993a, MNRAS 262, L27
Evidence against the unified scheme for powerful radio galaxies and quasars

Singal A.K., 1993b, MNRAS 263, 139
Cosmic evolution and luminosity dependence of the physical sizes of powerful radio galaxies and quasars

Singal A.K., 1996, MNRAS 278, 1069
Differential number counts of radio galaxies and quasars: evidence against the unified scheme

Smith C.H., Aitken D.K., Roche P.F., 1989, MNRAS 241, 425
The nature of the infrared luminous galaxies ARP 220 and NGC 6240

Smith H.E., Lonsdale C.J., Lonsdale C.J. Diamond P.J,, 1998, ApJ 493, L21
A starburst revealed – luminous radio supernovae in the nuclei of Arp 220

Soifer B.T., Neugebauer G., Matthews K., Becklin E.E., Ressler M., Werner M.W., Weinberger A.J., Egami E., 1999, ApJ 513, 207
High Spatial Resolution Imaging of ARP 220 from 3 to 25 Microns

Stockton, A., 1982, ApJ 257, 33
Compact companions to QSOs

Stockton, A., 1986, Ap&SS 118, 487
The environment of QSOs

Sturm E., Lutz D., Genzel R., Sternberg A., Egami E., Kunze D., Rigopoulou D., Bauer O.H., Feuchtgruber H., Moorwood A.F.M., de Graauw T., 1996, A&A 315, L133
ISO-SWS spectroscopy of ARP 220: a highly obscured starburst galaxy

Telesco C.M., Harper D.A., Loewenstein R.F., 1976, ApJ 203, L53
Far-infrared photometry of NGC 1068

Urry C.M., Padovani P., 1995, PASP 107, 803
Unified Schemes for Radio-Loud Active Galactic Nuclei

van Bemmel I.M., Barthel P., de Graauw Th., 2000, A&A 359, 523
ISOPHOT observations of 3CR quasars and radio galaxies

van Bemmel I.M., Bertholdi F., 2001, A&A 368, 414
Millimeter observations of radio-loud active galaxies

Véron-Cetty M.P., Véron P. 1998, ESO Scientific Report, (8th Edition), ESO, Garching
A Catalogue of Quasars and Active Nuclei

Wilkes B.J., Hooper E.J., Mc Leod K.K., Elvis M.S., Impey C.D., Lonsdale C.J., Malkan M.A., McDowell J.C., 1999, ESA-SP 427, 845
The far-infrared continuum of quasars

Wilkinson P.N., Akujor C.E., Cornwell T.J., Saikia D.J., 1991, MNRAS 248, 86
3C380 - A powerful radio source seen end-on?

Wills B.J., Wills D., Evans N.J., Natta A., Thompson, K.L., Breger M., Sitko M.L., 1992, ApJ 400, 96
Polarimetry and spectrophotometry of the QSO IRAS 13349+2438 and the unification of active galaxies

Wisotzki L., Christlieb N., Bade N., Beckmann V., Köhler T., Vanelle C., Reimers D., 2000, A&A 358, 77
The Hamburg/ESO survey for bright QSOs. III. A large flux-limited sample of QSOs

Acknowledgements

It is a pleasure for me to thank the many scientists, friends and colleagues who have contributed to inspiring discussions during the last few years. Special thanks go to

- Prof. Dietrich Lemke, who provided the framework for science at the ISOPHOT Data Centre and monitored the progress of the results with continued interest.

- Prof. Rolf Chini (Universität Bochum) and Prof. Klaus Meisenheimer, who allowed me to manage the *ISO Central European Quasar Programme* during the in-orbit phase, in order to optimize the observations, and to participate in creating and presenting the scientific output. Klaus Meisenheimer gave me an excellent introduction into the concept of unified schemes, and the interpretation of the ISO results profited from critical discussions with him. Rolf Chini provided the essential mm data for the quasars with IRAM. He also performed the mm observations for the ULIRGs with SEST, while I observed simultaneously at the JCMT. Also, while developing the new extinction diagnostics I learnt greatly from his expertise on dust models.

- PhD student Dipl. Phys. Sven Müller, who gave invaluable help in designing special new tools for the data reduction. He implemented the entire software and kindly prepared most of the graphic presentations of the results.

- Dr. Ulrich Klaas, who was really an *alter ego* in our daily discussions towards reaching a balanced view on numerous topics. The sub-mm and mm ISO-follow-up observations of the nearby ULIRGs are joint projects of ours.

- Prof. Hans Elsässer, who with Prof. Dietrich Lemke encouraged my comeback to astronomy, and Dr. Hans Hippelein, Prof. Christoph Leinert and Dr. Manfred Stickel, who have always found time to motivate me.

- Dr. Peter Ábrahám, Dr. Karsten Wilke, Dr. Philippe Héraudeau and Dr. Carlos del Burgo, who with Dr. Ulrich Klaas took over the validation of the final ISOPHOT calibration.

- Prof. Immo Appenzeller, who supervised my course of lectures on *Fern-Infrarot Astronomie* in his unique and efficient manner.

When I was a young boy, my mother recognised that the scientific milieu suited me best, and her love and spirit helped me to go this way. My father died too early to have a direct influence on my affinities, but in crucial situations, when I asked myself “what would he have done”, I felt his answer. And my wife Regina took great care to create a productive and harmonious lifestyle.